Winter 2010

Active Control of Shocks and Sonic Boom Ground Signal

Bedri Yagiz
Old Dominion University

ACTIVE CONTROL OF SHOCKS AND SONIC BOOM GROUND SIGNAL

by

BEDRI YAGIZ
B.Sc. June 2002, Istanbul Technical University, Turkey
M.S. June 2005, Istanbul Technical University, Turkey

A Dissertation Submitted to the Faculty of
Old Dominion University in Partial Fulfillment of the
Requirement for the Degree of

DOCTOR OF PHILOSOPHY

AEROSPACE ENGINEERING

OLD DOMINION UNIVERSITY
December 2010

Approved by:

Osama A. Kandil (Director)

Oktay Baysal (Member)

Duc T. Nguyen (Member)

Keejoo Lee (Member)

ABSTRACT

ACTIVE CONTROL OF SHOCKS AND SONIC BOOM GROUND SIGNAL

BEDRI YAGIZ
Old Dominion University, 2010
Director: Dr. Osama A. Kandil

The manipulation of a flow field to obtain a desired change is a much heightened subject. Active flow control has been the subject of the major research areas in fluid mechanics for the past two decades. It offers new solutions for mitigation of shock strength, sonic boom alleviation, drag minimization, reducing blade-vortex interaction noise in helicopters, stall control and the performance maximization of existing designs to meet the increasing requirements of the aircraft industries. Despite the wide variety of the potential applications of active flow control, the majority of studies have been performed at subsonic speeds. The active flow control cases were investigated in transonic speed in this study. Although the active flow control provides significant improvements, the sensibility of aerodynamic performance to design parameters makes it a nontrivial and expensive problem, so the designer has to optimize a number of different parameters. For the purpose of gaining understanding of the active flow control concepts, an automated optimization cycle process was generated. Also, the optimization cycle reduces cost and turnaround time. The mass flow coefficient, location, width and angle were chosen as design parameters to maximize the aerodynamic performance of an aircraft. As the main contribution of this study, a detailed parametric study and optimization process were presented. The second step is to appraise the practicability of weakening the shock wave and thereby reducing the wave drag in transonic flight regime using flow control devices such as two dimensional contour bump, individual jet actuator, and also the hybrid control which includes both control devices together, thereby gaining the desired improvements in aerodynamic performance of the air-vehicle. After this study, to improve the aerodynamic performance, the flow control and shape parameters are optimized separately, combined, and in a serial combination. The remarkable part of all these studies is both gradient and non-gradient optimization techniques were used to find the global optimum point. The second part of this study includes

investigation of the possibility of weakening the shock strength and the reduction of far field signature by using off- body energy addition. The main obstacle for flying supersonically over land is the detrimental effects of sonic boom on general public and structures. The shock waves generated from various parts of an aircraft flying at supersonic speed, coalesce to form a classic sonic boom acoustic signature, 'N' wave associated with the sonic boom on the ground. High pressure was imposed on certain parts of the computational domain to simulate the pulsed laser effects, and then the propagation and interaction of this pulsed shock with shock waves generated from the diamond shaped model were investigated. Optimization of the location and the power of the pulsed shock were achieved using the non-gradient optimization technique. The main contribution of this study is the optimization of the parameters of pulsed shock.

ACKNOWLEDGEMENTS

I would like to express my sincere gratitude and appreciation to my advisor Dr. Osama A. Kandil for his trust, encouragement and continuous support, during my research and course works. I am also thankful to the members of my dissertation committee, Dr. Oktay Baysal, Dr. Duc T. Nguyen and Dr. Keejoo Lee, for reviewing this manuscript.

I would like to thank my friends Dr. Kursat Kara, Dr. Mehti Koklu, Dr. Ilteris Koc, and Omer San for their friendship and support and for making my life easy here in Norfolk. I would like to thank all my professors from Istanbul Technical University for teaching and inspiring me with their knowledge and character.

Last but definitely not least, I want to convey my deepest thanks to my mother, Emine, my father Niyazi, my brother Serdar and Serkan, and my sister Kader. Finally, I want to thank the especially to my wife - Emine Tuba, and my children - Yusuf Fethi and Zeynep Nida - who have been patient and understanding while their husband and father was in his ivory tower.

TABLE OF CONTENTS

Page

LIST OF TABLES ix
LIST OF FIGURES xii

CHAPTERS

I INTRODUCTION 1
I.1 Flow Control of Shock and Boundary Layer 4
I.2 Motivation 5
I.3 Optimization 6
I.4 Outline of Present Research 8
I.5 Contribution of the Research 9
II MATHEMATICAL MODEL 10
II.1 Numerical model for flow analysis 10
II.1.1 Governing Equations 10
II.1.2 Time Advancement 13
II.1.3 Spatial Discretization 13
II.2 Initial and Boundary Conditions 14
II.2.1 Viscous Surface (Mass Transfer) 14
II.2.2 General Symmetry Plane 15
II.2.3 Extrapolation 16
II.2.4 Inflow/Outflow 16
II.2.5 Specified Pressure Ratio 17
II.3 Shock Boundary Layer Interaction 17
III COMPUTATIONAL TOOLS 20
III.1 Mesh Generation 20
III.2 Flow Solver 20
III.3 Optimization Codes 21
III.4 Computational Resources 22
IV OPTIMIZATION TECHNIQUES 23
IV.1 Gradient Based Optimization 23
IV.2 Non-Gradient Based Optimization 27
IV.2.1 Vibrational Genetic Algorithm 27
V ACTIVE CONTROL OF SHOCKS APPLICATIONS 30
V.1 Optimization of Active Flow Control of an Airfoil 30
V.1.1 Introduction 30
V.1.2 Optimization Methodologies 31
V.1.3 Grid Generation 31
V.1.4 Validation and Grid Sensitivity 31
V.1.5 Problem Parameterizations and Parametric Study 33
V.1.6 Optimization Results 38
V.1.7 Conclusion 49

V.2 Drag Reduction Optimization by Using Flow Control Techniques . . . 56
V.2.1 Introduction . . . 56
V.2.2 Optimization methodology . . . 58
V.2.3 Grid Generation . . . 59
V.2.4 Validation and Grid Sensitivity . . . 59
V.2.5 Bump-optimization study . . . 60
V.2.6 Discrete Suction-optimization study . . . 63
V.2.7 Hybrid-optimization study . . . 69
V.2.8 Conclusion . . . 72
V.3 Combined Optimization of Shape and Flow Control Parameters on an Airfoil at Transonic Speeds . . . 78
V.3.1 Introduction . . . 78
V.3.2 Numerical Model for Optimization Process . . . 79
V.3.3 Design parameters and objective function description . . . 79
V.3.4 Grid generation, validation, and sensitivity . . . 82
V.3.5 Optimization Results . . . 83
V.3.6 Conclusions . . . 94
VI CONTROL OF SONIC BOOM . . . 98
VI.1 Introduction . . . 98
VI.2 Motivation . . . 100
VI.3 Outline of Present Research . . . 101
VI.4 Problem Construction . . . 101
VI.5 Computational Modeling . . . 103
VI.5.1 Numerical model for flow analysis . . . 103
VI.5.2 Design parameters and objective function . . . 104
VI.5.3 Numerical model for optimization . . . 106
VI.6 Optimization Study . . . 109
VI.7 Far Field Result . . . 112
VI.8 Conclusions . . . 113
VII CONCLUSIONS AND RECOMMENDATIONS . . . 118
VII.1Conclusions . . . 118
VII.2Recommendations for Future Research . . . 121
Bibliography . . . 123

APPENDICES

A PSO of AFC on an Airfoil at Transonic Regime . . . 133
A.1 Introduction . . . 133
A.2 Optimization . . . 133
A.2.1 Particle Swarm Optimization . . . 133
A.3 Design Parameters and Objective Function . . . 136
A.4 Optimization Results . . . 137
A.5 Fixed location optimizations . . . 137
A.6 Variable location optimizations . . . 141
A.7 Comparative Evaluations . . . 144

A.8 Conclusions 147
B Time Advancement 149
C Spatial Discretization 151
C.1 Discretization of inviscid fluxes 151
C.2 Flux Difference Splitting 151
C.3 Discretization of Viscous Fluxes 153
D Thomas Code 155

VITA 158

LIST OF TABLES

		Page
1	Grid sensitivity for NACA64A010 aerofoil test cases	33
2	Initial and optimal values of angle optimization	42
3	Initial and optimal values for mass flow coefficient optimization	42
4	Initial and optimal values for mass flow coefficient optimization	42
5	Initial and optimal values for mass flow coefficient optimization	43
6	Vibrational genetic algorithm features	47
7	Single-jet with multi variable optimization	48
8	Multi variable optimization results	49
9	*Rae*5243 aerofoil lift and drag coefficient without and with suction	60
10	Initial and optimal parameters	63
11	Initial and optimal values	69
12	Initial and optimal values	76
13	The features of GA	79
14	Grid sensitivity for *NACA-64A010* aerofoil test cases	83
15	Optimization Steps	106

LIST OF FIGURES

		Page
1	Shock Boundary Layer Interaction	19
2	Illustration of active-violated constraints	25
3	Computational grid used in the 2D simulations	32
4	Comparison of pressure distributions for *NACA-64A010* aerofoil (a)without and (b)with suction	34
5	AFC actuator installed on the upper surface of the airfoil	34
6	Parameterizations of AFC actuator	35
7	Effect of actuator width with (a)suction and (b)blowing ($\beta = 45^0$, x_c=0.715c)	36
8	Pressure Distributions for five different width values with (a)suction (C_q=-0.02) and (b)blowing (C_q=0.01), ($\beta = 45^0$, x_c =0.715c)	37
9	Effect of C_q with (a)suction and (b)blowing (w_d=0.035 x/c, x_c=0.715c)	38
10	Pressure Distributions for various C_q values with (a)suction and (b)blowing ($\beta = 45^0$, w_d=0.035 x/c, x_c=0.715c)	39
11	Effect of location with (a)suction and (b)blowing ($\beta = 45^0$, w_d=0.035c)	40
12	Pressure distributions for various locations with (a)suction (C_q=-0.02) and (b)blowing (C_q=0.01), ($\beta = 45^0$, w_d=0.035c)	41
13	Effect of angle with (a)suction and (b)blowing (w_d=0.035 x/c. x_c=0.715c)	43
14	Pressure distributions for three different angles with (a)suction (C_q=-0.02), and (b)blowing (C_q=0.01), (w_d=0.035 x/c. x_c=0.715c)	44
15	History of β optimization for *Case* 1; Design Variable:β, Objective function:C_L/C_D, Constant variable:$C_q = C_{q0}$, $x_c = x_{c0}$, $w_d = w_{d0}$	45
16	History of C_q optimization for *Case* 2; Design Variable:C_q, Objective function:C_L/C_D, Constant variable:$\beta = \beta^*$, $x_c = x_{c0}$, $w_d = w_{d0}$	45
17	History of x_c optimization for *Case* 3; Design Variable:x_c, Objective function:C_L/C_D, Constant variable:$\beta = \beta^*$, $C_q = C_q^*$, $w_d = w_{d0}$	46
18	History of w_d optimization for *Case* 4; Design Variable:w_d, Objective function:C_L/C_D, Constant variable:$\beta = \beta^*$, $C_q = C_q^*$, $x_c = x_c^*$	46
19	Optimization history of single-jet control system by using (a)SQP and (b)GA algorithm	47
20	Mach Contours for no control case	52
21	Mach Contours for single-jet control case	53
22	Pressure distribution for single-jet control case; $C_q^{**} = -0.1374$, $\beta^{**} = 3^0$, $x_c^{**} = 0.584c$, $w_d^{**} = 0.0579c$	53
23	Mach Contours for double-jet control	54
24	Pressure distribution for double-jet control; $C_{q1}^{**} = -0.2007$, $\beta_1^{**} = 3^0$, $x_{c1}^{**} = 0.914c$, $w_{d1}^{**} = 0.043c$; $C_{q2}^{**} = -0.0519$, $\beta_2^{**} = 3^0$, $x_{c2}^{**} = 0.599c$, $w_{d2}^{**} = 0.0464c$	54
25	Mach Contours for triple-jet control	55

26 Pressure distribution for triple-jet control; $C_{q1}^{**} = -0.1084$, $\beta_1^{**} = 3^0$, $x_{c1}^{**} = 0.941c$, $w_{d1}^{**} = 0.043c$; $C_{q2}^{**} = -0.1084$, $\beta_2^{**} = 3^0$, $x_{c2}^{**} = 0.763c$, $w_{d2}^{**} = 0.032c$; $C_{q3}^{**} = -0.1084$, $\beta_3^{**} = 3^0$, $x_{c3}^{**} = 0.618c$, $w_{d3}^{**} = 0.035c$ . . 55
27 The automated optimization process 58
28 The computational grid used in 2D simulation 59
29 Cp distributions over *Rae*5243 airfoil (a) without control and (b)with FC 61
30 Bump Picture 62
31 Variation of (a)bump Design and (b)normalized C_L,C_D during the bump control optimization process 64
32 Bump Optimization Study Results (a)Comparison of airfoil shapes (b)Cp distributions (c)BL comparison 65
33 Mach Contours (a)baseline and (b)with bump 66
34 Actuator Parameters 67
35 The variation of (a)C_q and (b)normalized C_L,C_D values during the optimization process 68
36 Comparison of (a)Cp distributions and (b)normalized BL Thickness . 70
37 Mach Contours (a)without FC and (b)with FC 71
38 Variation of (a) Design Variables and (b)Normalized C_L,C_D during hybrid control optimization process 73
39 Comparison of (a) Airfoil (b) Cp distributions and (c)BL thickness . 74
40 Mach Contours (a)baseline and (b)with hybrid control 75
41 Optimization process 80
42 Active flow control parameters 81
43 Shape parameters 82
44 Computational grid used in simulations 83
45 The change of aerodynamic coefficients and performance during the generations 85
46 Velocity profiles inside the boundary layers 86
47 C_p distributions around *NACA-64A010* 86
48 Mach counters around *NACA-64A010* without AFC 87
49 Mach counters around *NACA-64A010* with AFC 87
50 The change of aerodynamic coefficients and performance during the generations 88
51 C_p distributions around *NACA-64A010* and optimized airfoil 89
52 Mach counters around optimized airfoil shape 90
53 The change of aerodynamic coefficients and performance during the generations 91
54 C_p distributions around *NACA-64A010* and optimized airfoil 92
55 Mach counters around optimized airfoil shape 93
56 The change of aerodynamic coefficients and performance during the generations 95
57 C_p distributions around *NACA-64A010* and optimized airfoil 96
58 Mach counters around optimized airfoil shape 96

59 The comparative results among the constructed optimization cases . . 97
60 The model of wave propagation 102
61 Problem definition based on oblique shocks 103
62 Design parameters 104
63 Initial design points determined by LHD 107
64 Optimization process points and the global optimum location for the optimization process (left), convergence history for the period (right) 109
65 Sample time frames for the pulse extension in supersonic flow area . . 110
66 A sample time frame for the multiple energy-addition based pulses in supersonic flow area 111
67 Maximum dP via time at far-field signature 113
68 Near and far field results at points (1) and (2) 114
69 Near and far field results at points (3) and (4) 115
70 Near and far field results at points (5) and (6) 116
71 The design parameters for active flow control 137
72 The change of aerodynamic coefficients during the generations 138
73 The change of aerodynamic performance in PSO and SQP 139
74 The change of aerodynamic coefficients during the generations 140
75 The change of aerodynamic performance in PSO and SQP 140
76 The change of aerodynamic coefficients during the generations 141
77 The change of aerodynamic performance in PSO and SQP 141
78 The change of aerodynamic coefficients and performance during the generations 142
79 The change of aerodynamic coefficients and performance during the generations 143
80 The change of aerodynamic coefficients and performance during the generations 144
81 The effect of location and the number of actuators on an aerodynamic performance 145
82 The effect of control on the pressure field and coefficient for the one-actuator case 146
83 The effect of location on pressure field and coefficient for the two-actuator case 146
84 The effect of location on pressure field and coefficient for the three-actuator case 147

CHAPTER I

INTRODUCTION

The manipulation of a flow field, in order to achieve a desired alteration is a heightened subject in the aerospace community. A considerable amount of research has been performed utilizing different flow control (FC) methods. FC is an attempt to alter the character and/or disposition of a flow field. To investigate the possibilities of FC has inspired and challenged engineers and the scientists for a long time. It has been more excitedly investigated by scientists than any other topic in fluid mechanics because of its potential advancements in improving the performance and maneuverability, increasing range and payload, providing affordability and environmental compliance of commercial and military aircraft.

A wide range of FC methods, ideas, and devices have been proposed and practiced in past decades. The FC methods are offering new solutions for lift enhancement, skin-friction and pressure drag reduction, shock strength and sonic boom mitigation, flow induced noise inhibition, heat transfer augmentation, mixing enhancement and stall control. To gain any of these useful end results, FC aims at delaying or progressing the transition from laminar to turbulent flow, at suppressing or intensifying turbulence levels, and at averting or aggravating the flow separation. These goals are not unavoidably mutually exclusive[1], a combination of them could be achieved. The achievement of one particular goal without adversely affecting another one is the quintessential challenge in selecting a FC device. For that reason, strong arrangements have to be made for the optimal benefits[2]. For instance, promoting the transition from laminar to turbulent boundary layer on a lifting surface, such as an aircraft wing, enhances the resistance to separation, and lift can be obtained at a higher angle of incidence. On the other hand, the skin friction drag and flow-induced noise for a turbulent boundary layer is higher than that for a laminar one. The laminar boundary layer can only struggle a small adverse pressure gradient; that's why it is more prone to separation which results lift reduction and form drag increment. The idealistic control method should be simple, inexpensive to establish as well as to operate. And, a particular control method should provide no existence of tradeoffs. A specific control method is preferred based on the kind of flow to achieve the performance maximization of existing designs to meet the enlarging requirements of the aircraft industries.

The modern use of FC originated with Prandtl's speech on "Uber Flussigkeit-bewegung bei sehr kleiner Reibung" (On fluid motion with very small friction) at Heidelberg Mathematicians Third International Congress. The theory of the boundary layer or the frictional layer, the idea of self similarity and separation control, was introduced for the first time in no more than 8 pages. Prandtl also demonstrated the mechanics of steady separation and depicted several experiments in which the boundary layer was controlled. In his research, Prandtl used mass removing to enhance the boundary layer's resistance to separation from the surface of the cylinder. He established the path for understanding the motion of real fluid; subsequently; the scientific FC method was born by this modest application. Thus, the selection of FC instruments is not any more a trial and error feat.

In the literature, a variety of impressive FC methods controlling or altering the behavior of fluid flow with the purpose of obtaining a desired goal were described and classified. The first typical approach for categorizing the FC methods depends on whether technique is employed at the wall or away from it in accomplishing the control. The methods applied at the wall influence the flow field by altering the surface parameters, such as wall roughness, curvature, rigid-wall motion, shape, temperature, stiffness, and porosity; by producing the viscosity and density gradients via a surface heating or cooling; by transferring mass or momentum through a wall with full of pores or slots by synthetic jet or plasma actuators; and by utilizing the different additives, such as micro bubbles, surfactant, polymers, droplets, dust or fibers. Also, several devices located away from the wall, such as large-eddy breakup devices, acoustic waves bombarding a shear layer from outside, and spectra, gust, and magneto- and electro-hydrodynamic body forces have the ability to modify a flow field to enhance efficiency and performance [3].

The second classification method of the FC technique proposed is based on whether or not additional energy is required and whether or not the control loop is involved. On the subject of energy expenditure, a control device can be active, requiring additional power, or passive, requiring no auxiliary energy. Altering the geometry of an aerodynamic shape to influence the pressure gradient in order to stabilize a laminar boundary layer[4] (Riley et al. 1988), installing fixed mechanical vortex generators to delay flow separation and aerodynamic stalling, and placing the longitudinal grooves or riblets on a surface to decease drag[5](Choi et al. 1993) are excellent examples of effective passive flow control (PFC) configurations. In recent

decades, there has been great importance placed on the application of active flow control (AFC) methods compared to conventional approaches. Although conventional methods deal with alteration of the mean flow, modern techniques attempt to manipulate the existing flow instabilities to obtain desired improvements in mean flow with a small amount of energy consumption[6]. AFC schemes can be broken into two categories as predetermined or interactive methods depending on existance of a control loop. A predetermined technique introduces the imposed steady or unsteady power without orienting attention to the particular state of the flow[7]. Therefore, the control loop in this method is open which simply means there is no demand for the sensor to send information forward; in other words, there is no direct feedback from the controlled condition. For example, when a predetermined method is used for a constant blowing actuator, it would operate continuously without regard to the flow condition structure. As practical examples for the predetermined technique, Smith and Glezer[8] (1997) utilized piezoelectric actuators to perform jet vectoring and Seifert and Pack[9] (1999) utilized oscillatory blowing to increase post-stall lift and to decrease form drag.

An interactive AFC system includes a controller (actuator) and a measurement element (sensor). A sensor is sending information to advise the controller that corrective action is required to obtain a desired improvement in the objective function. To state the matter differently, the energy input is continuously modified depending on the sensed information with consideration for the state of the flow field. The auxiliary energy used in an AFC method may be decided in advance (open-loop or feed-forward) or determined in real-time measurements of the flow (closed-loop or feedback control)[10]. In the open-loop (feed-forward) control system, the sensor is installed upstream of the actuator, and the resulting signal is used to adjust the controller. It is not a goal-seeking control system, so it does not consider whether or not the desired goal is fulfilled. Therefore, the measured and manipulated flow filed variable differs as flow passes over fixed sensors and actuators. Examples of open-loop control include a round jet under the time-periodic forcing to generate bifurcation or blooming[11] (Lee et al. 1985) and an electrolytic fluid under the hydrodynamic Lorenz forcing to restructure flow instabilities in vicinity the wall[12] (Nosenchuck et al. 1993). The effectiveness of an open-loop system is reduced when the flow field includes unstable coherent structures. And, if the controller works unnecessarily, this kind of control system could be detrimental. A closed-loop control system can be

more effective in modifying the flow field to achieve the desired effect. In this control scheme, the controlled flow field variable is measured by a sensor located downstream of the actuator, and the results are compared with the desired goal. By comparing the signals, the control system can be switched off when it is not required in order to save energy and to promote safety. Moin and Bewley[10] (1994) have categorized the closed-loop control into four schemes by examining their mathematical dependence on the governing equations of the flow phenomenon to be managed: adaptive control, physical model-based, dynamical systems-based, and optimal control.

The third category is to consider whether the FC scheme directly adjusts the global velocity profile or discerningly affects certain scales of motion. The shape of the instantaneous or mean velocity profile can be modified via surface motion, mass injection or removing the streamwise or spanwise pressure gradient or normal viscosity gradient generation by heating or cooling. Polymers, riblets, and LEBUs are utilized to change the small scales of motion rather than global velocity profile.[3]

I.1 FLOW CONTROL OF SHOCK AND BOUNDARY LAYER

The impetus to control the shock wave and boundary layer (BL) comes from performance and economical and environmental attentions. As mentioned in the previous chapter, FC approaches involve passive or active devices depending on whether or not energy is consumed in performing the control. A substantial amount of research has been carried out using passive methods of FC such as riblets, vortex generators, passive cavities etc., that modify a flow without auxiliary power. A substantial drag reduction has been achieved when a permeable surface covering a plenum chamber is located underneath the shock region for a freestream Mach number over an aerofoil of 0.81[13]. However, at off-design conditions, the viscous drag increment due to the rough permeable surface is more than the wave drag reduction obtained by PFC. PFC cannot be switched off when it is not required. AFC negates the disadvantages of PFC methods. Gad-el-Hak et al.[1, 2] and Bushnell and Hefner[14] provide an up-to-date overview of the subject of PFC.

Throughout the last decade, attention has been paid to the development of AFC methods in which external energy is introduced into the flow. Deforming surfaces, pulsed jets, active suctions, a synthetic jet actuator are some of the examples for AFC methods. Traditional AFC techniques are oriented toward direct interaction with, and change of, the mean flow about a body. Modern concepts of AFC are

associated with manipulation of existing flow instabilities to obtain gross alterations of mean flows with little spending of control energy[6].

AFC achieves an augmentation in lift and lift-to-drag ratio; thus, additional improvements in fuel consumption can be gained [15]. In the literature, there have been numerous studies about AFC offering the improvement for the performance of existing designs at subsonic speeds[16, 17]. Certain AFC actuators are effective at subsonic speeds because of the momentum and vorticity they produce, and the discussion of the application of AFC at transonic speeds frequently occurs in the literature. Arwarts et al.[18] designed a new concept to increase the efficiency of actuators to higher Mach numbers. Vadillo et al.[19] performed some cases in transonic flow past an airfoil using a synthetic jet. The small disturbance close to the shock wave can result in large changes in the aerodynamics of the airfoil at transonic and supersonic speeds[20]. An experimental study by Smith and Walker [21] has shown that application of strong suction in the strong adverse pressure gradient increases lift. Qin et al.[22] showed that lift could be increased by application of suction in the vicinity of the shock; however this is obtained with an increase in drag. Injection of momentum accelerates the inviscid outer flow over the airfoil ahead of the shock and induces weak compression waves that soften the adverse pressure gradient[23].

I.2 MOTIVATION

For aircraft flying at transonic speeds, shock waves develop over the lifting surface after the local pocket of supersonic flow. The formation of the shock wave will cause an additional drag that occurs in the transonic speed, which is called a wave drag. There are several ways of dealing with a wave drag such as active and passive control[24]. Examples of AFC techniques involve BL suction, tangentially blowing, and surface heating or cooling. Putting a porous surface with a cavity underneath the shock region is one PFC method. Although PFC enhances the aerodynamic performance at the design point, it could have harmful effects on off-design conditions. AFC can allow this disadvantage to be switched on in the flight envelope and to be switched off when not required. As well, hybrid control can be employed utilizing a combination of AFC and PFC.

Although the AFC provides such degrees of improvements, the sensibility of aerodynamic performance to design parameters makes it a nontrivial and expensive problem [25], so the designer has to optimize a number of different parameters. Therefore,

for the purpose of gaining understanding of the AFC concepts, an automated optimizing cycle process is needed. Also, the optimization cycle reduces cost and turnaround time. On the other hand, there have been only a few in depth investigations of optimization of the AFC methods. An optimally designed and actuated jet should lead to a jet that can be designed effectively at a lower cost with fewer power requirements as well as higher performance.

I.3 OPTIMIZATION

As a noun, the word optimization means "an act, process, or methodology of making something (as a design, system, or decision) as fully perfect, functional, or effective as possible" [26]. It is the procedure of maximizing or minimizing a desired cost function whilst satisfying the existing constraints. One of the most fundamental principles in our macrocosm is the hunting for an optimum state. There are numerous examples in nature where an optimal system status is sought. The atoms of metals and alloys take positions in order to minimize the energy of their electrons to form unit cells. These unit cells define the crystalline structure of materials. The perfect sphere, the geometric form of smallest surface area for a given volume, is a liquid droplet in zero gravity. Tall trees weigh many tons, and they form ribs near the base to strengthen them in bending. The honeycomb structure section is to be understood as one of the most compact packaging arrangements. The biological life leads to better adaptation of the species to their environment. Like nature, organizations and businesses have also struggled for excellence. The solutions to their problems have depended largely on judgments and experience. However, increased competition and consumer demands often require that the solutions be optimal and not just feasible [27]. In vehicles, weight minimization can affect fuel consumption, payloads, or performance. A small reduction in drag saves billions of dollars in annual fuel costs for land, air, and sea vehicles. Thus, many crucial decisions are made by choosing a quantitative measure of effectiveness and optimizing it.

Formally, the general multicriteria optimization problem can be defined as :

$$Minf(\mathbf{x})\mathbf{x} \epsilon R^n$$

Subject to:

$$g(\mathbf{x}) \leq 0,$$

$$h(\mathbf{x}) = 0,$$
$$\mathbf{x}_L \leq \mathbf{x} \leq \mathbf{x}_U \tag{1}$$

where $\mathbf{x} = (x_1, x_2, ..., x_n)^T$ is a column vector of n real-valued design variables. $\mathbf{f}$ is the objective function or cost function, $\mathbf{g}$ is inequality constraint, $\mathbf{h}$ is equality constraint, and $\mathbf{x}_U$ and $\mathbf{x}_L$ are upper and lower bounds of design variables. Briefly, this standard form includes three elements such as objective function, design variables, and constraints. Note that maximization of $\mathbf{f}$ is equivalent to the minimization of $-\mathbf{f}$. The goal of the optimization process is to obtain the proper design variable values which give the maximum or the minimum objective function value under defined constrained conditions.

Methods used for solving optimization problems may be classified as gradient-based or non-gradient based/derivative free. Gradient based algorithms search the design space and iteratively move from one design alternative to another improved alternative to find the next candidate solution in accordance with the derivative information. Common examples under this typology of solution methods are generalized reduced gradient (GRG) and sequential quadratic programming (SQP)[28]. SQP methods for constrained minimization were developed in the 1970s. The SQP method was first published by Pshenichny in 1970 in Russian and later in a book by Pshenichny and Danilin in 1978. This method has received a lot of attention in recent years owing to its superior rate of convergence [27]. GRG is one of a class of techniques called reduced-gradient or gradient projection methods which are based on extending methods for linear constraints to apply to nonlinear constraints. They adjust the variables so the active constraints continue to be satisfied as the procedure moves from one point to another. The ideas for these algorithms were devised by Wilde and Beightler using the name of constrained derivatives, with Wolfe using the name of the reduced-gradient method and extended by Abadie and Carpenter using the name generalized reduced gradient[29].

After the 1960s, side by side with the developments in gradient-based methods, there were also developments in non-gradient methods. The most popular ones are genetic algorithms (GA)[30], particle swarm optimization (PSO), simulated annealing (SA)[31], and ant colony optimization (ACO). Derivative free methods work through repeated function evaluations, decision of which solution candidate should be tested next, and the search for an optimum proceeds iteratively using heuristics methods. There are a lot of heuristic search methods in the literature.

Gradient based algorithms are proven to converge to the solution for a relatively shorter runtime. However, gradient-based optimization methods lack global searching features, and they tend to find the local optima in multimodal problems. This typology of solution methods are generally utilized because they can deal in large numbers of variables and constraints and also, they are rapid, rigorous and guarantee a locally optimum solution. Often heuristic algorithms may require numerous evaluations of cost functions when compared to gradient-based algorithms. They, however, provide attractive characteristics, such as incorporation of both global and local search, applicable for both continuous and discrete problems, efficient use of large numbers of parallel processors, no requirement for the continuity in response functions.

I.4 OUTLINE OF PRESENT RESEARCH

The primary goal of the first part of this study is to appraise the effectiveness of flow control techniques such as suction/blowing, local and global modification of airfoil geometry, and combination of them. The next goal is to develop a methodology to perform optimization. To obtain this objective, the following steps are taken :

- Investigate a detailed parametric study covering the large design space for the actuator.
- Couple Computational Fluid Dynamic (CFD) and optimization methodology to study single- and multi- variable design optimization.
- To improve the aerodynamic performance on airfoils in transonic conditions by using actuation in the form of steady suction/blowing on airfoils by utilizing a gradient based and a non-gradient based global algorithm optimization technique.
- To decrease the total drag in transonic conditions by using actuation in the form of steady suction/blowing, 2D local bump and a combination of these two methods (hybrid optimization) on the upper surface of airfoil.
- To improve the aerodynamic performance on an airfoil at transonic speed by optimizing the surface suction/blowing parameters and/or airfoil shape by utilizing the non-gradient based global algorithm and vibrational genetic algorithm enhanced with neural networks.

I.5 CONTRIBUTION OF THE RESEARCH

The contribution of this thesis is twofold. First, the understanding and modeling of the physical phenomena involved in a shock-wave/boundary-layer interaction under active and hybrid control conditions is presented. This action is based on execution of basic flow control parameter studies of aiming at a detail description of the interacting flow field and shock strength. Then, the benefits of AFC and PFC to improve the aerodynamic performance of an airfoil at a transonic speed are investigated. Subsequently, the interrelation among control aims is elaborated upon.

Second, the preceding study points the challenge to achieve the particular desired goal without violating another one. To obtain an ideal control method as effective as possible, an optimization approach has to be introduced into this problem. The gradient and non-gradient optimization techniques are used to search the global optimum point, and maybe this is the noteworthy part of this research. Equally important, an automated optimization cycle is produced to decrease computational time. In conclusion, the original goal and motivation behind the application of AFC and PFC on a transonic airfoil have been fully achieved with a little penalty. Based on this research, detailed and sufficient explanations are provided to aid in the preparation of a possible future study on AFC with optimization.

CHAPTER II

MATHEMATICAL MODEL

Theory and formulation of the present study are described in two sections. In the first part, the flow analysis formulations are given. In the second, brief theoretical information about the shock boundary layer interaction is presented.

II.1 NUMERICAL MODEL FOR FLOW ANALYSIS

An existing Navier-Stokes solver, CFL3D v6, for solving 2D/ 3D flows on a structured grids is used to perform the numerical simulations. The original version of CFL3D was developed in the early 1980s in the Computational Fluids Laboratory at NASA Langley Research Center. The general features of the code are described in Section 3, and governing equations and detailed formulations are given in the Appendices. Further information about the CFL3D code can also be found in Rumsey et al.[32]; Baysal et al.[33]; Bartels et al.[34]

II.1.1 Governing Equations

The governing equations, which are the thin layer approximations to the three-dimensional time dependent compressible Navier-Stokes equations, can be written in terms of generalized coordinates as:

$$\frac{\partial \hat{Q}}{\partial t} + \frac{\partial(\hat{F} - \hat{F}_v)}{\partial \xi} + \frac{\partial(\hat{G} - \hat{G}_v)}{\partial \eta} + \frac{\partial(\hat{H} - \hat{H}_v)}{\partial \zeta} = 0 \tag{2}$$

A general, three-dimensional transformation between the Cartesian variables (x, y, z) and the generalized coordinate (ξ, η, ζ) is implied. The variable J represents the Jacobian of the transformation:

$$J = \frac{\partial(\xi, \eta, \zeta, t)}{\partial(x, y, z, t)} \tag{3}$$

In equ.2, **Q** is the vector of conserved variables, density, momentum, and total energy per unit volume, such that

$$\hat{Q} = \frac{\mathbf{Q}}{\mathbf{J}} = \frac{\mathbf{1}}{\mathbf{J}} = \begin{vmatrix} \rho \\ \rho u \\ \rho v \\ \rho w \\ e \end{vmatrix} \tag{4}$$

The inviscid flux terms in 2 are

$$\hat{F} = \frac{\mathbf{F}}{\mathbf{J}} = \frac{\mathbf{1}}{\mathbf{J}} = \begin{vmatrix} \rho U \\ \rho U u + \xi_x p \\ \rho U v + \xi_y p \\ \rho U w + \xi_z p \\ (e+p)U - \xi_t p \end{vmatrix} \tag{5}$$

$$\hat{G} = \frac{\mathbf{G}}{\mathbf{J}} = \frac{\mathbf{1}}{\mathbf{J}} = \begin{vmatrix} \rho V \\ \rho V u + \eta_x p \\ \rho V v + \eta_y p \\ \rho V w + \eta_z p \\ (e+p)V - \eta_t p \end{vmatrix}$$

$$\hat{H} = \frac{\mathbf{H}}{\mathbf{J}} = \frac{\mathbf{1}}{\mathbf{J}} = \begin{vmatrix} \rho W \\ \rho W u + \zeta_x p \\ \rho W v + \zeta_y p \\ \rho W w + \zeta_z p \\ (e+p)W - \zeta_t p \end{vmatrix}$$

where the contravariant velocities are given as:

$$\begin{aligned} U &= \xi_x u + \xi_y v + \xi_z w + \xi_t \\ V &= \eta_x u + \eta_y v + \eta_z w + \eta_t \\ W &= \zeta_x u + \zeta_y v + \zeta_z w + \zeta_t \end{aligned} \tag{6}$$

Again in equation 2, the viscous flux terms are given as follows:

$$\hat{F}_v = \frac{\mathbf{F}_v}{\mathbf{J}} = \frac{\mathbf{1}}{\mathbf{J}} = \begin{vmatrix} 0 \\ \xi_x\tau_{xx} + \xi_y\tau_{xy} + \xi_z\tau_{xz} \\ \xi_x\tau_{xy} + \xi_y\tau_{yy} + \xi_z\tau_{yz} \\ \xi_x\tau_{xz} + \xi_y\tau_{zy} + \xi_z\tau_{zz} \\ \xi_x b_x + \xi_y b_y + \xi_z b_z \end{vmatrix} \tag{7}$$

$$\hat{G}_v = \frac{\mathbf{G}_v}{\mathbf{J}} = \frac{\mathbf{1}}{\mathbf{J}} = \begin{vmatrix} 0 \\ \eta_x\tau_{xx} + \eta_y\tau_{xy} + \eta_z\tau_{xz} \\ \eta_x\tau_{xy} + \eta_y\tau_{yy} + \eta_z\tau_{yz} \\ \eta_x\tau_{xz} + \eta_y\tau_{zy} + \eta_z\tau_{zz} \\ \eta_x b_x + \eta_y b_y + \eta_z b_z \end{vmatrix}$$

$$\hat{H}_v = \frac{\mathbf{H}_v}{\mathbf{J}} = \frac{\mathbf{1}}{\mathbf{J}} = \begin{vmatrix} 0 \\ \zeta_x\tau_{xx} + \zeta_y\tau_{xy} + \zeta_z\tau_{xz} \\ \zeta_x\tau_{xy} + \zeta_y\tau_{yy} + \zeta_z\tau_{yz} \\ \zeta_x\tau_{xz} + \zeta_y\tau_{zy} + \zeta_z\tau_{zz} \\ \zeta_x b_x + \zeta_y b_y + \zeta_z b_z \end{vmatrix}$$

The shear stress and hear flux terms are defined in tensor notations (summation convention implied) as

$$\tau_{x_i x_j} = \frac{M_\infty}{Re_{L_R}} \left[\mu \left(\frac{\partial u_i}{\partial x_j} + \frac{\partial u_j}{\partial x_i} \right) + \lambda \frac{\partial u_k}{\partial x_k} \delta_{ij} \right]$$

$$b_{x_i} = u_j \tau_{x_i x_j} - \dot{q}_{x_l} \tag{8}$$

$$\dot{q}_{x_l} = -\left[\frac{M_\infty \mu}{Re_{L_R} Pr(\gamma - 1)} \right] \frac{\partial a^2}{\partial x_i}$$

The pressure is obtained by the equation of state for a perfect gas

$$p = (\gamma - 1)\left(e - \frac{\rho}{2}(u^2 + v^2 + w^2)\right) \tag{9}$$

The variables in the above equations have been non-dimensionalized with respect to the free-stream density, $\tilde{\rho}_\infty$, the free-stream speed of sound, $\tilde{a}_\infty$, and the free-stream molecular viscosity, $\tilde{\mu}_\infty$. The chain rule is used to evaluate derivatives with

respect to (x, y, z) in terms of (ξ, η, ζ). Consistent with the thin-layer assumption, only those derivatives in the direction normal to the wall (ζ) are retained in the shear stress and heat flux terms. Equation 2 is closed by the Stokes hypothesis for bulk viscosity ($\lambda + \frac{2\mu}{3} = 0$) and Sutherland's law for molecular viscosity:

$$\mu = T^{3/2}\left(\frac{1+c}{T+c}\right) \tag{10}$$

where T is the non-dimensional temperature and c is the Sutherland's constant given by $c \approx 110.4/T_\infty$.

The details of the code can be found in the reference by Rumsey et al.[35]

II.1.2 Time Advancement

The CFL3D code is advanced in time with an implicit approximate-factorization method. The implicit derivatives are written as spatially first-order accurate, which results in block-tridiagonal inversions for each sweep. However, for the solutions that employ FDS the block-tridiagonal inversions are additionally simplified with a diagonal algorithm (with a spectral radius scaling of the viscous terms). Since the method in which the left-hand side of equation is treated for computational efficiency in steady-state simulations (approximate factorization, first-order accuracy), the second-order temporal accuracy is given up for unsteady computations. One method for recovering the desired accuracy is to use sub-iterations. Two different sub-iteration strategies have been implemented in CFL3D: the "pseudo time sub-iteration $(\tau - TS)$" method and the other method, termed "physical time sub-iteration $(t - TS)$". The details of these strategies are explained in Appendix A.

II.1.3 Spatial Discretization

The spatial derivatives of the convective and pressure terms are written conservatively as a flux balance across a cell for the discretization of inviscid fluxes. A state-variable interpolation and a locally one-dimensional flux model is utilized to determine the interface flux. To split these inviscid fluxes, CFL3D offers three different methods such as Flux Limiting, Flux Vector Splitting, and Flux Difference Splitting. Nonetheless, just the Flux Difference Splitting method is used in this research. The viscous terms that represent shear stress and heat transfer effects are discretized with second-order

central differences. The second derivatives are treated as differences across cell interfaces of the first-derivative terms. Appendix B includes the detail of the spatial discretization.

II.2 INITIAL AND BOUNDARY CONDITIONS

A set of initial conditions are needed to initiate the time integration process. In all cases, free stream environments are used to set the initial conditions.

The boundary conditions must be imposed explicitly at every time step in the iteration process on all sides of the domain and the physical surfaces of any objects presenting in the computational domain. This means that boundary conditions have to be enforced at each face of each computational block. CFL3D contains two types of boundary condition representations, namely cell-center and cell-face. The boundary conditions used in this study are viscous wall, inflow/outflow, general symmetry plane, extrapolation, specified pressure ratio.

II.2.1 Viscous Surface (Mass Transfer)

The viscous surfaces are implemented on the walls of the domains to impose the no-slip condition. With this boundary condition every no-slip wall segment can be set with different wall temperature conditions along with its additional data field ($\tilde{T}_w/\tilde{T}_\infty$). It also allows for mass flow through the wall (suction or blowing) through the second additional data field (C_q) where $C_q = (\rho u_{normal})/(\rho u)_\infty$. ($C_q$ is zero if there is no flow through the wall). Besides, $sjetx$,$sjety$ and $sjetz$ are the direction numbers of the blowing/suction in the x, y, and z directions, respectively. For example, if $sjetx = 1$ and $sjety = sjetz = 0$, then the blowing/suction will act in the x-direction. If $sjetx = 0.5$, $sjety = 0$, and $sjetz = 0.5$, then the blowing/suction will act at a 45^0 angle in the x-z plane. If all three direction numbers are zero, then the mass flow will default to be normal to the surface.

To obtain the smooth initiation inside the flow field, a constant rate of change in mass flow, C_{qu} from zero to a constant value within a defined time, T, is established and then C_q described in Eq. 11 will remain fixed.

$$C_q = \int_0^T C_{qu} dt \tag{11}$$

The pressure on the body, p_b, is calculated through the linear extrapolation :

$$p_b = p_1 - (p_2 - p_1)/2$$

The non-dimensional square of the speed of sound, c_2, at the wall is defined as:

$$c2 = (\frac{\tilde{a}_w}{\tilde{a}_\infty})^2 = \frac{\tilde{T}_w}{\tilde{T}_\infty}$$

$$c2 = (\frac{a_1}{a_\infty})^2[1 + \frac{\gamma - 1}{2}(M_1)^2] \tag{12}$$

The surface velocities are then given as:

$$\begin{aligned} u_w &= M_\infty C_q \frac{\xi_x}{\nabla\xi} \frac{(c2)}{\gamma p_b} \\ v_w &= M_\infty C_q \frac{\xi_y}{\nabla\xi} \frac{(c2)}{\gamma p_b} \\ w_w &= M_\infty C_q \frac{\xi_z}{\nabla\xi} \frac{(c2)}{\gamma p_b} \end{aligned} \tag{13}$$

II.2.2 General Symmetry Plane

The symmetry is supposed across an axis. The ghost point density values are determined equal to their "mirror image" counterparts.

$$\rho_{-1} = \rho_1$$

$$\rho_{-2} = \rho_2$$

The pressure values are assigned in the same way. The velocity components at the ghost cells are obtained as follows. Consider ghost cells at $i = 1$ face. Note that the normalized contra-variant velocity $\bar{U}$ is normal to $i = 1$ constant face. Let $\bar{U}_1$ be the normalized contra-variant velocity at cell center. For symmetry plane, $\bar{U}$ must have opposite signs on each side of the plane. Thus,

$$u_{-1} = u_1 - 2\hat{\xi}_x \bar{U}_1$$

$$\nu_{-1} = \nu_1 - 2\hat{\xi}_y \bar{U}_1$$

$$w_{-1} = w_1 - 2\hat{\xi}_z \bar{U}_1$$

where $\hat{\xi}_x, \hat{\xi}_y$ and $\hat{\xi}_z$ are the unit normals at $i = 1$ face.

II.2.3 Extrapolation

The flow field variables at ghost points are calculated based on zeroth-order extrapolation from the computational domain. The extrapolated values would be:

$$\rho_{-1} = \rho_1$$

$$\rho_{-2} = \rho_2$$

The rest of the flow field variables are evaluated based on the same zeroth-order extrapolation.

II.2.4 Inflow/Outflow

One-dimensional characteristic boundary conditions are locally used to incorporate the far field boundary conditions. The velocity normal to the far boundary and the speed of sound are calculated from two locally 1-d Riemann invariants, that is

$$R^{\pm} = \bar{u} \pm \frac{2a}{\gamma - 1}$$

where

$$\bar{u} = \bar{U} - \frac{\xi_t}{\nabla \xi}$$

$$\bar{U} = \frac{\xi_x}{\nabla \xi} u + \frac{\xi_y}{\nabla \xi} v + \frac{\xi_z}{\nabla \xi} w + \frac{\xi_t}{\nabla \xi}$$

R^- can be evaluated locally from conditions outside the computational domain and R^+ can be determined locally from inside the domain. The normal velocity and speed of sound are determined from

$$\begin{aligned} \bar{u}_{face} &= \frac{1}{2}(R^+ + R^-) \\ a_{face} &= \frac{\gamma - 1}{4}(R^+ - R^-) \end{aligned}$$

The Cartesian velocities are determined by decomposing the normal and tangential velocity vectors:

$$u_{face} = u_{ref} + \frac{\xi_x}{|\nabla\xi|}(\bar{u}_{face} - \bar{u}_{ref})$$
$$v_{face} = v_{ref} + \frac{\xi_y}{|\nabla\xi|}(\bar{u}_{face} - \bar{u}_{ref})$$
$$w_{face} = w_{ref} + \frac{\xi_z}{|\nabla\xi|}(\bar{u}_{face} - \bar{u}_{ref})$$

For inflow $ref \Longrightarrow \infty$, for outflow ref represents the values from the cell inside the domain adjacent to the boundary. The sign of the normal velocity $\bar{U}_{face} = \bar{u}_{face} + \frac{\xi_t}{|\nabla\xi|}$ determines whether the condition is at inflow ($\bar{u}_{face} < 0$) or outflow ($\bar{u}_{face} > 0$). The entropy is $\frac{p}{\rho_\gamma}$ determined using the value from outside the domain for inflow and from inside the domain for outflow. The entropy and speed of sound are used to determine the density and pressure on the boundary :

$$\rho_{face} = \left[\frac{(a_{face})^2}{\gamma S_{face}}\right]^{\frac{1}{\gamma-1}}$$
$$p_{face} = \frac{\rho_{face}(a^2_{face})}{\gamma}$$

II.2.5 Specified Pressure Ratio

The specified pressure ratio boundary condition is utilized to impose the pulse shock to computational domain. It is usually used as the outflow boundary condition for internal flows. A single pressure ratio, $\frac{\tilde{p}}{\tilde{p}_\infty}$, is defined on input. This pressure ratio is used to determine both two ghost point pressure boundary values. To set the boundary values for ρ, u, v, and w, extrapolation from inside the computational domain is used.

II.3 SHOCK BOUNDARY LAYER INTERACTION

The interaction of shock wave with a boundary layer is a classic viscous/inviscid interaction problem that plays a great role in determining the performance of transonic transport aircraft[36]. These phenomena are met in many fields of practical interests such as on transonic wings, turbomachines, helicopter blades, in supersonic air intakes, in propelling nozzles at off-design conditions and on deflected controls at supersonic/transonic speeds, to name a few. The SBLI is particularly important

in supercritical flows where the strong viscous interaction happening near the shock root causes a rapid thickening of the boundary layer and induces a mild increase in section drag to flow separation and buffeting if the shock is strong enough[37]. In the lack of separation the drag increment is generally due to wave drag, caused by an increase in the flow entropy through the interaction. SBLI occurs on transonic aerofoils at local mach numbers, between 1.1 and 1.5.

The inner part of the BL is completely subsonic. The neighboring subsonic and supersonic regions make the structure of the interaction very complicated. The pressure disturbances in the viscous boundary are allowed to be transmitted in both upstream and downstream directions. The interaction produces large shear gradients normal to the wall and the same time the low energy air is dragged downstream [13]. Although the effect of viscosity is relatively small in the outer part of BL, the inner part's viscous effects would cause the shock foot to smear due to the pressure rise across the freestream shock. The displacement and momentum thickness grow throughout the interaction.

As the sock becomes stronger, the pressure rise exerted on the flow field results in a larger compression wave and greater smearing of the shock foot. For a greater pressure rise, shear stress on the wall will locally be negative, which can produce separation and reattachment. The succeeding BL is inadequate in conquer the pressure increase enforced by the interaction and hereafter it separates to generate a free shear layer that,following attaches further at of the rear shock. The beginning of separation can have a terrible result on a transonic airfoil such as rise in drag, loss in a lift, various section moments and the start of buffet.

The thickening of the boundary layer in the shock foot region and the related wave pattern constructing by compression waves originating from the interaction upstream part can be seen in. Fig.1. After this interaction, there is still a small triangular region of supersonic flow(1) terminated by a nearly normal shock called the trailing shock. The normal trailing leg and the oblique leading leg meet the main shock at the triple point, also known as the bifurcation point. The increment in entropy is always greater through a single shock than the increment through successive shocks for the same final static pressure. Because of this, the Mach number downstream of the leading and trailing leg of the lambda structure(2) is greater than the Mach number downstream of the main shock(3). This discontinuity generates a slip line or vortex sheet.

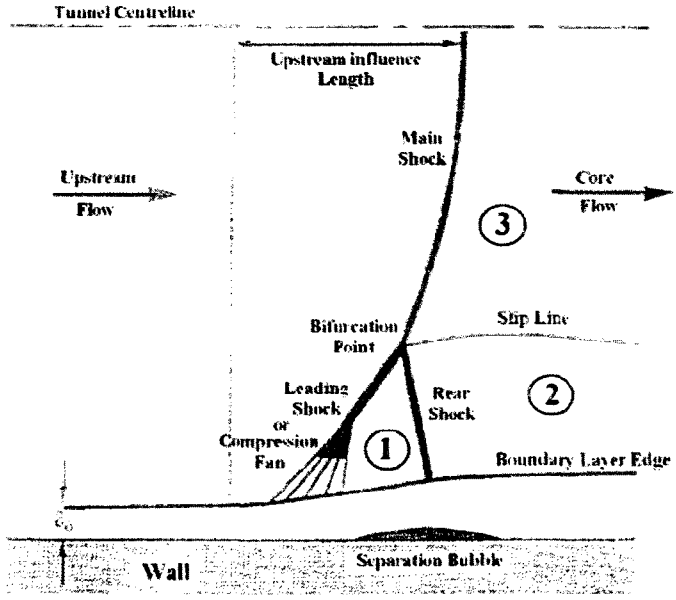

FIG. 1: Shock Boundary Layer Interaction

CHAPTER III

COMPUTATIONAL TOOLS

III.1 MESH GENERATION

The grid required by the analysis code is generated by powerful commercial grid generation software, Gridgen v15.05. These grids are structured 2-D grids that are clustered near the wall to ensure that the near wall $y+$ values of the airfoil blocks are kept in the appropriate range. The computational grid is clustered in the normal direction and in the vicinity of jets to resolve the details of the flow in AFC cases. For the local and global optimization process to generate the new grids an automated grid generation technique is developed in order to perform the optimization efficiently. Optimization code provides the new points of the airfoil, then the script produces the new grid.

III.2 FLOW SOLVER

CFL3D is a long-standing Navier-Stokes CFD code developed at NASA Langley Research Center for solving 2-D or 3-D flows on structured grids. The code is very reliable and stable and has many capabilities and options[38]. CFL3D solves the time-dependent conservation law form of the Reynolds-averaged Navier-Stokes equations. The spatial discretization involves a semi-discrete finite-volume approach. The spatial discretization of the inviscid and viscous fluxes are described in Appendix B. Upwind-biasing is used for the convective and pressure terms, while central differencing is used for the shear stress and heat transfer terms. Time advancement is implicit with dual time stepping and sub-iterations and the ability to solve steady or unsteady flows.

Multigrid and mesh sequencing are available for convergence acceleration. The full-approximation storage (FAS) multigrid algorithm is utilized to accelerate convergence to steady state (or to accelerate convergence of sub-iterations during a time-accurate computation). A sequence of grids is defined that denotes the finest grid, and coarser grids are formed by successively deleting every other grid line in all three coordinate directions. The fine grid serves to damp the high-frequency errors; the coarser grids damp the low-frequency errors.

Numerous turbulence models are provided such as 0-equation models: Baldwin-Lomax, Baldwin-Lomax with Degani-Schiff modification, 1-equation models: Baldwin-Barth, Spalart-Almaras[39], including Detached Eddy Simulation (DES), and also 2-equation models: Wilcox $k-\omega$ model, Menter's $k-\omega$ Shear Stress Transport (SST) model, Abid $k-\omega$ model, $k-\omega$ and $k-\varepsilon$ Explicit Algebraic Stress Models (EASM), k-entropy model.

CFL3D can perform computation on 1-1 blocking, patching, grid overlapping, and grid embedding. When two blocks share a face or a portion of a face and the grid points correspond with a point to point, the boundary condition communication set up between the two blocks is called 1-1 blocking. Grid patching, on the other hand, refers to the boundary condition interpolations set up between blocks that share a common face or portion of a face, but which do not match point to point. Grid overlapping has neither the restriction of point to point connectivity nor a common face between blocks. CFL3D does not contain any grid generation software. Grids must be supplied externally [35].

III.3 OPTIMIZATION CODES

VisualDOC is utilized in this study for gradient based optimization cases. It is a general-purpose optimization tool that allows the user to quickly add design optimization capabilities to almost any analysis program. It uses a powerful, intuitive graphical user interface along with state-of-the-art optimization algorithms to setup, solve, and post-process the design. It can be used for any design problem since it can be directed by defining which parameters may change (design variables) and measures the design quality (responses). It solves the design problem by calling the optimizer to modify the design variables and then calling the program that calculates the responses. It is also possible to pre/post process the design optimization data. It allows the user to use the optimization in parallel/distributed computing. For the gradient-based optimization, the user can provide gradients to program, or it will calculate the gradients using finite difference methods. Capabilities and options of the VisualDOC can be found in its manual[40].

For non-gradient optimization cases, the codes are written by Dr. Y. Pehlivanoglu using Matlab. The detail of the algorithms are written in his dissertation[41]. The communication between non-gradient optimization codes and solvers is established by Unix shell scripts. To decrease the computation time, in the computational phase

two-level parallelization is implemented. The first parallelization is applied in the swarm computed on different processors in a parallel way and the second is applied in flow solver by using multi-blocks.

III.4 COMPUTATIONAL RESOURCES

The flow domains analyzed in this dissertation were decomposed into blocks to obtain the solution in a reasonable time. Most of the computations were carried out using the hardware resources of Old Dominion University's first teraflop computer cluster, which has been given the name Zorka. A teraflop equals 1,000 gigaflops, and this is a measure of performance that Zorka can obtain when running even at partial capacity. (An average desktop system peaks near 5 gigaflops.) The new Dell high-performance cluster can handle the data crunching required for complex studies and simulations in fields such as aerospace engineering, mathematics, oceanography and bioelectric engineering. [42]. Zorka cluster is rated at 1.5 teraflops and has:

- Forty compute nodes, each with two 3-gigahertz dual-core Intel processors and 8 gigabytes of memory, providing 160 processor cores for parallel or serial applications;
- Four symmetric multiprocessor (SMP) nodes, each with four 2.4-gigahertz quad-core processors and 32 gigabytes of memory, providing 64 additional processor cores for large, shared memory applications;
- Four input/output (I/O) nodes supplying disk space to research applications: 9 terabytes of parallel file system disk and 3 terabytes of network file system (NFS) disk;
- A 20 gigabit-per-second Infiniband fabric connecting the compute nodes and I/O nodes;
- Fast disk space within the cluster to allow applications to run at very high speed and with low latency.

CHAPTER IV

OPTIMIZATION TECHNIQUES

IV.1 GRADIENT BASED OPTIMIZATION

The gradient-based optimization algorithm has been selected because it is reasonably robust and allows flexibility in formulating the design problem [40]. At first, optimization was applied using a black-box approach by employing finite differences to obtain gradient information. This means that getting gradients involved in calculating the flow solutions for the several perturbations of the design variables [43]. The major factor in determining the feasibility of optimization methods is the cost of obtaining these solutions. The gradient-based methods have a major distinguishing disadvantage convergence toward local optimum point. Non-gradient based methods such as simulated annealing, genetic algorithms have the ability to escape from the local minimums. Nonetheless, these methods require calculation of a large number of flow solutions. To escape from the local minimum/maximum, many initial points for all cases are used in this study.

A nonlinear-constrained optimization problem can be expressed as follows:

$$\begin{aligned} & Minf(X) \\ & \text{Subject to:} \\ & g_j(X) \leq 0, \quad j = 1, M \\ & h_k(X) = 0, \quad k = 1, L \\ & X_i^L \leq X_i \leq X_i^U, \quad i = 1, N \end{aligned} \tag{14}$$

Here, X is a column vector of n real valued design variables. $f(X)$ is the objective function, g_j's are inequality constraints, h_k's are equality constraints and X^L, and X^U, are the side constraints for the design variables.

There are numerous gradient and non-gradient optimization routines in the literature. However, in the present study, sequential quadratic programming (SQP) is used to solve the optimization problems. SQP is one of the most powerful methods among the mathematical nonlinear programming techniques[40]. The SQP method has several attractions such as the starting point can be infeasible and the gradients of only active constraints are needed. First of all, a quadratic approximation to the

objective function using the Taylor series expansion of the objective function is generated in this method. The result of the quadratic problem is used to decide the search direction at a given point. The quadratic problem is expressed as follows:

$$\begin{aligned} &Minimize \quad \nabla f(\mathbf{X^i})^\mathbf{T}\mathbf{S} + \frac{1}{2}\mathbf{S}^T\bar{\mathbf{H}}^\mathbf{i}\mathbf{S} \\ &Subjectto \quad \nabla g_j(\mathbf{X^i})^\mathbf{T}\mathbf{S} + g_j(\mathbf{X^i}) \leq 0 \end{aligned} \tag{15}$$

The search direction vector is the design variable for this quadratic problem. The matrix $\bar{\mathbf{H}}$ is initially the identity matrix, which is a positive definite matrix. To approach the Hessian of the objective function, $\bar{\mathbf{H}}$ is updated on the subsequent iterations. One design iteration of the gradient based optimization process is summarized as follows:

1. $i = 0$, $x = x^o$ (initial point);
2. $i = i + 1$'
3. Calculate $f(x^{i-1}), g_j(x^{i-1}), j = 1, n$;
4. Identify the set of critical constraints, J;
5. Evaluate $\nabla f(x^{i-1}), \nabla g_j(x^{i-1}), j \epsilon J$;
6. Determine a search direction, $\mathbf{S^i}$;
7. Investigate a one dimensional search to find, α^* (Sub iterations are done here);
8. Set $\mathbf{x^i} = \mathbf{x^{i-1}} + \alpha^*\mathbf{S^i}$;
9. Check for convergence to the optimum. An important part of the overall optimization process is deciding when to stop. Optimizer uses several criteria such as a maximum number of iterations, reasonable satisfaction of the Kuhn-Tucker conditions and diminishing returns where the optimum is approached asymptotically to make this decision[40].If converged, exit. If not go to step 2.

Finding a usable-feasible search direction ($\mathbf{S}^i$), finding the step size (α^i), and checking convergence are the three crucial parts of the optimization technique. The initial point in finding the usable-feasible search directions is to identify all constraints which are active or violated. Fig. 2 illustrates the definition of active and violated constraints. There are three possibilities :

1. There are no active or violated constraints;
2. There are active constraints but no violated constraints;
3. There are one or more violated Constraints;

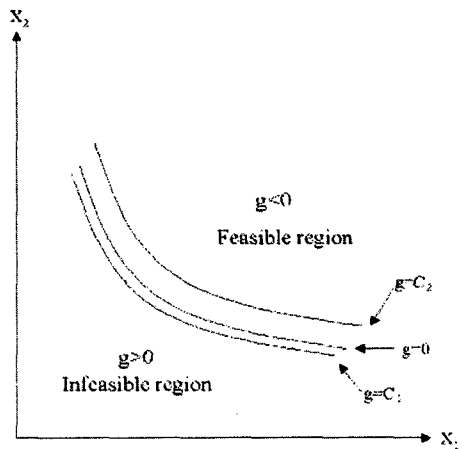

FIG. 2: Illustration of active-violated constraints

$$\begin{aligned} g_j(\mathbf{X}) < C_2 \qquad & \textit{Inactive} \\ C_1 \leq g_j(\mathbf{X}) \leq C_2 \qquad & \textit{Active} \\ g_j(\mathbf{X}) > C_1 \qquad & \textit{Violated} \end{aligned}$$

where C_2 is a small negative number and C_1 is a small positive number.

Each of these cases are dealt with separately. At the beginning of the optimization process, mostly there are no active or violated constraints. A steepest descent direction is utilized for the first search direction at any time. For the following steps, conjugate search direction is more precise. The Fletcher-Reeves conjugate direction method is chosen. This method indicates a very simple alteration to the basic steepest descent algorithm but gives a major increase in efficiency. In conjugate direction search each search direction includes the steepest descent direction plus some portion of the preceding search direction. The Fletcher-Reeves conjugate direction method is described as:

$$\mathbf{S}^i = -\Delta F(\mathbf{X}^{i-1}) + \frac{|\Delta F(\mathbf{X}^{i-1})|^2}{|\Delta F(\mathbf{X}^{i-2})|^2}\beta \mathbf{S}^{i-1} \tag{16}$$

If there is an active constraint but no violated constraints finding the search direction, a new optimization sub-problem will be needed, and is defined as:

$$\begin{aligned} &Min\ \Delta f(X^{i-1})^T\mathbf{S}^i \\ &\text{Subject to:} \\ &\Delta g_j(X^{i-1})^T\mathbf{S}^i \leq 0, \quad j\varepsilon J_c \\ &(\mathbf{S}^i)^T\mathbf{S}^i \leq 1 \end{aligned} \tag{17}$$

In the case of one or more constraints violated, a new parameter ,Λ, is added to the direction finding problem, and the sub optimization problem changes in to finding the search direction and the artificial parameter Λ:

$$\begin{aligned} &Min\ \Delta f(X^{i-1})^T\mathbf{S}^i - \Phi\Lambda \\ &\text{Subject to:} \\ &\Delta g_j(X^{i-1})^T\mathbf{S}^i + \Theta_j\Lambda \leq 0, \quad j\varepsilon J_c \\ &(\mathbf{S}^i)^T\mathbf{S}^i + \Lambda^2 \leq 1 \end{aligned} \tag{18}$$

For further information about the choice of these parameters and usage, see the VisualDOC manual[40].

After finding a usable-feasible search direction, the problem now becomes one of determining the step size parameter using the approximate Lagrangian function.To find the Lagrange multipliers,μ_j:

$$Min\ f(\mathbf{X}) + \sum_{j=1}^{M} \vartheta_j max[0, g_j(\mathbf{X})] \tag{19}$$

where

$$\mathbf{X} = \mathbf{X}^{i-1} + \alpha\mathbf{S}$$

$$\vartheta_j = |\mu_j|, \qquad j = 1, M \quad \text{at the first iteration}$$

$$\vartheta_j = max\left[|\mu_j|, \frac{1}{2}(\vartheta_j' + |\mu_j|)\right], \quad j = 1, M \quad \text{at the subsequent iterations}$$

where $\vartheta_j' = \vartheta_j$ from the preceding iteration. After the one-dimensional search is complete, the Hessian of the Lagrangian is updated using the BFGS (Broydon-Fletcher-Goldfarb-Shanno) formula:

$$\bar{\mathbf{H}}^i = \bar{\mathbf{H}}^{i-1} + \frac{\gamma^{i-1}(\gamma^{i-1})^T}{(\eta^{i-1})^T\gamma^{i-1}} - \frac{(\bar{\mathbf{H}}^{i-1})^T\eta^{i-1}(\eta^{i-1})^T\bar{\mathbf{H}}^{i-1}}{(\eta^{i-1})^T\bar{\mathbf{H}}^{i-1}\eta^{i-1}} \tag{20}$$

where

$$\eta^{i-1} = \mathbf{X}^i - \mathbf{X}^{i-1}$$

$$\gamma^i = \Theta\sigma + (1-\Theta)\bar{\mathbf{H}}^i\eta^i$$

$$\sigma = \nabla L^i - \nabla L^{i-1}$$

$$\Theta = \left\{ \begin{array}{rl} 1, & \text{if } \eta\sigma \geq 0.2\eta^T\bar{\mathbf{H}}\eta \\ \frac{0.8\eta^T\bar{\mathbf{H}}\eta}{\eta^T\bar{\mathbf{H}}\eta - \eta\sigma} & \text{if } \eta\sigma < 0.2\eta^T\bar{\mathbf{H}}\eta \end{array} \right\} \tag{21}$$

IV.2 NON-GRADIENT BASED OPTIMIZATION

IV.2.1 Vibrational Genetic Algorithm

The Vibrational genetic algorithm described by *Pehlivanoglu* and Baysal[44] is an iterative algorithm. Within the algorithm an initial population is generated by using a random number operator based on baseline shape or parameters. To describe the method mathematically, let S be the population size, D be the individual (or chromosome) dimension space, f be the objective function, and $\mathbf{Z}_i$ be the current vector including genes, $z_{i,j}(t)$, described in t^{th} iteration:

$$\mathbf{Z}_i(t) = (z_{i,1}(t), z_{i,2}(t), ..., z_{i,D}(t)), \quad z_{i,j}(t) \in R^D, ^{i=1,2,...,S} \tag{22}$$

The second step is to evaluate the fitness of the current population via a defined cost function f. Then, the cost weighting fitness scaling and roulette selection procedure[45] for mating are determined. The elitism concept is applied next to ensure that the best objective function value within a population is not reduced from one generation to the next. The procedure for the elite fitness value, f_ε, and elite individual, Z_ε, is as follows:

$$f_\varepsilon(t) = argmin_{Z_i(t)} f(t) \;\; and \;\; \mathbf{Z}_\varepsilon(t) = \mathbf{Z}_i(t) \tag{23}$$

$$\mathbf{Z}^\varepsilon(t) = \left\{ \begin{array}{rl} \mathbf{Z}^\varepsilon(t-1), & \text{if } f^\varepsilon(t) > f^\varepsilon(t-1) \\ \mathbf{Z}^\varepsilon(t), & \text{if } f^\varepsilon(t) \leq f^\varepsilon(t-1) \end{array} \right\} \tag{24}$$

The crossover technique denoted by $BLX - \theta$ [46] with $\theta = 0.5$, is applied for the new individuals. The Vibrational mutation strategy is applied right after this crossover phase. At this step, there are two tools. As the first tool, the goal of the first mutation application is to provide a global random diversity in the population. For this reason, all the genes in all the chromosomes are mutated as follows:

$$z_{i,j}(t) = \left\{ \begin{array}{rl} z_{i,j}(t)[1 + w_1\beta_1(1-u)]_{j=1,2,....D}^{i=1,2,....S}, & \text{if } t = nf_1, n = 1, 2, ... \\ z_{i,j}(t), & \text{if } t \neq nf_1, n = 1, 2, ... \end{array} \right\} \tag{25}$$

where f_1 is the application frequency, β_1[?] is a user defined amplitude parameter, u is a random real number between (0-1), and w_1 is a user defined scale factor. Implementing the mutation starts from the first gene position of the first chromosome, and continues throughout the genes at the same positions in the other chromosomes. As a second tool, the goal of the second mutation application is to provide a local but controlled diversity in the population. A neural network application can be used to provide a local-controlled diversity within the population. In the neural network application, all the genes of an elite individual are mutated as follows:

$$P_{i,j}(t) = \left\{ \begin{array}{rl} z_j^\varepsilon(t)[1 + w_2\beta_2(1-u)], & \text{if } t = nf_2, n = 1, 2, ... \\ z_j^\varepsilon(t), & \text{if } t \neq nf_1, n = 1, 2, ... \end{array} \right\}_{j=1,2,....D}^{i=1,2,...N} \tag{26}$$

where u is a random real number between (0-1), β_2 is a user-defined constant amplitude, and f_2 is the second application frequency. A newly generated temporal population $\mathbf{P}$ includes $\mathbf{N}$ individuals. The objective function values of this population, $\mathbf{f}^{NN}$, are predicted via trained neural network function, N_{func}, and the best I of them are randomly placed within the population:

$$\mathbf{f}^{NN} = N_{func}(\mathbf{P})$$

$$[\mathbf{f}^{NN} order] = sort(\mathbf{f}^{NN}) \tag{27}$$

$$(Z_k(t))_i = \mathbf{P}_{order(i)_{i=1,2,\ldots,I}^{k=rand[1-D]}}$$

The frequencies f_1, f_2, and I are user-defined constants. In the applications the Matlab routine *newrb* is used as N_{func} [47]. After mutation operations, the new population is evaluated via the cost function which is determined by the real flow solver. The algorithm repeats all of the above steps as necessary until the convergence criterion are satisfied.

CHAPTER V

ACTIVE CONTROL OF SHOCKS APPLICATIONS

V.1 OPTIMIZATION OF ACTIVE FLOW CONTROL OF AN AIRFOIL

V.1.1 Introduction

AFC has been the subject of major research areas in fluid mechanics for the past two decades. It offers new solutions for boundary-layer separation delay or prevention, mitigation of shock strength, drag minimization[48], fluidic thrust vectoring[2], reducing blade-vortex interaction noise in helicopters, stall control[49] and performance maximization of existing designs to meet the increasing requirements of the aircraft industry.

The desired goal in this study was to improve the aerodynamic performance on an airfoil in transonic flow conditions by using actuation in the form of steady suction/blowing on an airfoil. The impacts of control location, width, angle, and speed of suction/blowing were analyzed. Computations were performed for flow past a *NACA-64A010*in transonic flow at Mach 0.78, angle of attack 0.5^0 with and without AFC. The *NACA-64A010* airfoil was tested by Smith and Walker [21] at transonic speeds with surface suction. This test was used to validate the numerical study. Then, a parametric study, interested in the influences of mass flow coefficient, suction/blowing angle, location and width of the actuator was performed on the different configurations. After the parametric study, primarily a gradient-based optimization technique is used to optimize the control variables. Additionally a non gradient based optimization algorithm, vibrational genetic algorithm [44], is used to validate the global optimality of the results found by the gradient-based optimization method. The optimizations were carried out by coupling an automatic algorithm and a widely-used Navier-Stokes solver [35]. The single variable and multiple variable optimization processes were done. For single variable optimization, just one parameter was optimized and the others were kept constant. The well-founded optimum design variables were determined within the control parameter range. Eventually, the optimum parameters were used as an initial value for the multiple-variable optimization.

V.1.2 Optimization Methodologies

The objective of optimization was to maximize the lift-to-drag ratio of a *NACA-64A010* airfoil at a given angle of attack varying mass flow coefficient, actuator angle with respect to the wall, location and width of the actuator as the design variables. The objectives of AFC may cause conflict as the achievement of one desired goal may adversely affect another goal. Thus, the decision of design parameters of the actuators is important for AFC. Optimization methods may be classified as gradient-based or non-gradient based. Traditionally, gradient-based methods are preferred, though the requirement for computing gradient information can often result in prohibitive costs. However, non-gradient based algorithms, such as genetic algorithm and particle swarm optimization have also attracted significant attention in research. Among many optimization strategies available the gradient-based optimization algorithm has been selected as the primary optimization method because it is reasonably efficient and allows flexibility in formulating the design problem [40]. Additionally, the vibrational genetic algorithm (VGA) is applied for the multi-variable case to ensure that the initial points selected for gradient-based algorithm are close enough to capture the global optimal design variables.

V.1.3 Grid Generation

Two dimensional, 10% thick symmetric *NACA-64A010* airfoil was utilized. The computational grid was clustered in the normal direction and in the in the vicinity of jets to resolve the details of the flow. The resolution of the utilized C-type computational grid was $429x121$. Normal spacing for the first grid line of the surface of the airfoil was $0.000001c$ to ensure that the near wall $y+$ values of the airfoil blocks kept in appropriate range. Fig. 3 shows the grid clustering on the upper surface of the *NACA-64A010* airfoil to simulate the jets. The actuator sits in a much refined region downstream of the shock position, 0.51 x/c. The domain was decomposed into four blocks to make the computations parallel. The cases are run at Old Dominion University's teraflop computer cluster.

V.1.4 Validation and Grid Sensitivity

The *NACA-64A010* aerofoil was tested by Smith and Walker[21](1960) at different transonic speeds with surface mass injection downstream of the hinge line of the

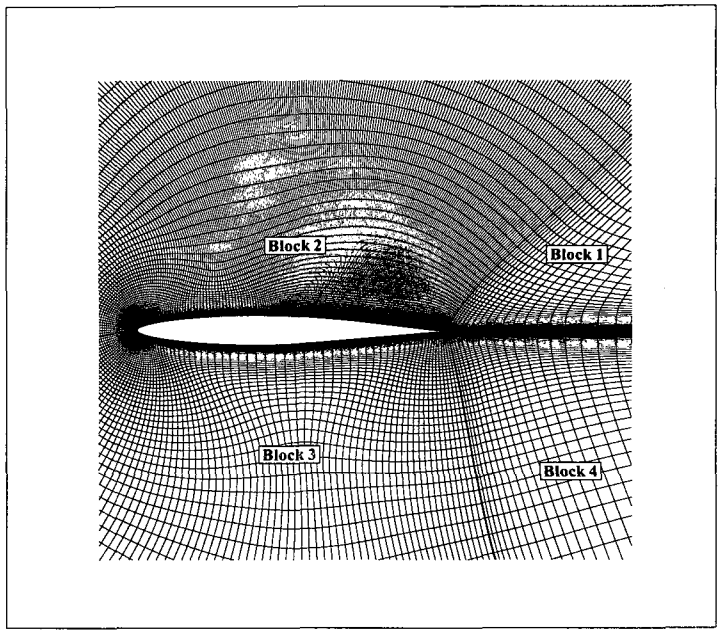

FIG. 3: Computational grid used in the 2D simulations

trailing edge flap. The validation case used in this study had a Reynolds number of 2.9 million based on aerofoil chord, $M_\infty = 0.78, \alpha = 0.50$ corresponding to one of the wind tunnel experiments. The region of suction was located between $0.69c$ and $0.725c$ which is downstream of the shock position. The suction coefficient was 0.06429 and the suction angle was 84^0 to the airfoil surface, since the suction is normal to the chord line [22]. The suction coefficient through the porous area specified in this simulation is different from the experimental value because of the definition of mass flow coefficient. In the present study, the mass flow coefficient equation does not include the ratio of slot width to the airfoil chord in order to investigate the impact of the changes of the slot width.

Fig. 4 shows the comparison of the pressure distributions for both computation and experiment with and without flow control. Also, solution sensitivity to the grid used in this study is illustrated in Table 1. In the numerical tests, three sets of grids have been used. y^+ values, based on the height of the first wall-bounded cell, are below unity for all the meshes considered here. The solutions obtained on the course and fine grids are reasonably good. The results obtained on these three different grid sizes are reasonably grid-converged results and prove the little solution

TABLE 1: Grid sensitivity for NACA64A010 aerofoil test cases

Grid Size	C_L	C_D
Without control		
$449 * 121$	0.2121	0.01049
$241 * 121$	0.2084	0.01075
$241 * 69$	0.2121	0.01071
Experiment[21]	0.2000	0.01300
Computation[50]	0.2166	0.01110
With control		
$449 * 121$	0.2821	0.01406
$241 * 121$	0.2712	0.01385
$241 * 69$	0.2751	0.01378
Experiment[21]	0.2400	0.0140
Computation[50]	0.27950	0.0138

sensitivity. The results are seen to be in qualitative agreement with the experiment. As can be seen from Table 1, the measured lift for the control case and drag for the non-control values are different than the present results. This may be due to the fixtures mounted on the aerofoil in the experiment, which was not calculated for in the computation[50].

V.1.5 Problem Parameterizations and Parametric Study

A parametric study, interested in the influences of mass flow coefficient,C_q, center location of jet, x_c, width of actuator, w_d, and suction/blowing angle relative to the local normal, β, was presented as displayed in Fig. 6. These parameters were selected in order to understand the key ones that affect the performance of the airfoil at transonic speeds.

AFC actuator parameters were allowed to fluctuate in the following ranges in Eq. 33:

$$\begin{aligned} -0.5 \leq C_q \leq 0.05 \\ 3^0 \leq \beta \leq 176^0 \\ 0.01c \leq x_c \leq 0.99c \\ 0.01c \leq w_d \leq 0.095c \end{aligned} \tag{28}$$

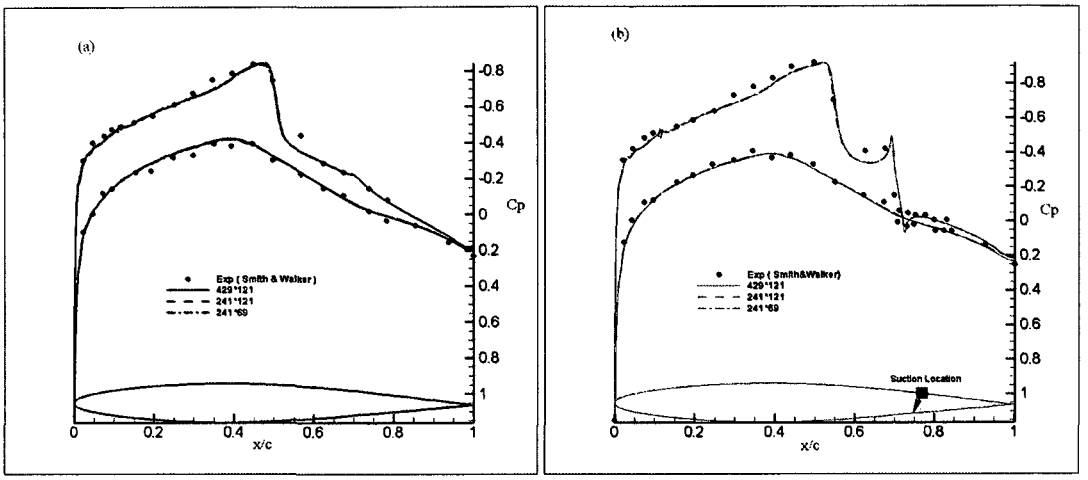

FIG. 4: Comparison of pressure distributions for *NACA-64A010* aerofoil (a)without and (b)with suction

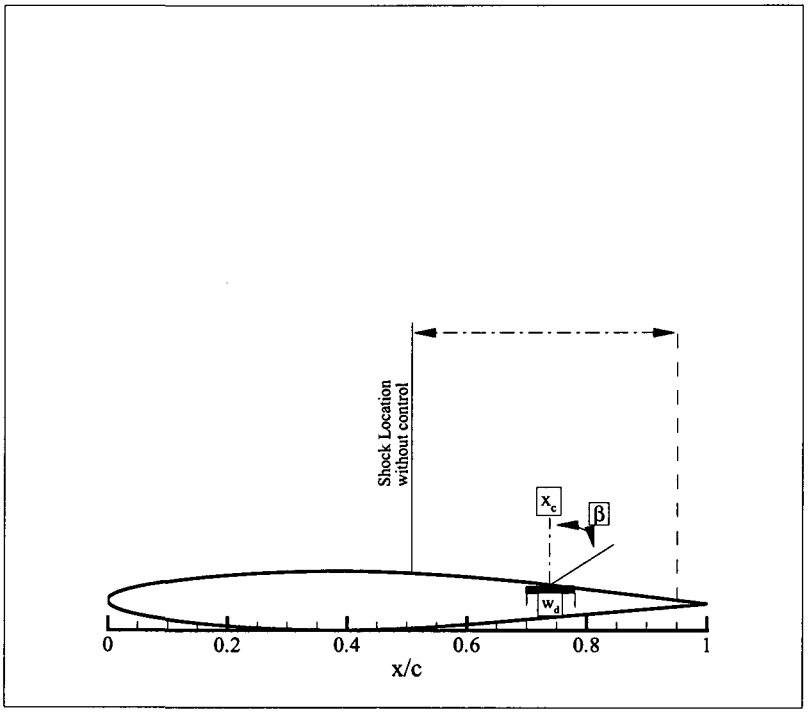

FIG. 5: AFC actuator installed on the upper surface of the airfoil

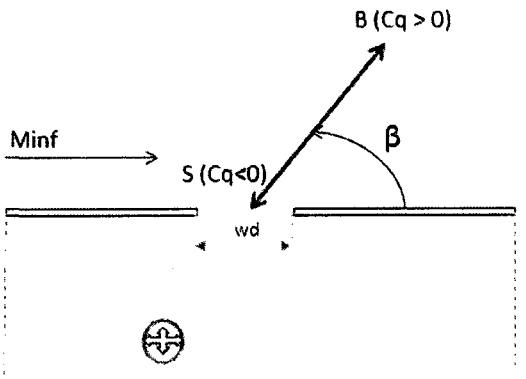

FIG. 6: Parameterizations of AFC actuator

Impact of actuator width (w_d) on C_L/C_d

The suction/blowing jet involves many control parameters. For the convenience of analysis, one parameter was changed while the rest were kept constant. The calculation results illustrate that the variation in the actuator width affects the lift-to-drag ratio and pressure distribution over the airfoil. The actuator width, w_d, was changed over the parameter range of interest between 0.025 and $0.095x/c$ to gain more understanding the impact of the actuator width. Also, two different C_q values were performed to observe the interaction between these two variables. Fig. 7 indicates the variation in lift-to-drag ratio with slot width. As seen in Fig. 7(a), higher width with lower C_q values gives better L/D ratio during the suction. Shown in Fig. 7(b), in contrast to steady suction, lift-to-drag ratio rapidly decreases while the width increases during the injection because of the huge increment in drag value. Fig. 8 illustrates the width effect on pressure distribution over the airfoil. Fig. 8(a) indicates that the shock position gradually moves toward the trailing edge with the increase of the jet width. However, when blowing was performed at the wall, the jet width was affected in a contrary way. Fig. 8(b) shows that the wide actuator pushes the shock to the upstream while performing the blowing.

Impact of mass flow coefficient (C_q) on C_L/C_d

Among all AFC actuator parameters, a crucial one is the mass flow coefficient, C_q. Fig. 7(a) depicts that the effect of C_q is sensitive to the actuator angle. Mass

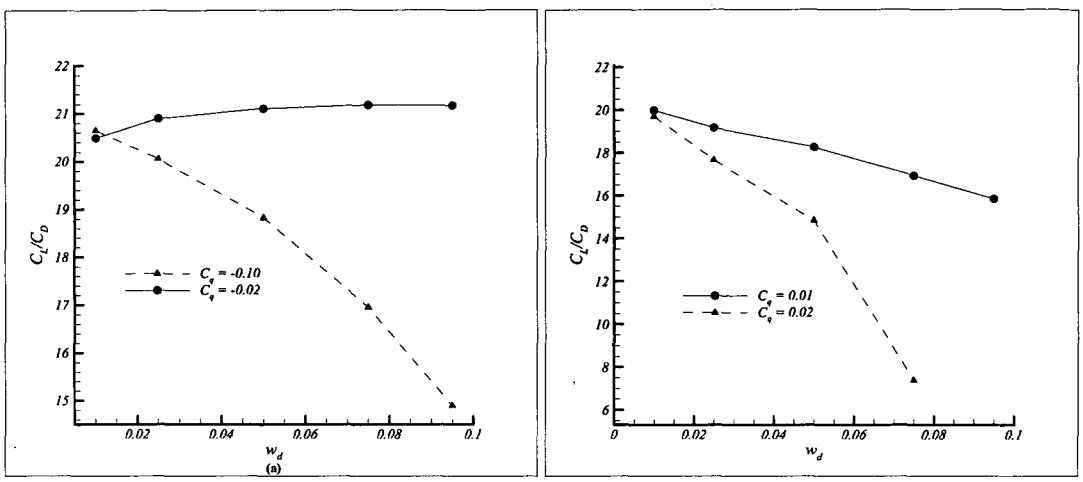

FIG. 7: Effect of actuator width with (a)suction and (b)blowing ($\beta = 45^0$, x_c=0.715c)

removing and injection cases are investigated separately by using different actuator angles with constant location and width of the actuator. The results shown in Figures 9 and 10 have indicated that C_q has an important effect on the lift-to-drag ratio and airfoil surface pressure distribution. Analyses were carried out by changing C_q values from -0.15 to 0.02. As in Fig. 9(a), the effect of steady suction depends on the actuator angle. The stronger suction with actuator angles from 45^0 to 135^0 increases drag value resulting in a decrement in the L/D ratio. Increasing suction speed pulls the shock further downstream and increases both the lift and drag values. The lift increase is more substantial, resulting in an increase in the L/D ratio, when the actuator angle is from 45^0 to 3^0.

On the other hand, stronger blowing pushes the shock upstream with a degradation of the aerodynamic performance but reduces the shock strength. Higher blowing speed with angle from 45^0 to 135^0 rapidly decreases the L/D ratio. When the blowing coefficient is higher, the L/D ratio decreases slowly after 135^0

Impact of location (x_c) on C_L/C_D

At this point, the impact of location of the suction/blowing actuator relative to the shock position was investigated. The range for the location is selected downstream of the transonic shock wave, $0.55 - 0.95x/c$. This range is divided into five intervals and the analyses are run at these locations while the other parameters are kept at

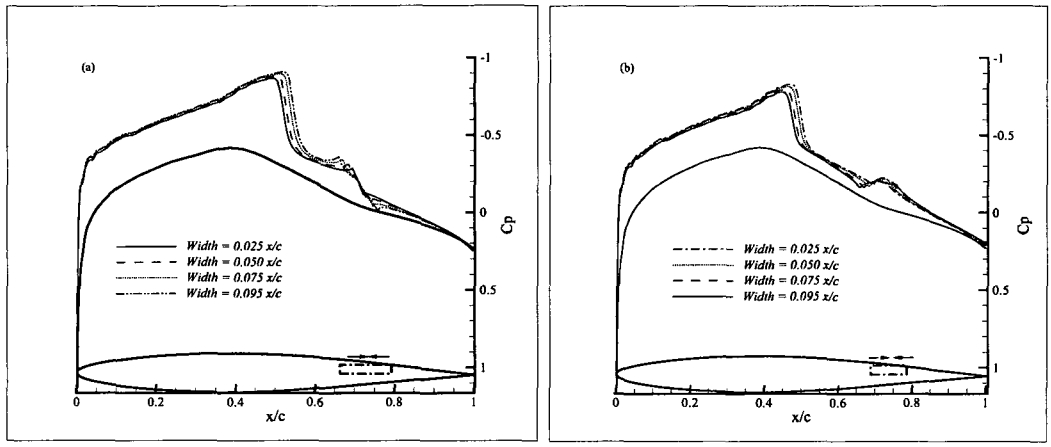

FIG. 8: Pressure Distributions for five different width values with (a)suction (C_q=-0.02) and (b)blowing (C_q=0.01), ($\beta = 45^0$, x_c =0.715c)

their baseline values.

The impact of the actuator location is depicted in Figures 11 and 12. As one can observe from Fig. 12(a), suction changes the local pressure significantly. The effect is especially obvious when suction is close to shock wave. The aerodynamic performance of airfoil was increased when the suction was performed at the downstream of the shock position. However, when the suction was located close to the shock, the aerofoil performance was reduced. Fig. 11(b) shows that blowing more downstream of the original shock can also trim down the shock strength by moving it upstream. Blowing close to the trailing edge was found to reduce the aerodynamic performance considerably. The blowing studies reveal that for the presence of mass injection control downstream of the shock wave, both lift and drag were decreased.

Impact of angle (β) on C_L/C_D

Actuator angle has an important impact on the performance of AFC actuator. The angle was defined as the angle between the actuator flow direction and the local aerofoil surface tangent. The effect of the actuator angle was investigated by changing the angle from 3^0 to 177^0 while the other design variables were kept constant.

All parameters of the AFC actuator have a non-linear relationship with each other. Pressure distributions and the lift-to-drag ratio are plotted against the actuator angles in Figures 13 and 14. AS shown in Fig. 13(a), when the mass flow

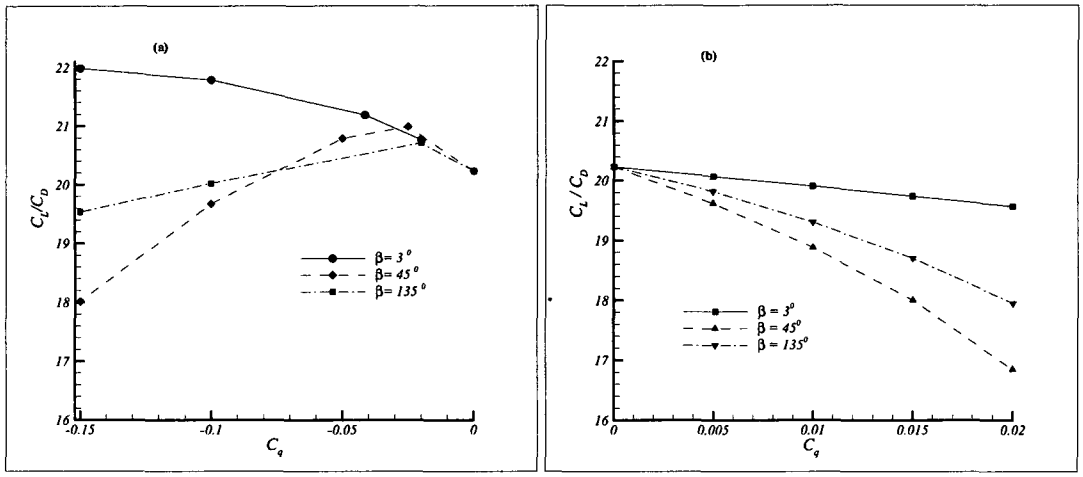

FIG. 9: Effect of C_q with (a)suction and (b)blowing (w_d=0.035 x/c, x_c=0.715c)

coefficient is equal to -0.1 and the actuator angle is normal to airfoil surface, lift-to-drag ratio is decreased rapidly because of the increment in drag value. The surface suction downstream of the transonic shock wave with a higher C_q value and an angle from 70^0 to 110^0 increases the drag rather than the lift of the airfoil. When the actuator angle is 70^0, the drag value begins to decrease with an increment in lift. And at the 3^0 actuator angle, almost tangent to the surface, the lift-to-drag ratio is greatly enhanced. The effect of the angle shows an opposite behavior with lower C_q values. A significant non-linear relationship has been observed between the effect of the actuator angle and mass flow coefficient. It can be seen from Fig 13(b) and 14(b), in contrast to steady suction, blowing decreases the L/D ratio.

V.1.6 Optimization Results

The parametric study shows that the variation in the actuator width, mass flow coefficient, angle, and location may affect the shock strength and overall aerodynamic performance of an airfoil. The considerable variation between retrieved results showed that the parameters effectiveness correlate with each other. In this section, optimization studies have been carried out to investigate the benefits of AFC to improve the aerodynamic performance of *NACA-64A010* at transonic speed. The primary objective of the optimization is to maximize the lift-to-drag ratio, up to the performance of the non-control case. First, the performance was optimized for one

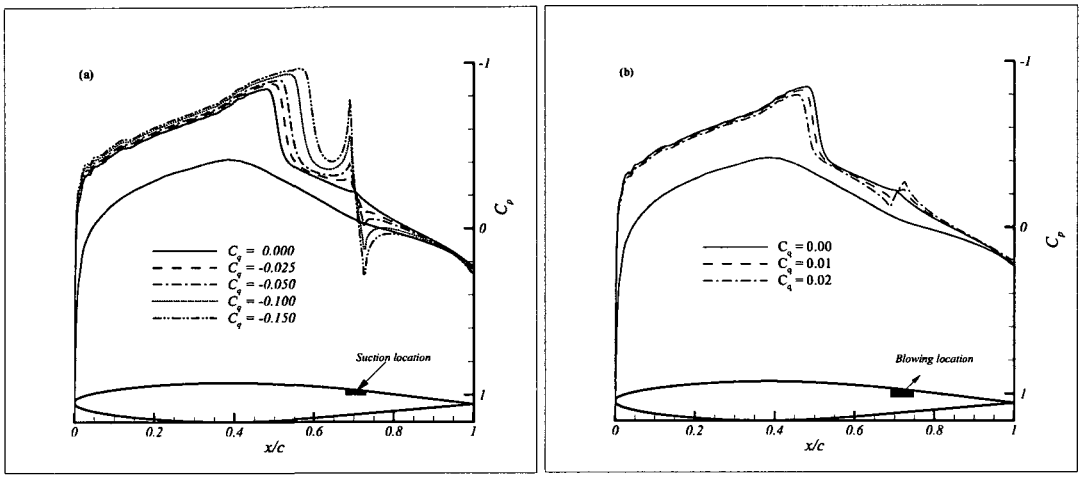

FIG. 10: Pressure Distributions for various C_q values with (a)suction and (b)blowing ($\beta = 45^0$, w_d=0.035 x/c, x_c=0.715c)

actuator parameter at a time while keeping the others constant. In order to achieve more realistic results, multi-variable optimization was also performed over the airfoil surface.

Single - variable optimization

Case 1: Angle (β) Optimization

To improve the performance of the airfoil, in the first step all the design variables except β are kept constant. The optimization problem is defined in the following form :

$$Max\ C_L/C_D\ (\beta)$$

subject to:

$$\begin{aligned} C_L(\beta) &\leq C_{L0}, \\ C_D(\beta) &\leq C_{D0}, \\ \beta^L &\leq \beta \leq \beta^U \end{aligned} \tag{29}$$

In order to better search the design space, four different initial points are used. The initial points and resulting values are given in Table 2. When the initial point is chosen between 90^0 to 177^0, the optimization always converges to a jet angle that

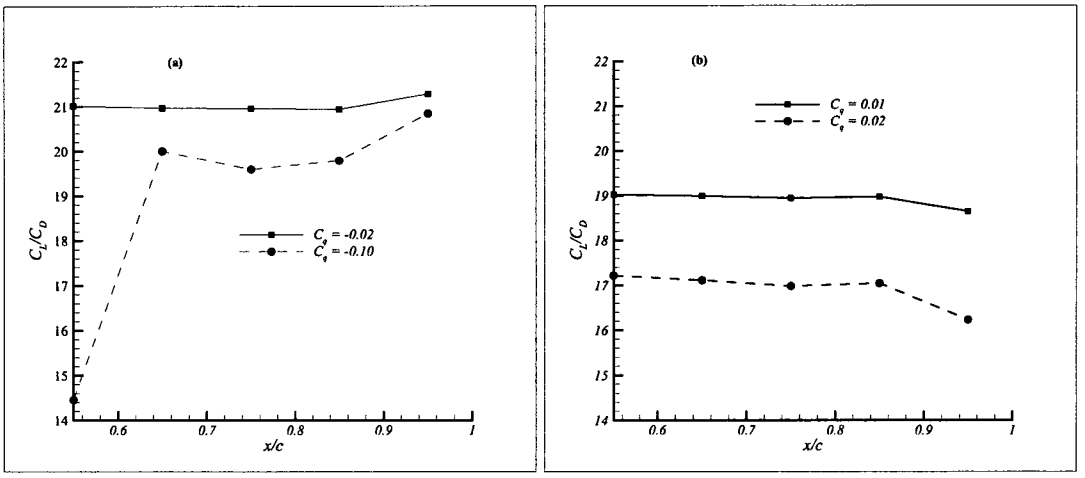

FIG. 11: Effect of location with (a)suction and (b)blowing ($\beta = 45^0$, w_d=0.035c)

produces less lift-to-drag ratio than the non-control case. The optimum jet angle, 155^0, underperforms the non-control case. The initial point is crucial to escape the local minimum for gradient based optimization techniques. The result is quite remarkable indeed; if the initial point is chosen less than 80^0, the optimum one is nearly tangent to the upper surface of airfoil. At the end of the optimization process the resulted optimal values provide 7.76% increase in airfoil performance. Fig.15 shows the plots of the histories for the design variable and objective function for the best optimization process. The optimizer called the solver 6 times for one optimization cycle. The optimizer investigates a one dimensional search which is called sub iteration in the optimization process.

Case 2: Mass Flow Coefficient (C_q) Optimization

As compared with all the parameters studied, the effect of the mass flow coefficient is very important. In this study, C_q is allowed to vary between -0.05 to 0.05 which means that the jet can do suction or blowing depend on the search direction. The optimal jet angle obtained from previous section is used. One case is started from blowing and the other case is started from suction. Two different initial points given in Table 3 are examined, but the same optimal results are obtained. The lift-to-drag ratio is increased 8.91% by using one actuator on optimal or near optimal C_q and β values while the other parameters are kept in baseline values. The best optimization history for case 2 is illustrated in Fig.16. As can be seen, the optimizer called the

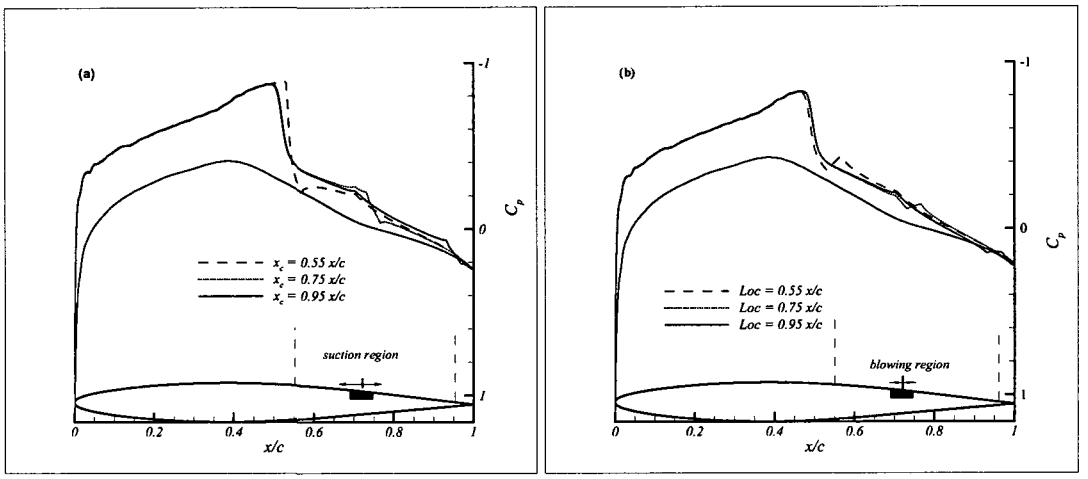

FIG. 12: Pressure distributions for various locations with (a)suction (C_q=-0.02) and (b)blowing (C_q=0.01), ($\beta = 45^0$, w_d=0.035c)

solver 17 times to find the optimal point.

Case 3: Location (x_c) Optimization

Initial location optimization runs have been performed to investigate the influence of the location of the actuator. The actuator is allowed to move between 0.51 – 0.96 x/c. The optimization is started from three different initial points, and the results are given in Table 4. Mass flow coefficient and jet angle are obtained from the previous optimization studies, and width is kept in baseline value. After the optimization, the location is obtained to be close to 0.57 x/c. Consequently, the aerodynamic performance is increased by 12.78% as compared to the non-control case. The steady jet works more effectively when it is located in the vicinity of the shock. The optimization histories for the design variable and objective function are shown in Fig.17.

Case 4: Width (w_d) Optimization

After the optimization of C_q, β and x_c, the other design variable is the width of the actuator. As seen in parametric study, the wide actuator with small suction speeds or a narrow one with high suction speeds can increase the L/D ratio. The two different initial points with optimal C_q^*, β^* and x_c^* values are used to search design variable space. The width value is allowed to vary between 0.01 to 0.095 x/c values. As seen in Fig.18, the actuator works most effectively at an actuator width value around 0.43 and provides 13.62% increase in aerodynamic performance. This result

TABLE 2: Initial and optimal values of angle optimization

	Initial Parameters				
Sub Cases	C_q	β	x_c/c	w_d/c	
1	-0.1	45^0	0.7075	0.035	
2	-0.1	80^0	0.7075	0.035	
3	-0.1	0^0	0.7075	0.035	
4	-0.1	135^0	0.7075	0.035	
	Optimal Results				
	β^*	C_L	C_D	C_L/C_D	%
1*	3.012^0	0.2340	0.01074	21.7877	7.76
2*	3.012^0	0.2340	0.01074	21.7877	7.76
3*	154.84^0	0.2515	0.01245	20.2008	-0.09
4*	155.8^0	0.2481	0.01229	20.1871	-0.16

TABLE 3: Initial and optimal values for mass flow coefficient optimization

	Initial Parameters				
Sub Cases	C_q	β_*	x_c/c	w_d/c	
1	-0.02	3.012^0	0.7075	0.035	
2	0.02	3.012^0	0.7075	0.035	
	Optimal Results				
	C_q^*	C_L	C_D	C_L/C_D	%
1*	-0.1775	0.2473	0.01123	22.0214	8.91
2*	-0.1775	0.2473	0.01123	22.0214	8.91

TABLE 4: Initial and optimal values for mass flow coefficient optimization

	Initial Parameters				
Sub Cases	C_q	β_*	x_c/c	w_d/c	
1	-0.1775	3^0	0.6000	0.035	
2	-0.1775	3^0	0.7075	0.035	
3	-0.1775	3^0	0.9000	0.035	
	Optimal Results				
	x^*/c	C_L	C_D	C_L/C_D	%
1*	0.57048	0.2408	0.01056	22.803	12.78
2*	0.57048	0.2408	0.01056	22.803	12.78
3*	0.56100	0.2392	0.01057	22.630	11.92

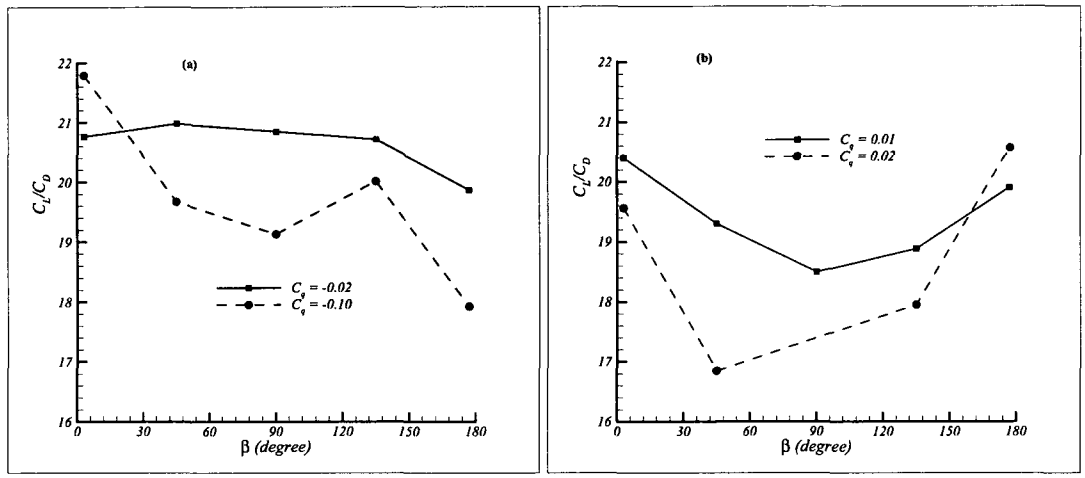

FIG. 13: Effect of angle with (a)suction and (b)blowing (w_d=0.035 x/c. x_c=0.715c)

is expected because the initial suction speed is too high; the actuator width value is decreased. The optimizer calls the solver 10 times during the optimization process.

TABLE 5: Initial and optimal values for mass flow coefficient optimization

	Initial Parameters				
Sub Cases	C_q	β_*	x_c/c	w_d/c	
1	−0.1775	3^0	0.57136	0.060	
2	−0.1775	3^0	0.57136	0.075	
	Optimal Results				
1*	w_d*	C_L	C_D	C_L/C_D	%
2*	0.04394	0.2449	0.01066	22.9737	13.62
3*	0.03375	0.2408	0.01056	22.8030	12.78

Multi - Variable Optimization

The original goal and motivation behind actuator parameter optimization is to determine the optimal ones for improvement in the aerodynamic performance. As discussed earlier, the parameters' effectiveness correlate with each other. For this reason, all the parameters need to optimize together to obtain a more realistic result.

1.Single-jet Control System Optimization

First, the optimization process of the single-jet four-parameter control system is studied. The optimal results obtained from the single variable optimizations are used

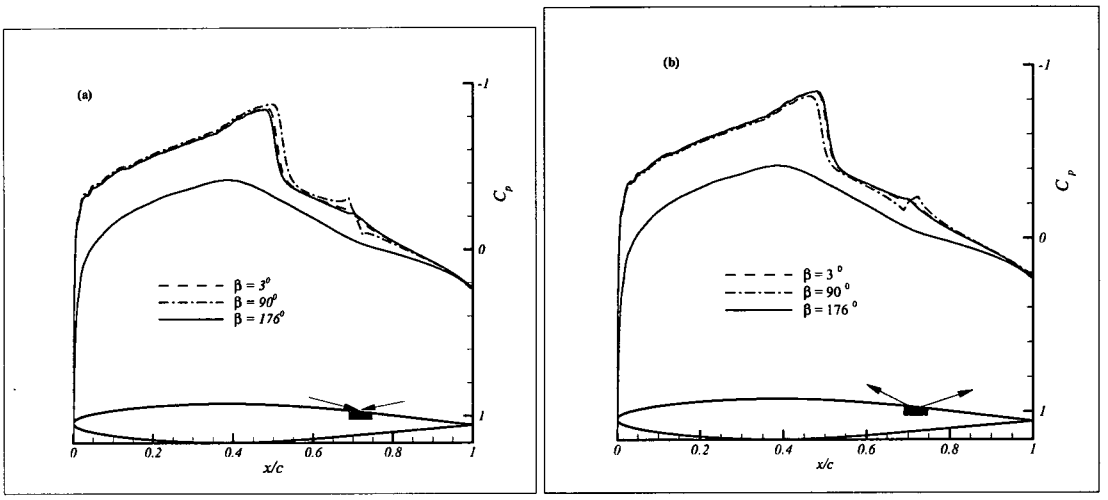

FIG. 14: Pressure distributions for three different angles with (a)suction (C_q=-0.02), and (b)blowing (C_q=0.01), (w_d=0.035 x/c. x_c=0.715c)

for the initial point of SQP, to start close to the global maximum. The optimization problem is defined in the following form:

$$Max\ C_L/C_D\ (C_q, \beta, x_c, w_d)$$

Subject to:

$$\begin{aligned} C_L(C_q, \beta, x_c, w_d) &\leq C_{L0} \\ C_D(C_q, \beta, x_c, w_d) &\leq C_{D0} \\ -0.5 \leq {C_q}^* &\leq 0.05 \\ 3^0 \leq {\beta}^* &\leq 176^0 \\ 0.55c \leq {x_c}^* &\leq 0.96c \\ 0.01c \leq {w_d}^* &\leq 0.1c \end{aligned} \tag{30}$$

From Table 7, one can see that the optimum suction speed is decreased to -0.1259. The actuator is moved away from the initial location. The width of the actuator is increased to almost twice the initial value. The control angle is not changed. After suction at optimal values C_L is increased 21.69%, on the other hand C_D is increased to 2.96% because of the increment in skin friction. As a result, C_L/C_D is increased to 18.195% as compared to non-control case. The optimization

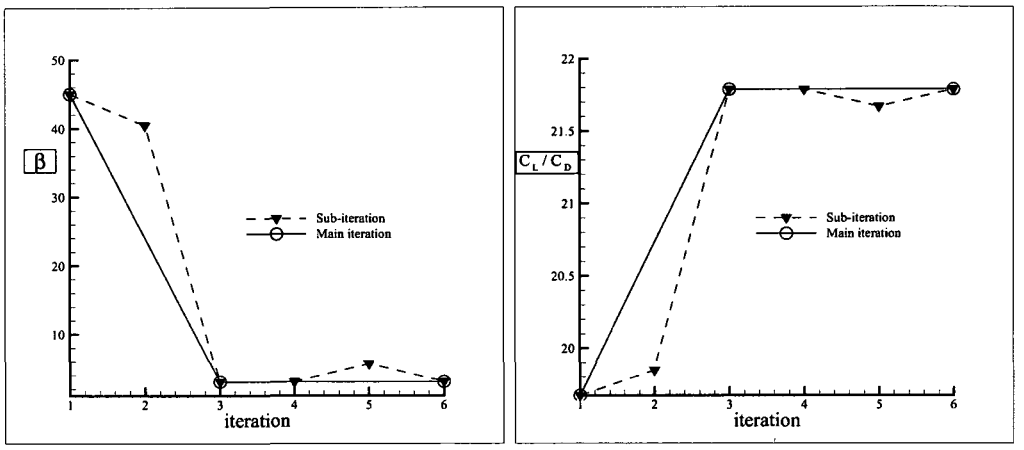

FIG. 15: History of β optimization for *Case* 1; Design Variable:β, Objective function:C_L/C_D, Constant variable:$C_q = C_{q0}$, $x_c = x_{c0}$, $w_d = w_{d0}$

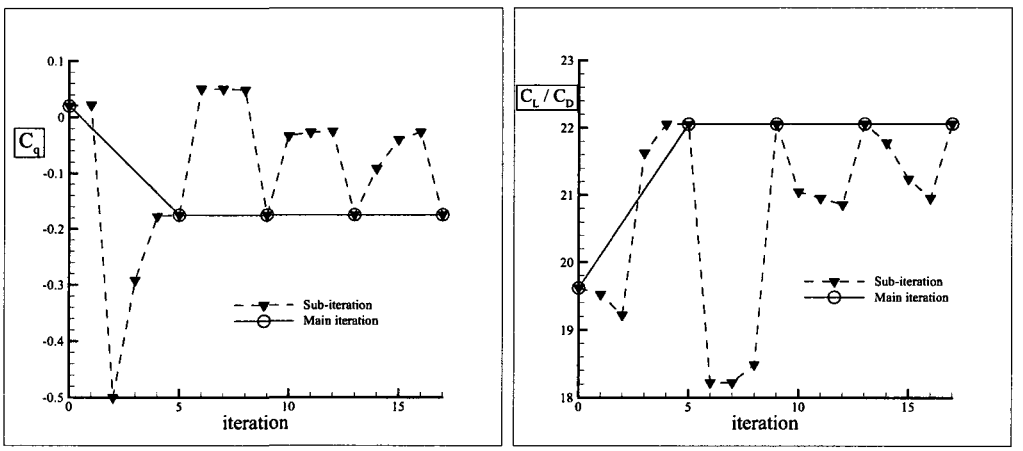

FIG. 16: History of C_q optimization for *Case* 2; Design Variable:C_q, Objective function:C_L/C_D, Constant variable:$\beta = \beta^*$, $x_c = x_{c0}$, $w_d = w_{d0}$

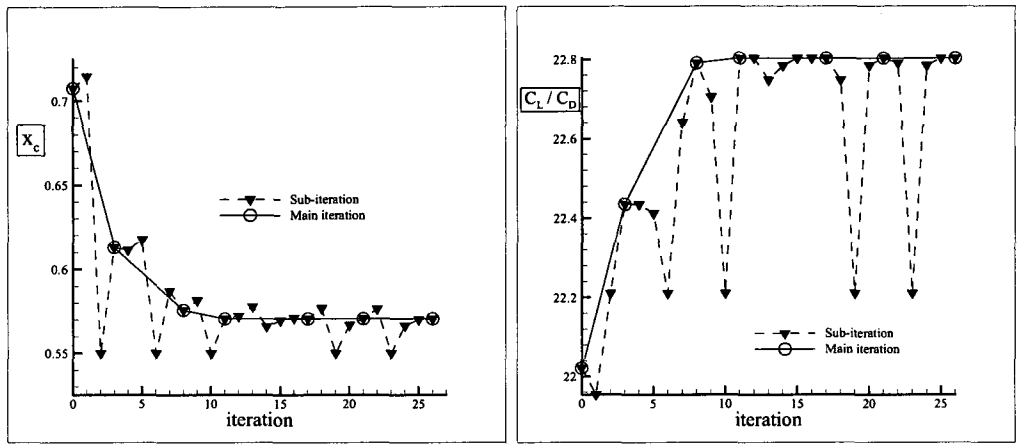

FIG. 17: History of x_c optimization for *Case* 3; Design Variable:x_c, Objective function:C_L/C_D, Constant variable:$\beta = \beta^*$, $C_q = C_q^*$, $w_d = w_{d0}$

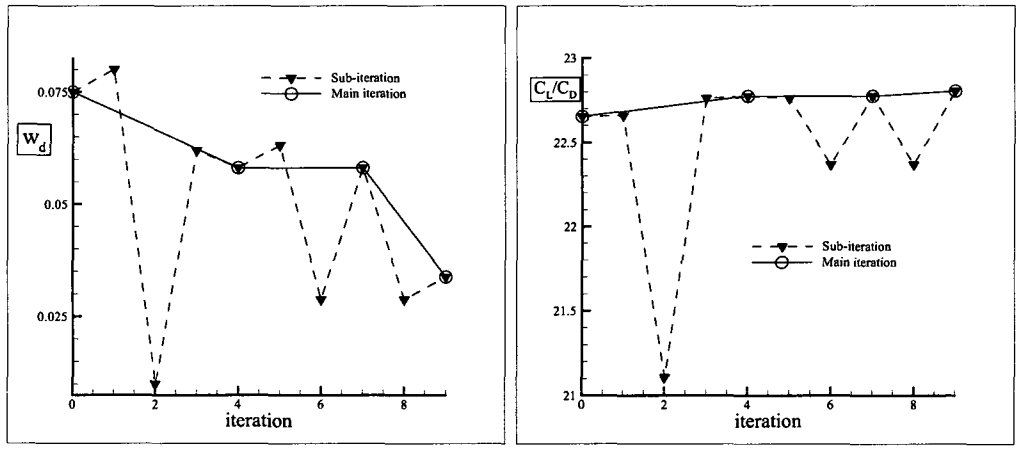

FIG. 18: History of w_d optimization for *Case* 4; Design Variable:w_d, Objective function:C_L/C_D, Constant variable:$\beta = \beta^*$, $C_q = C_q^*$, $x_c = x_c^*$

history for the design variable and the objective function is plotted in Fig.19.a. To make the validation, the same optimization problem is solved by using the genetic algorithm. The features of the genetic algorithm are given in Table 6. As shown in Table 7, although the optimal design parameters are different except control angle, the AFC is found to yield exactly the same aerodynamic performance increment as obtained by using the gradient-based optimization technique. The history of GA is also depicted in Fig.19.b. We also need to point out that suction speed and actuator width values for both optimization processes give almost the same momentum value as 0.010 (C_q, w_d) .

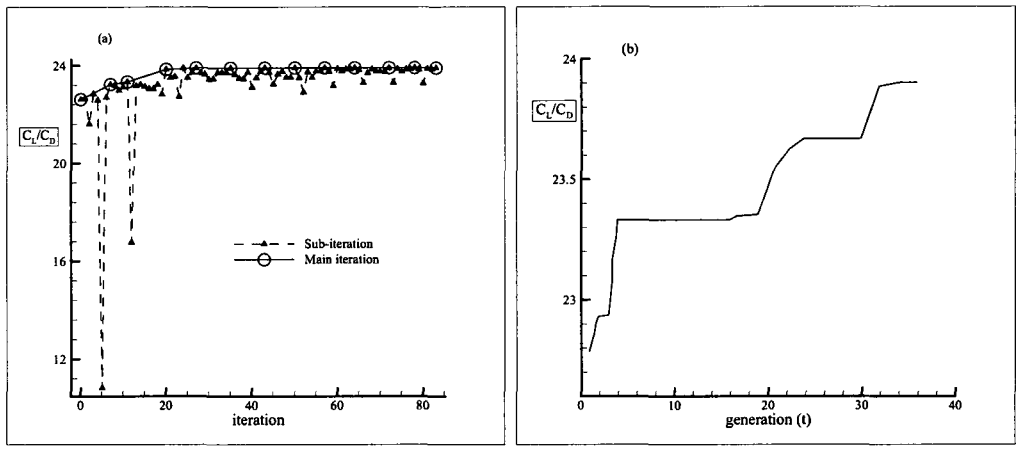

FIG. 19: Optimization history of single-jet control system by using (a)SQP and (b)GA algorithm

TABLE 6: Vibrational genetic algorithm features

mutation	**generation**	**S**
vibrational with f_x 4, w 1, and A 0.5	36	10
fitness scaling	**selection**	**elite count**
rank	roulette	1

2. Multi-jet Control System Optimization

In this section, the effect of actuator numbers on the lift-to-drag ratio is studied. The upper limit for the width of the actuators is reduced to $0.06c$ to give the actuators a more flexible moving location. The other parameters' upper and lower limits are kept the same as in previous cases. Then the optimization problem is defined in the following form:

TABLE 7: Single-jet with multi variable optimization

	Initial Parameters							
method	$C_q{}^*$	β^*	x_c/c^*	w_d/c^*				
SQP	-0.1775	3^0	0.5713	0.043				
GA	-	-	-	-				
	Optimal Results							
	$C_q{}^{**}$	β^{**}	x_c/c^{**}	w_d/c^{**}	C_L	C_D	C_L/C_D	%
SQP	-0.1259	3^0	0.599	0.0806	0.2581	0.01080	23.90	18.195
GA	-0.1480	3^0	0.607	0.0731	0.2615	0.01094	23.90	18.195

$$Max\ C_L/C_D\ (C_q, \beta, x_c, w_d)$$

subject to:

$$\begin{aligned} C_L(C_q, \beta, x_c, w_d) &\leq C_{L0} \\ C_D(C_q, \beta, x_c, w_d) &\leq C_{D0} \\ -0.5 \leq C_q{}^*|^{1,2,3} &\leq 0.05 \\ 3^0 \leq \beta^*|^{1,2,3} &\leq 176^0 \\ 0.55c \leq x_c{}^*|^{1,2,3} &\leq 0.96c \\ 0.01c \leq w_d{}^*|^{1,2,3} &\leq 0.06c \end{aligned} \tag{31}$$

As seen in Table 8, the increment in lift-to-drag ratio is reduced almost 2.25%, because of the reduction in the width of the actuator. After that, the double-jet four-parameter control system is performed to improve the aerodynamic performance of the airfoil. As seen in Table 8, one of the actuators goes to the trailing edge and the other one keeps its location. As it is known from previous cases, high suction speed incredibly increases drag value except when the angle is almost tangent to the airfoil surface. Thus, both of the actuators almost keep their initial angles. The suction speed of the second actuator close to the shock location is decreased, but its width is increased a little. For double-jet control with multi variable optimization, an 18.78% increase is observed as compared to the non-control cases. Finally, an optimization study is performed by using three actuators. The range for mass flow coefficient is decreased to $-0.2 - 0.02$, because a sufficient residual cannot be attained due to the adverse pressure gradient caused by the actuators on the airfoil surface. The initial

points are obtained from the previous study. The control speed of the actuators is not changed much. The optimal values of the design parameters are shown in Table 8. The lift-to-drag ratio is increased 20.06% as compared to the non-control case at the same flow conditions. Mach contours of the non-control case and all multi-jets control cases are plotted in Fig.21.

TABLE 8: Multi variable optimization results

	Initial Parameters							
Act no	$C_q{}^*$	β^*	x_c/c^*	w_d/c^*				
Single-Jet								
1	-0.1775	3^0	0.571	0.043				
Double-Jets								
1	-0.1260	3^0	0.80	0.043				
2	-0.1260	3^0	0.60	0.043				
Triple-Jets								
1	-0.1	3^0	0.93	0.04				
2	-0.1	3^0	0.78	0.04				
3	-0.1	3^0	0.60	0.04				
	Optimal Results							
	$C_q{}^{**}$	β^{**}	x_c/c^{**}	w_d/c^{**}	C_L	C_D	C_L/C_D	%
Single-Jet								
1	-0.1374	3^0	0.584	0.0579	0.2493	0.0106	23.43	15.88
Double-Jets								
1	-0.2007	3^0	0.914	0.0430				
2	-0.0519	3^0	0.599	0.0464	0.2733	0.0114	24.02	18.78
Triple-Jets								
1	-0.1084	3^0	0.941	0.043				
2	-0.1084	3^0	0.763	0.032				
3	-0.1084	3^0	0.618	0.035	0.2990	0.0123	24.28	20.06

V.1.7 Conclusion

Some validation cases have been done against the experimental data regarding pressure distribution and lift and drag coefficients. A grid sensitivity study was performed to ensure the numerical solution accuracy of the governing equations. Then, a parametric study was carried out to understand the physics of control concepts. It demonstrated that the expected improvement in aerodynamic performance were mostly dependent on the mass coefficient, the location and width of the actuator and the jet angle relative to the local tangent. Based on the retrieved results, the following

outstanding conclusions are drawn; the surface suction downstream of the transonic shock wave increases the lift with very little penalty in drag and shock strength. This provides an extended low-pressure region after the shock on the upper surface of the aerofoil. A significant lift augmentation was observed for the present suction control applied at the appropriate angle and location of downstream of the shock wave. Blowing ahead of shock generally was found to reduce the lift-to-drag ratio.

In the second part of this study, a numerical study has been carried out to investigate the benefits of AFC to improve the aerodynamic performance of $2D$ aerofoil, *NACA-64A010*, at transonic speed by using the gradient based optimization technique. The optimization was successfully applied to *NACA-64A010* airfoil with a 1^0 hinged flap and equipped with AFC actuator to improve the aerodynamic performance. An automated optimization cycle was performed, and the computational time was decreased. Unfortunately, the gradient -based optimization method depends on the initial points so that several optimization runs with different initial values needed to escape the local minimum/maximum points. Additionally, a global search optimization method, GA is employed to make sure that the resulted optimal values are global optimal design variables for one-jet control system optimization. For all cases, to obtain the fully converged solutions, the convergence study on residuals and forces was done before passing the response values to the optimization program.

A method based on gradient-based approach is exercised to optimize the actuation parameters of the AFC over an airfoil. Optimization work has three parts: maximize the lift-to-drag ratio of the aerofoil with constraints C_D and C_L, applying one-jet control system optimization with a single variable; using one-jet control system optimization with multi variables; and multi jets control system with multi variables. The single variable optimizations were performed in order to enhance the L/D ratio. First of all, the performance was optimized for jet angle relative to the local normal while keeping the other parameters constant. As compared to the non-control case, the optimization produces 7.76% increment into L/D ratio. The optimal angle is almost tangential to the airfoil surface, 3^0. For the second step, by using this optimum jet angle as an initial point, mass flow coefficient is employed for the optimization. C_q optimizations result in 8.91% increase in the objective function. The same process was done for both location and width of jet. Finally, compared to the non-control case, the single variable optimization produces a 13.62% increase in the aerofoil transonic aerodynamic performance optimizing jet angle, mass flow

coefficient, location and width of the actuator, respectively.

As mentioned earlier, the parameters' effectiveness correlates with each other. In order to obtain the best solution, multi variable optimization was introduced. For the initial point, the optimal results obtained from the single variable optimizations are used. The result indicates that a significant augmentation was observed by using the one-jet four-parameter control system on the downstream of the shock position. The increment was reached to 18.195% with multi variable optimization. Additionally, genetic algorithm is used to validate the results obtained by using gradient based technique. As a result, gradient based optimization and genetic algorithm are converged to the same result with different design parameters

Finally, an optimization study is performed by multi actuators with multi design variables. The upper limit for the width of the actuators is reduced to $0.06c$ to give the actuators more flexible moving location. All the actuators are located downstream of the shock location. The two-jet four-parameter control system optimization results in a 18.78% increase in L/D ratio. Then, the number of the actuators is increased to three. The final lift-to-drag ratio reaches 24.2764 which means 20.06% increments in the aerodynamic performance.

Consequently, to obtain the desired goal without affecting another goal is very crucial in AFC phenomena. In this study, the original goal and motivation behind the application of AFC on *NACA-64A010* airfoil have been fully achieved with very little penalty in drag and shock strength. Based on this study, detailed suggestions are provided to aid in the preparation of a possible future study on AFC with optimization.

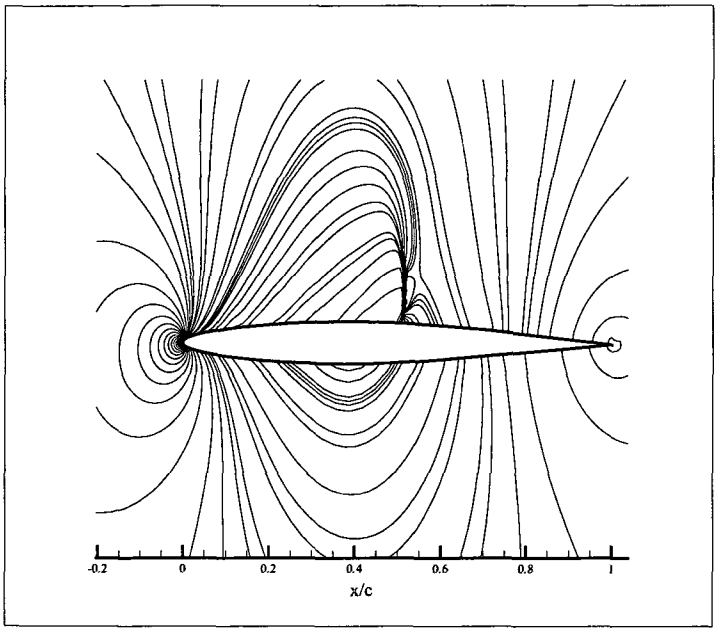

FIG. 20: Mach Contours for no control case

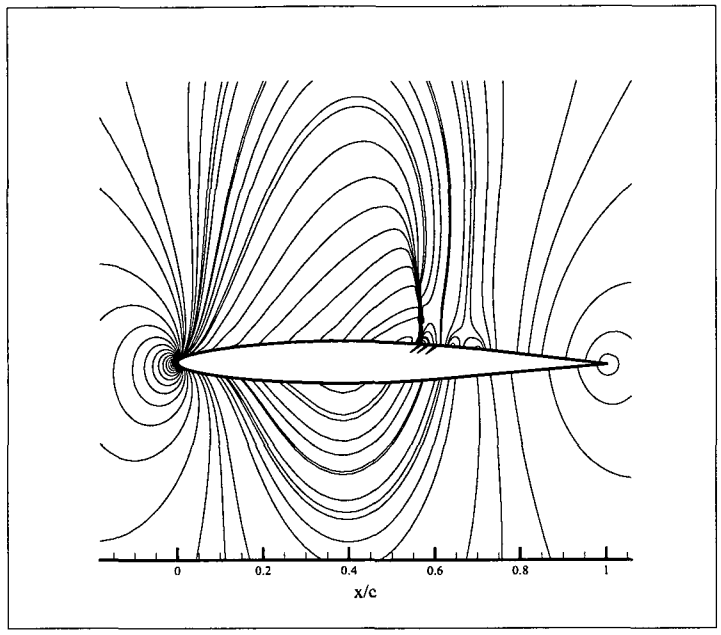

FIG. 21: Mach Contours for single-jet control case

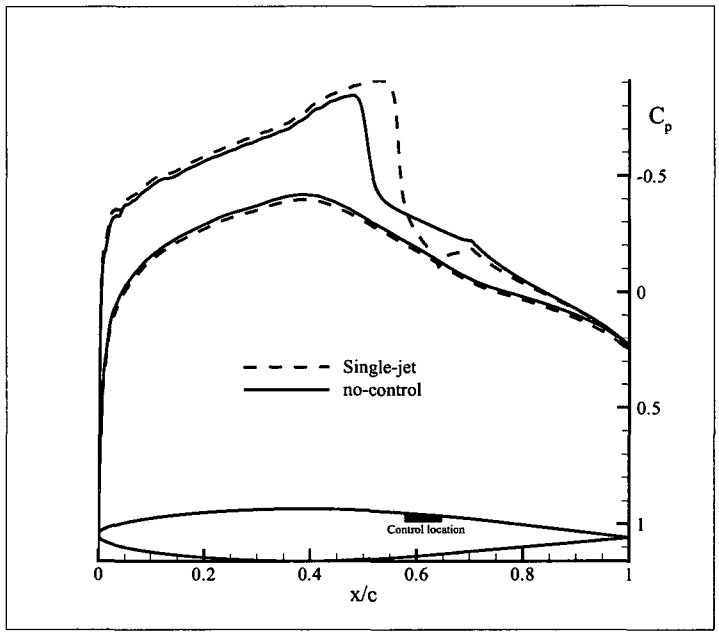

FIG. 22: Pressure distribution for single-jet control case; $C_q^{**} = -0.1374$, $\beta^{**} = 3^0$, $x_c^{**} = 0.584c$, $w_d^{**} = 0.0579c$

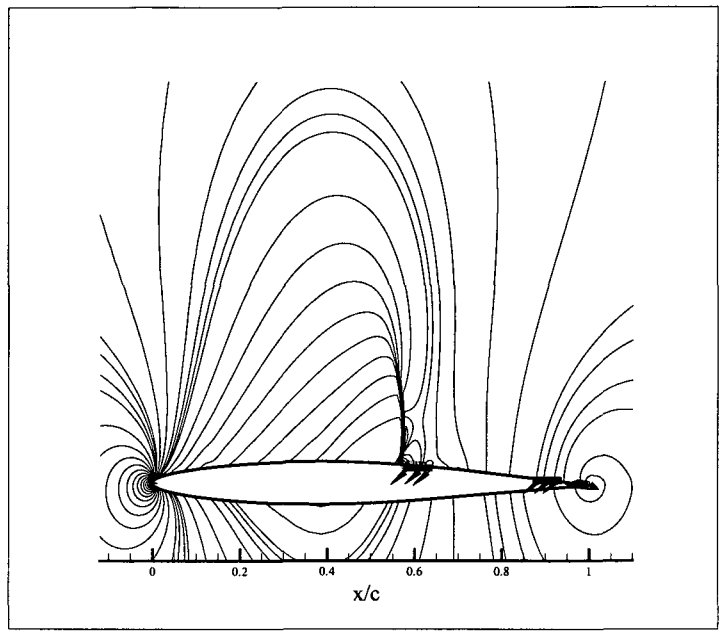

FIG. 23: Mach Contours for double-jet control

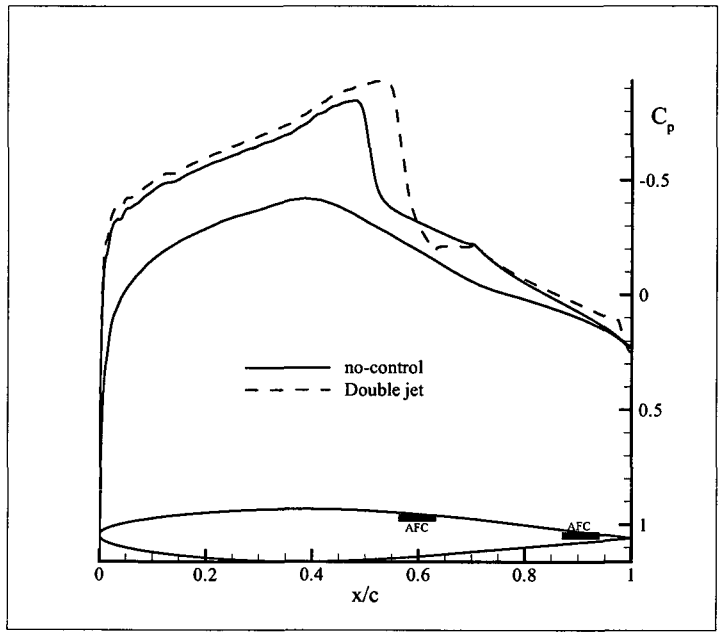

FIG. 24: Pressure distribution for double-jet control; $C_{q1}^{**} = -0.2007$, $\beta_1^{**} = 3^0$, $x_{c1}^{**} = 0.914c$, $w_{d1}^{**} = 0.043c$; $C_{q2}^{**} = -0.0519$, $\beta_2^{**} = 3^0$, $x_{c2}^{**} = 0.599c$, $w_{d2}^{**} = 0.0464c$

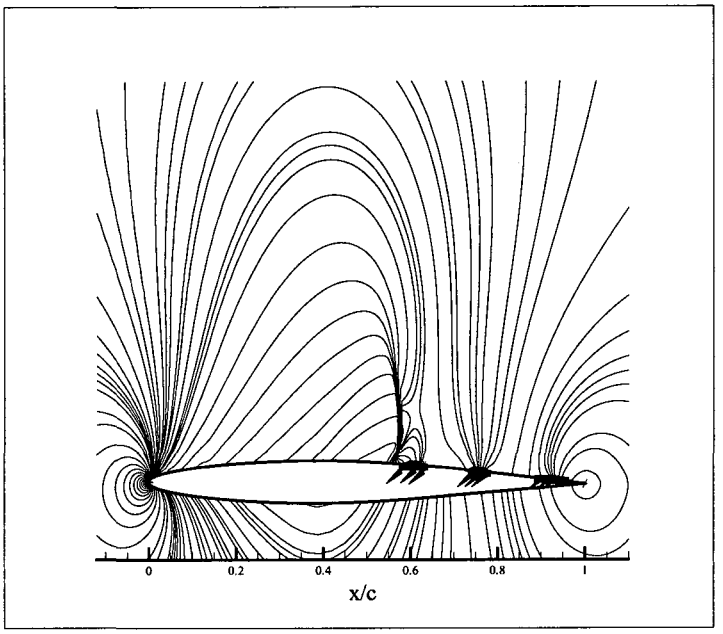

FIG. 25: Mach Contours for triple-jet control

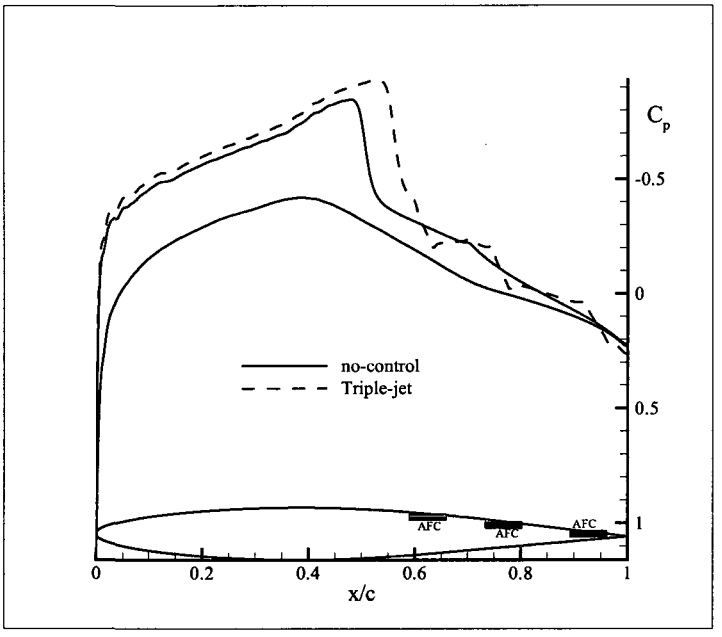

FIG. 26: Pressure distribution for triple-jet control; $C_{q1}^{**} = -0.1084$, $\beta_1^{**} = 3^0$, $x_{c1}^{**} = 0.941c$, $w_{d1}^{**} = 0.043c$; $C_{q2}^{**} = -0.1084$, $\beta_2^{**} = 3^0$, $x_{c2}^{**} = 0.763c$, $w_{d2}^{**} = 0.032c$; $C_{q3}^{**} = -0.1084$, $\beta_3^{**} = 3^0$, $x_{c3}^{**} = 0.618c$, $w_{d3}^{**} = 0.035c$

V.2 DRAG REDUCTION OPTIMIZATION BY USING FLOW CONTROL TECHNIQUES

V.2.1 Introduction

The development of the boundary layer and the interaction of the boundary layer with the outer flow field, aggravated at high speeds by the presence of the shock waves which develops over the lifting surface after the local pocket of supersonic flow, dramatically limit the overall aircraft or aircraft-component performance [51]. Modern civil transport aircraft's cruise speed is brought down for fuel efficiency due to the large drag penalty connected with shock waves inducing an additional drag, namely the wave drag.

Flow control (FC) offers new solutions for the performance maximization of existing designs to meet the increasing requirements of the aircraft industries. FC achieves an augmentation in lift and lift-to-drag ratio; thus, additional improvements in fuel consumption can be gained [15] by decreasing the drag associated with shock waves for transonic and supersonic flight. In addition to profound aerodynamic benefits, FC technology presents a pathway toward higher efficiencies in the aircraft design [52]. To achieve any of these useful end results, a wide range of flow control methods [15] have been proposed and practiced such as passive control by applying a porous surface at the foot of the shock [53], local bump close to the shock [54] and active control by using mass injection or removing [23]. The most common ones, suction/blowing and contour bump on the upper surface of the airfoil, were used in this study.

For the shock control method, 2D contour bump was chosen because it is efficient at reducing wave drag without increasing the skin friction excessively. Stanewsky [53] et al. asserted that a contour bump in the shock region is most effective in reducing wave drag. The shock control bump supersedes the normal transonic shock with near isentropic compression or smear it into multiple weaker shocks like λ-shock structure [55]. A contour bump does not need additional energy input as in the case of suction/blowing to reduce the wave drag [53].

In the literature, there have been numerous studies showed that lift could be increased by application of suction in the vicinity of the shock; however this is obtained with an increase in drag. Injection of momentum accelerates the inviscid outer flow over the airfoil ahead of the shock and induces weak compression waves that soften

the adverse pressure gradient[23]. When the discrete suction is applied to airfoil, the total drag can be considerably reduced, while either the skin friction or wave drag is increased depending on the location of the suction point relative to the shock location.

In this study, these two techniques are utilized individually and then the combination of these two control mechanisms is considered to mitigate the shock wave and hence decrease the total drag. Although the flow control provides such degrees of improvements, the sensibility of aerodynamic performance to design parameters makes it a nontrivial and expensive problem [25], so the designer has to optimize a number of different parameters. Thus, it is crucial to decide the parameters such as maximum height, the length, the position via shock location, and the crest position of the 2D bump and also location, angles, and speed of suction/blowing of actuator during the flow control. The bump could be symmetrical or asymmetrical depending on the location of the bump's crest. Thus, for the purpose of gaining more understanding of the flow control concepts, an automated optimizing cycle process is needed. Also, the optimization cycle reduces cost and turnaround time.

The desired goal in this study is to decrease the total drag in transonic conditions by using actuation in the form of steady suction/blowing and 2D local bump on the upper surface of airfoils. Computations were performed for flow past the *Rae*5243 aerofoil which is a natural laminar flow (NLF) aerofoil with a pressure distribution on the upper surface having a favorable pressure gradient upstream of the shock at about 55% chord in transonic flow at Mach 0.6799, angle of attack 0.77, $Re = 18.68\text{x}10^6$. The *Rae*5243 airfoil was tested by Fulker and Simmons [56] at transonic speeds with surface suction. This test was used to validate the numerical study. Fig. 29 shows the comparisons between numerical values and experimental data. In general, the pressure distributions were found to be in good agreement with the experiment. Then, an efficient method based on the gradient based optimization technique is used to optimize the parameters of the steady suction/blowing jet and contour bump. The optimizations were carried out by coupling an automatic algorithm and an existing Navier-Stokes solver. The current study of gradient based optimization on flow control at transonic speed has been demonstrated to be a prosperous optimization application.

V.2.2 Optimization methodology

The objective of optimization is to minimize drag coefficient of a *Rae*5243 aerofoil under given flow conditions varying design variables of discrete suction and/or $2D$ contour bump. The objectives of flow control may cause conflict as the achievement of one desired goal may adversely affect another goal. Thus, the decision of location, angle and speed of suction/injection of the actuator and also 2D bump parameters including the length, the maximum height, the bump position via shock location, and the crest position via bump over the upper surface of the airfoil is important for the flow control.

In the present study, sequential quadratic programming (SQP) is used to solve the optimization problems. The details of this method are explained in the previous chapter. Fig. 27 provides a brief overview of the computational details of the automated optimization process.

In this study, C_L is defined as a constraint to be sure not to decrease the lift during an optimization process. As mentioned before, the gradient based optimization technique sensitive to the initial points so that approximately 15 initial points were used for every case. On the whole, the overall aerodynamic performance increment was also considered while choosing the best design point among the optimization results obtained in search space.

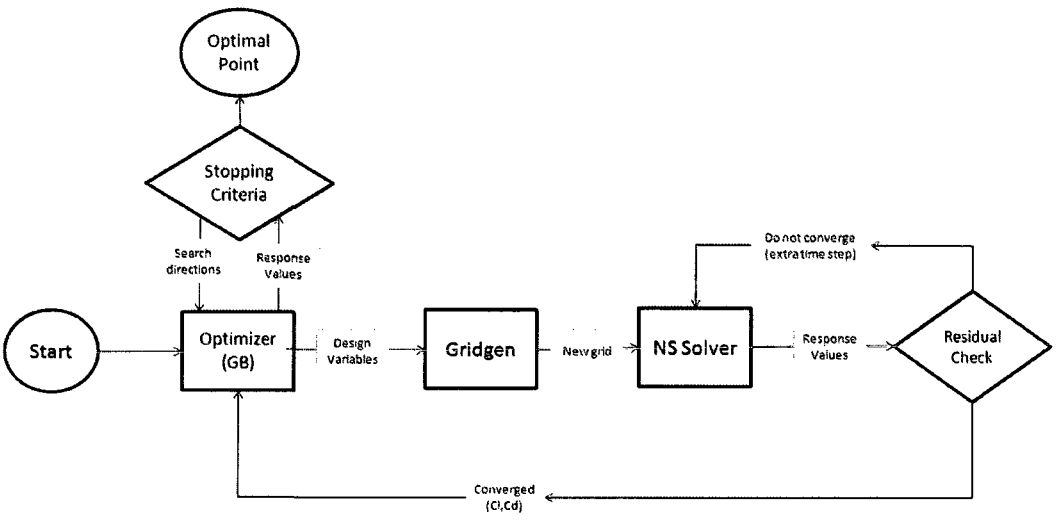

FIG. 27: The automated optimization process

V.2.3 Grid Generation

$2D$, *Rae*5243 airfoil was utilized. The computational grid was clustered in the normal direction and in the vicinity of jet and bump to resolve the details of the flow. The resolution of the utilized C-type computational grid was 337x129. Normal spacing for the first grid line of the surface of the airfoil was 0.00001c to ensure that the near wall y+ values of the airfoil blocks stayed in the appropriate range. Fig. 28 shows the grid clustering on the surface of the *Rae*5243 airfoil. The control devices stayed in a much refined region. The domain was decomposed into four blocks to make the computations parallel. The cases were run at Old Dominion University's teraflop computer cluster.

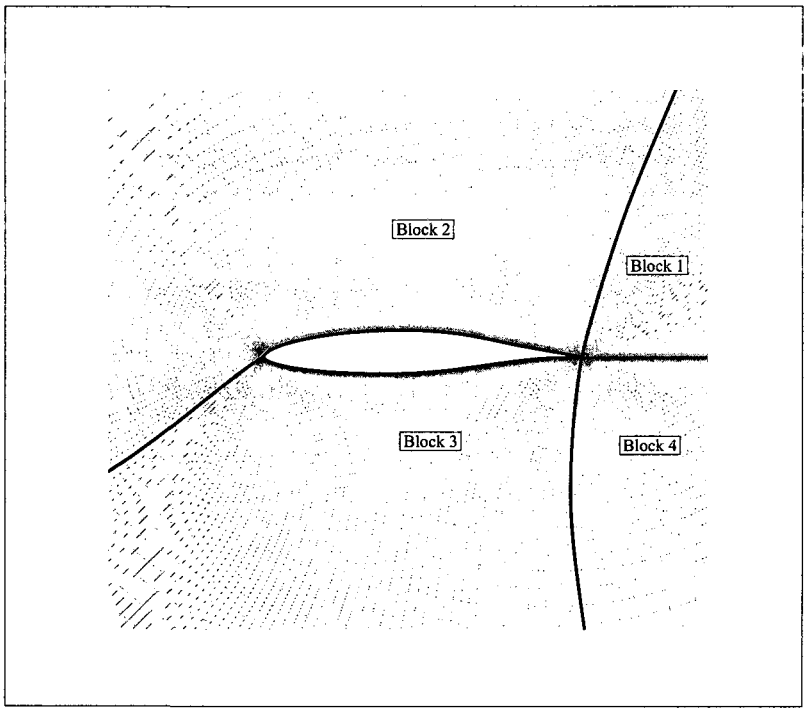

FIG. 28: The computational grid used in 2D simulation

V.2.4 Validation and Grid Sensitivity

The *Rae*5243 aerofoil was tested by Fulker and Simmons [56] at different transonic speeds with surface mass injection. The validation case used in this study has a

TABLE 9: *Rae*5243 aerofoil lift and drag coefficient without and with suction

	C_L	C_D
No Suction		
Experiment[56]	0.5154	0.00877
Computation[22]	0.5142	0.00980
Present	0.5299	0.01006
With Suction		
Experiment[56]	0.5146	0.00830
Computation[22]	0.5144	0.00968
Present	0.5361	0.01002

Reynolds number of 18.68x10^6 million based on aerofoil chord, $M_\infty = 0.6799$, $\alpha = 0.77^0$ corresponding to one of the wind tunnel experiments. The region of suction was located between $0.45c$ and $0.46c$ which is upstream of the shock position. The suction coefficient was 0.009 and the suction angle was 84^0 to the airfoil surface. Fig. 29 shows the comparison of the pressure distributions for both computation and experiment with and without flow control. In the numerical tests, three sets of grids have been used to demonstrate solution sensitivity . $y+$ values, based on the height of the first wall-bounded cell, are below unity for all the meshes considered here. The solutions obtained on the course and fine grids are reasonably good. The results obtained on these three different grid sizes are reasonably grid-converged results and prove the little solution sensitivity. The results are seen to be in qualitative agreement with the experiment. The measured lift and drag values for the validation cases can be seen in Table 9.

V.2.5 Bump-optimization study

$2D$ contour bump has been optimized for drag reduction at transonic speed using the gradient based optimization. The length, l_B, maximum height, h_B and the crest position relative to bump and airfoil,c_B, x_B, depicted in Fig. 30 are chosen as the key parameters. For the initial points as given in Table 10, asymmetric bump is used with a relative height of 1.2% chord consisting of the arcs located between $x = 0.5c$ and $0.99c$ with the junction of the arcs at $x = 0.9c$ on the *Rae*5243 airfoil section.

The lift coefficient is constrained to the no control value, $C_L = 0.5299$ during the optimization process. The objective is to minimize the total drag coefficient. The

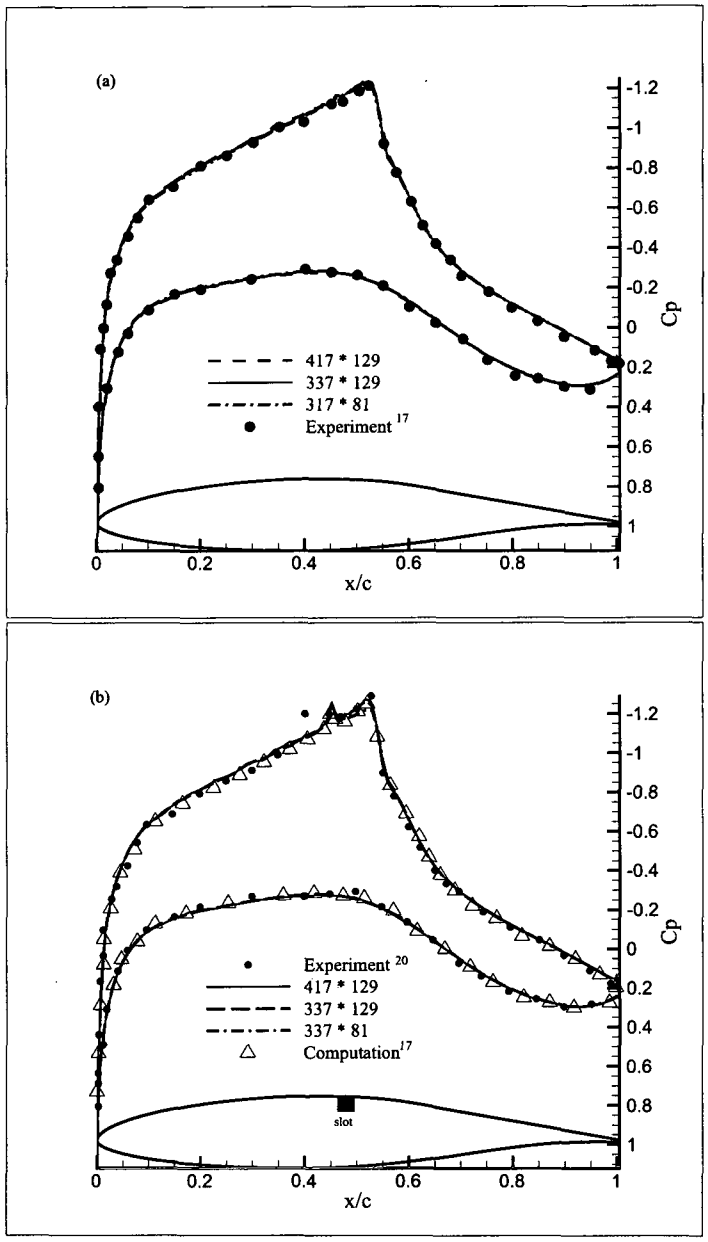

FIG. 29: Cp distributions over *Rae*5243 airfoil (a) without control and (b)with FC

optimization problem is defined in the following form:

$$MinC_D(x_B, l_B, c_B/l_B, h_B)$$

Subject to :

$$\begin{aligned} C_L &\geq C_{L0} \\ 0.0 \leq\ & x_B \leq 0.99c \\ 0.0 \leq\ & l_B \leq 0.75c \\ 0.01 \leq\ & c_B/l_B \leq 0.99 \\ 0.001c \leq\ & h_B \leq 0.02c \end{aligned} \tag{32}$$

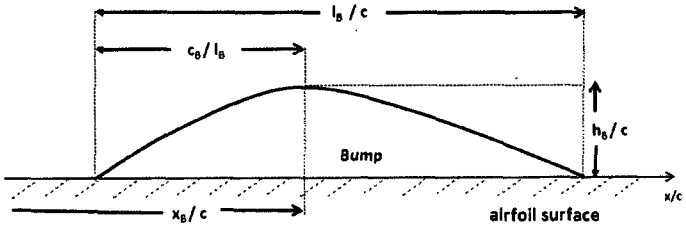

FIG. 30: Bump Picture

The bump becomes symmetric after 26 optimization iterations. Its crest point arrived close to the shock location, and its height is kept constant during the optimization process. Fig. 31 shows shapes of the airfoil and the change of the normalized lift and drag values with respect to the crest position of the bump during the optimization steps is also depicted on the right side.

The no control datum airfoil and the airfoil with control by an optimized bump is illustrated in Fig. 32. On the other hand, the pressure distributions belong to the original and optimized flow conditions are depicted in Fig. 32. The results of computations have been shown, and also they can be seen in Figs. 32 and 33, if the bump in the shock region is located correctly respect to the shock, the wave drag is reduced by weakening the shock strength with slightly increasing viscous drag. The wave drag is decreased as -3.12%, the skin friction is increased 0.72% placing the bump with optimum parameters as given in Table 10. The reduction of the wave

TABLE 10: Initial and optimal parameters

	Initial Parameters			
	x_B	l_B	c_B/l_B	h_B
1	0.82	0.40	0.80	0.012
	Optimal Results			
	${x_B}^*$	${l_B}^*$	${c_B/l_B}^*$	${h_B}^*$
	0.6377	0.3737	0.5043	0.01232
			C_L^*	C_D^*
			0.5328	0.009959
			+ %0.5473	−%0.9843

drag and the shock strength infers satisfying improvement for fuel consumption and aircraft range. The overall aerodynamic performance, lift-to-drag ratios is increased 1.55%. Special consideration is given to the development of the BL thickness by using $2D$ contour bump. As shown in Fig. 32 The BL thickness can be considerably reduced overall the airfoil except the location between the start and crest of the bump.

V.2.6 Discrete Suction-optimization study

As in the case of $2D$ contour bump, the effect of discrete suction on drag has been investigated. The flow control parameters such as mass flow coefficient, C_q, location of actuator, x_c, and suction/blowing angle relative to the local surface tangent, β are optimized to get the minimum drag. the width of the actuator, w_d is kept fixed as 0.0035 during the optimization. The angle is defined as the angle between the jet flow direction and the local aerofoil surface tangent. The effects of these parameters are analyzed by the authors of this paper in 2009 [57]. Fig. 34 shows the parameters of the control jet.

The optimization problem is defined in the following form:

$$MinC_D(C_q, \beta, x_c)$$

Subject to :

$$C_L \geq C_{L0}$$
$$-0.5 \leq C_q \leq 0.05$$
$$3^0 \leq \beta \leq 176^0$$

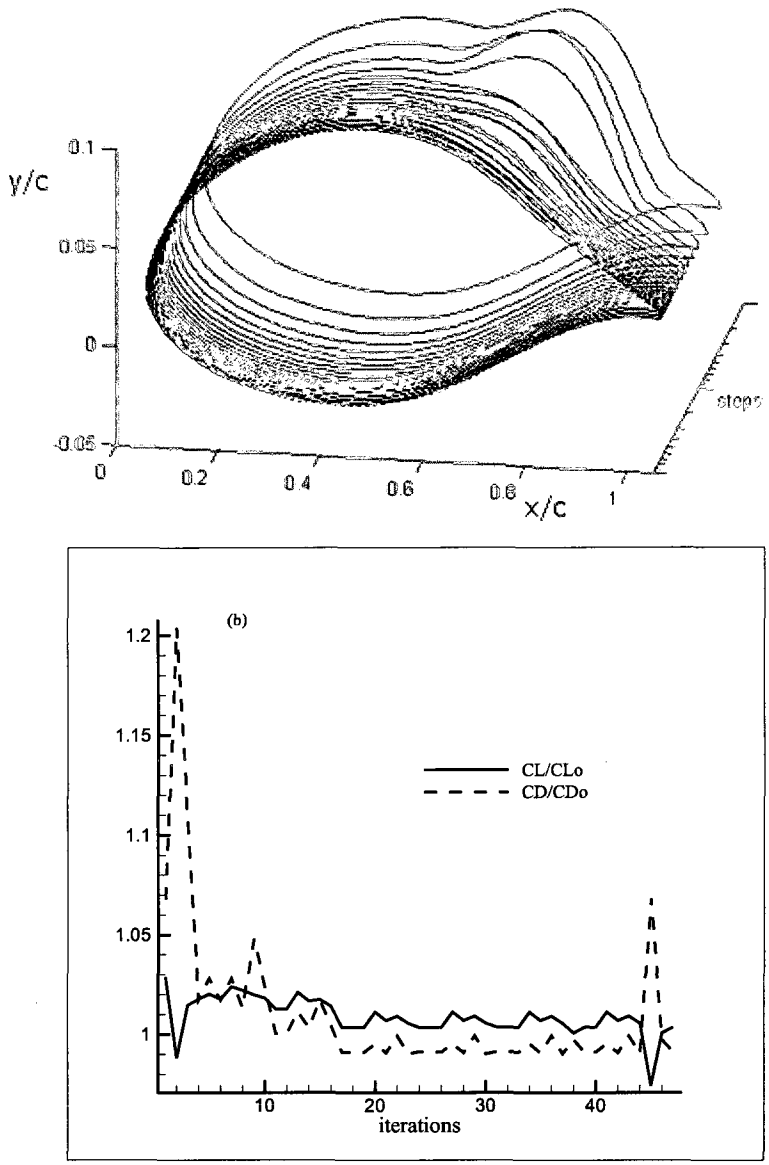

FIG. 31: Variation of (a)bump Design and (b)normalized C_L,C_D during the bump control optimization process

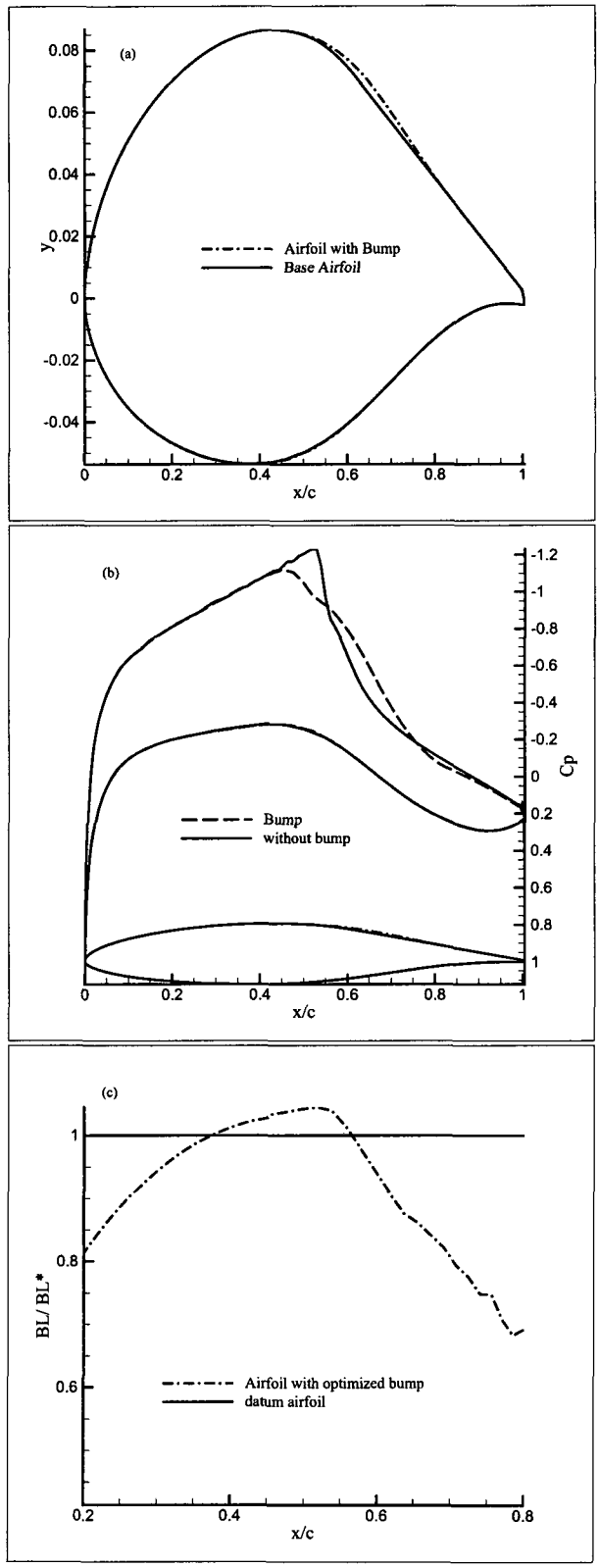

FIG. 32: Bump Optimization Study Results (a)Comparison of airfoil shapes (b)Cp distributions (c)BL comparison

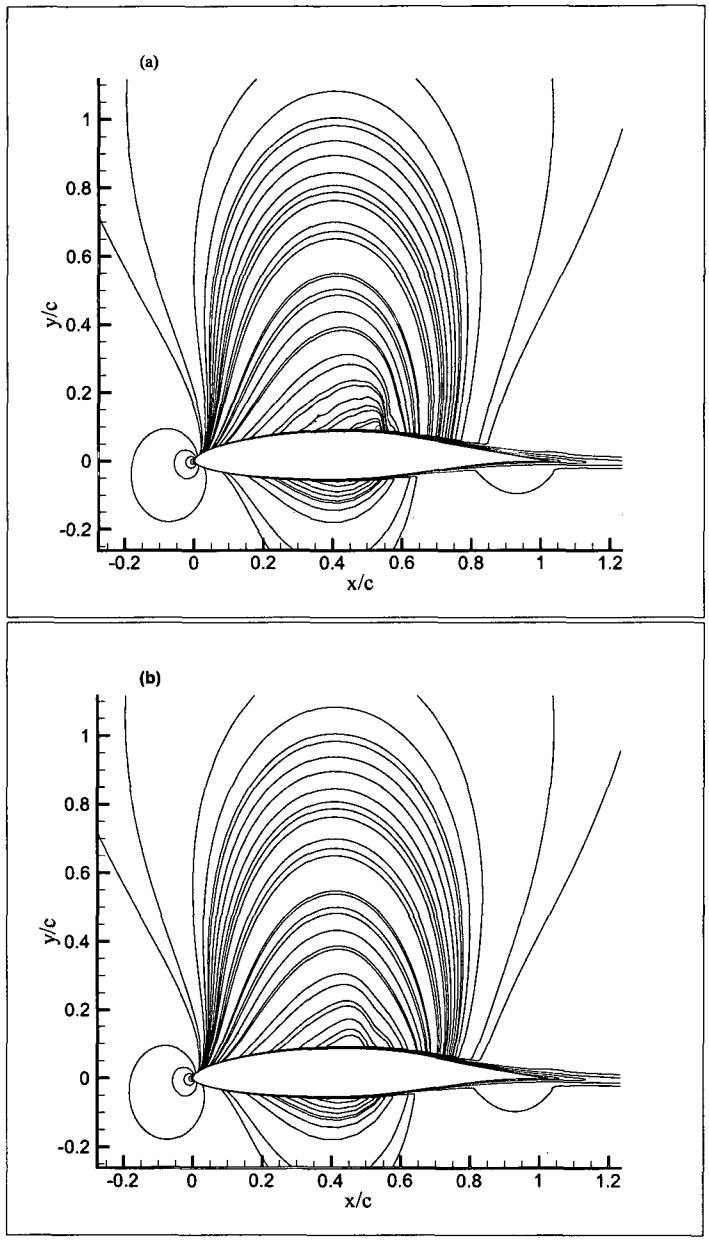

FIG. 33: Mach Contours (a)baseline and (b)with bump

$$0.01c \leq x_c \leq 0.99c \tag{33}$$

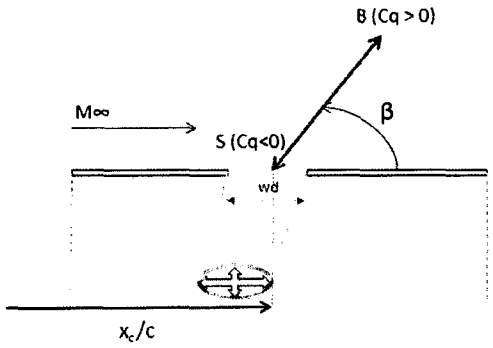

FIG. 34: Actuator Parameters

From the previous studies[57], it is known that to decrease the total drag, the actuator should be located upstream of the shock. At the initial point, the actuator is doing mass injection; after 9 optimization steps it turns to suction. The variation of C_q, C_L and C_D values during the optimization process are depicted in Fig. 35. C_L and C_D values are normalized with baseline C_{Lo} and C_{Do} values respectively. At the end of the optimization process, C_q has taken the suction velocity as -0.0755, β became close to the airfoil surface as 5.87^0, and the actuator is located upstream of the transonic shock wave, $x_c/c = 0.3944$. The resulting optimal values provide 3.17% increase in lift and 3.13% reduction in total drag. The drag is the sum of pressure drag, obtained by integrating the pressure and the skin friction distributions, respectively, along the airfoil surface [53]. The total drag decrement comes from the pressure drag rather than viscous drag. Although the skin friction is increased as 8.37%, the wave drag is reduced to 17.62% by mass removing. The increment in viscous drag depends on the angle of the suction relative to the surface. If the suction angle is almost tangent to the surface of the airfoil, the viscous drag is inevitably increased. It was shown before by Bedri et al. [57], by doing suction at an angle $3^0 - 7^0$ respect to the airfoil surface keeps or increases the lift value. The optimization results are given in Table 11. The overall aerodynamic performance of lift-to-drag ratios is increased by 6.5%.

Fig. 36 indicates the comparison of the pressure distributions and the boundary layer thickness normalized by the baseline BL thickness for the cases without flow

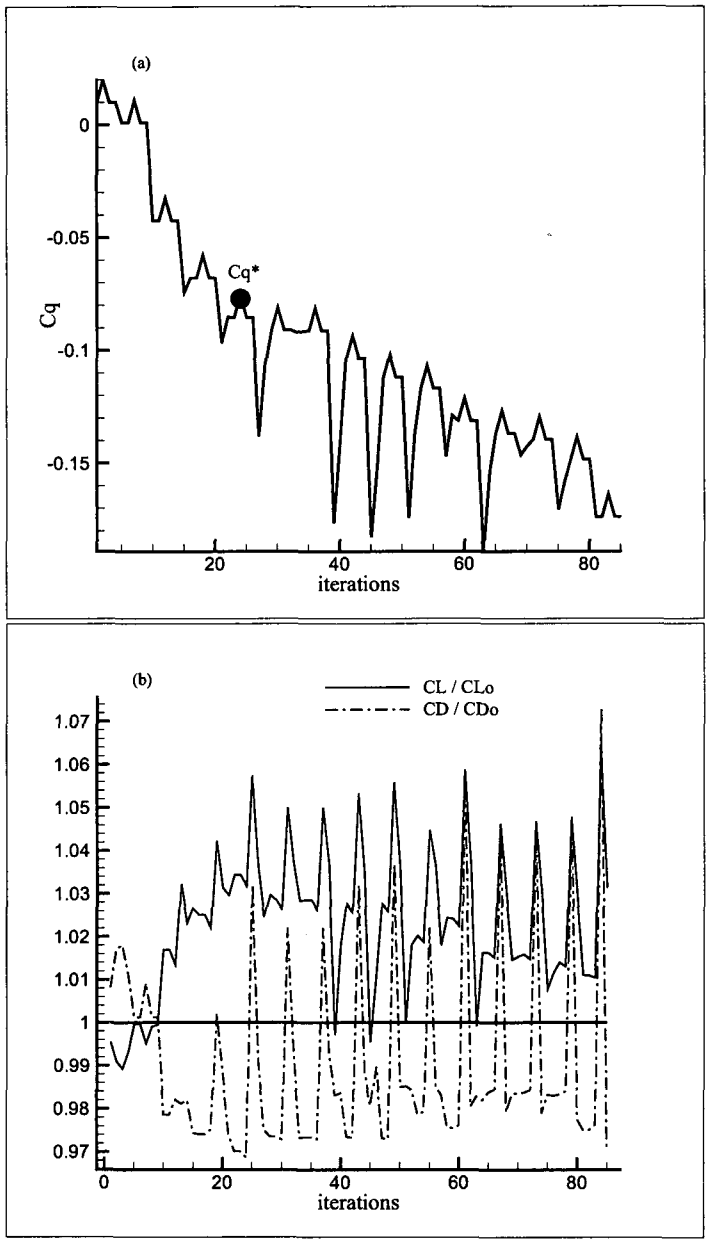

FIG. 35: The variation of (a)C_q and (b)normalized C_L,C_D values during the optimization process

TABLE 11: Initial and optimal values

	Initial Parameters		
	C_q	β	x_c/c
1	0.01	6.34^0	0.40
	Optimal Results		
	C_q^*	β^*	x_c/c^*
	-0.0755	5.87^0	0.3944
		C_L	C_D
		0.5467	0.00974
		+ %3.17	- %3.13

control and with optimized flow control. The effect of suction on the pressure distributions is reliant on the actuator location. The suction, located at $x/c = 0.3944$, slightly reduces the BL thickness upstream of the shock location, $x_c/c = 0.53$, after the shock the decrement is considerably increased. The actuator is located upstream of the shock, dependent on the suction rate, spreading the top of the shock into three small pieces. The separation can be seen from the mach contours given in Fig. 37. These small partitions cause reduction in pressure drag with increment in lift value.

V.2.7 Hybrid-optimization study

Hybrid control consists of the $2D$ contour bump and suction on the upper surface of the airfoil. In this optimization, three parameters are from discrete suction and four parameters are from bump. The optimization problem is defined in the following form:

$$MinC_D(C_q, \beta, x_c, x_b, l_B, c_B/l_B, h_B)$$

Subject to :

$$\begin{aligned} C_L &\geq C_{L0} \\ -0.5 \leq C_q &\leq 0.0 \\ 3^0 \leq \beta &\leq 176^0 \\ 0.01c \leq x_c &\leq 0.99c \\ 0.0 \leq x_B &\leq 0.99c \\ 0.0 \leq l_B &\leq 0.75c \end{aligned}$$

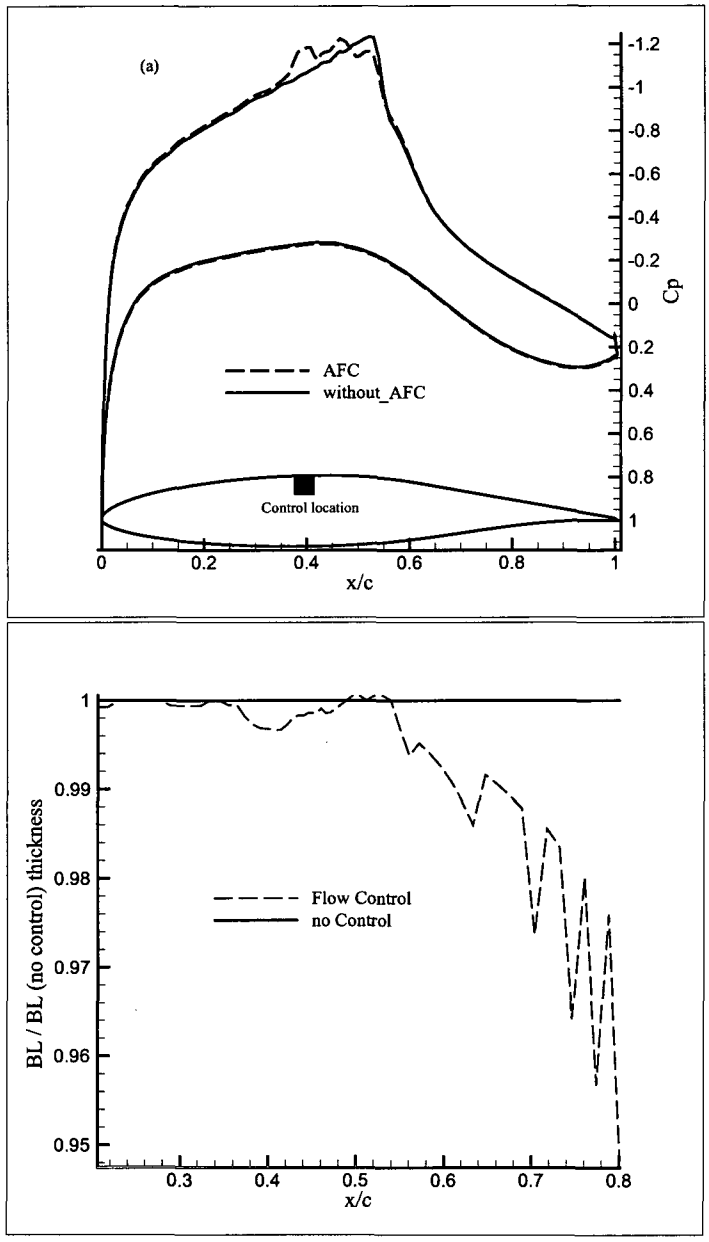

FIG. 36: Comparison of (a)Cp distributions and (b)normalized BL Thickness

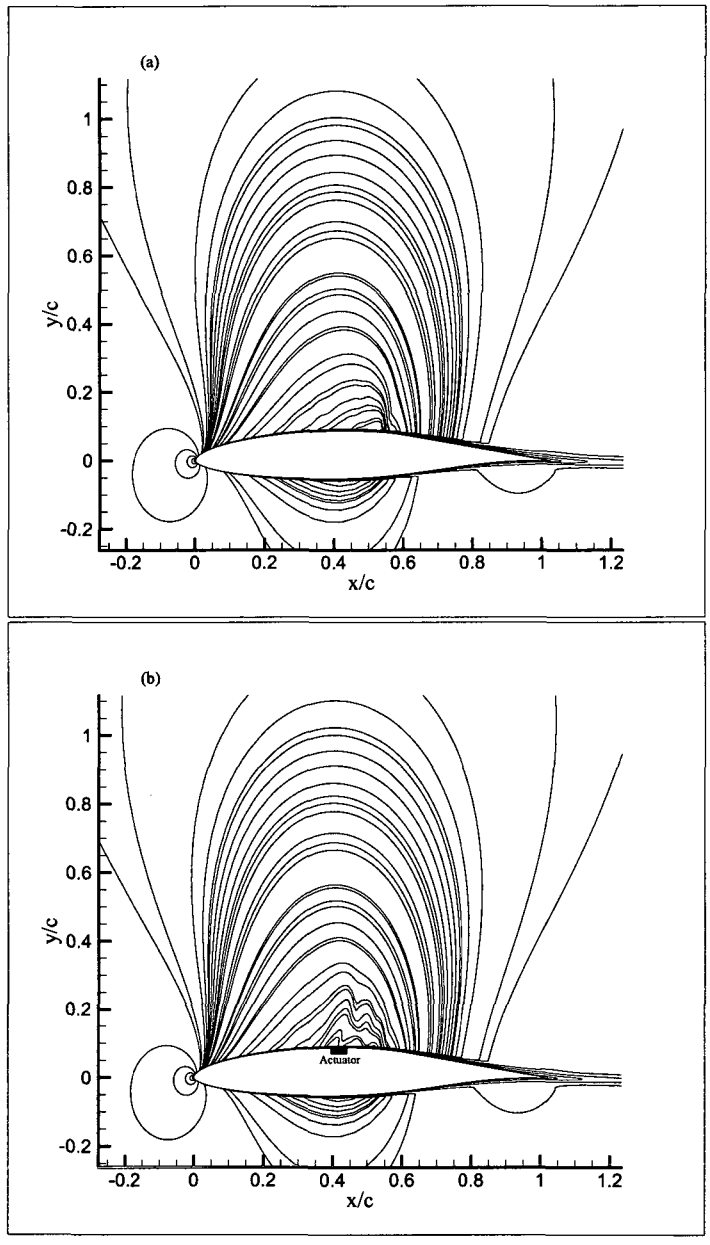

FIG. 37: Mach Contours (a)without FC and (b)with FC

$$0.0 \leq c_B/l_B \leq 1.0$$
$$0.01c \leq h_B \leq 0.02c \tag{34}$$

Nonetheless, these methods require calculation of a large number of flow solutions because there are more parameters than in the other cases. Many initial points were used to escape from the local optimums in this study. The initial points were chosen relative to the shock location. The bump crest was located in the vicinity of the shock and suction slot was located after this point to make easy the expansion. Fig. 38 shows the optimization steps to minimize the drag coefficients by optimizing the actuator and bump parameters. For hybrid cases, the variation of normalized C_L and C_D values via the optimization steps is depicted in Fig. 38.

The results of the computations of a contour bump in combination with downstream slot suction are illustrated in Fig. 39 by pressure distributions and boundary layer parameter. The boundary layer was only increased at the interaction region. As already seen in the previous sections, the surface suction with appropriate selection of C_q, β, x_c decreases the drag , 3.13% with an increment in lift value, 3.17% and the optimum bump alone results in a drag reductions of 0.9843% without any penalty in lift. The optimization of hybrid control raises the drag reduction to 3.94% and lift increment to 5.04%. The corresponding pressure distributions and boundary layer thickness in Fig. 39 show that the hybrid control reduces the wave drag, 32.58%, due to pushing and spreading the shock upstream with increasing viscous drag around 19.15%. As already mentioned in the discrete suction control study, the increment in viscous drag depends on the angle of the suction relative to the surface. As a result, the overall aerodynamic performance, lift-to-drag ratios is increased 9.34%.

V.2.8 Conclusion

The desired goal behind this optimization study is to reduce the drag of an airfoil in transonic conditions without any loss in lift. Some validation cases have been done with the experimental and numerical data regarding pressure distribution, lift and drag coefficients. A validation study guaranteed the prediction capabilities of the analyzer software. At the same time, a grid sensitivity study was performed to ensure the numerical solution accuracy of the governing equations. The computational results for the transonic airfoils investigated in this study show that the application of shock control in the form of $2D$ contour bump, discrete suction, and combination

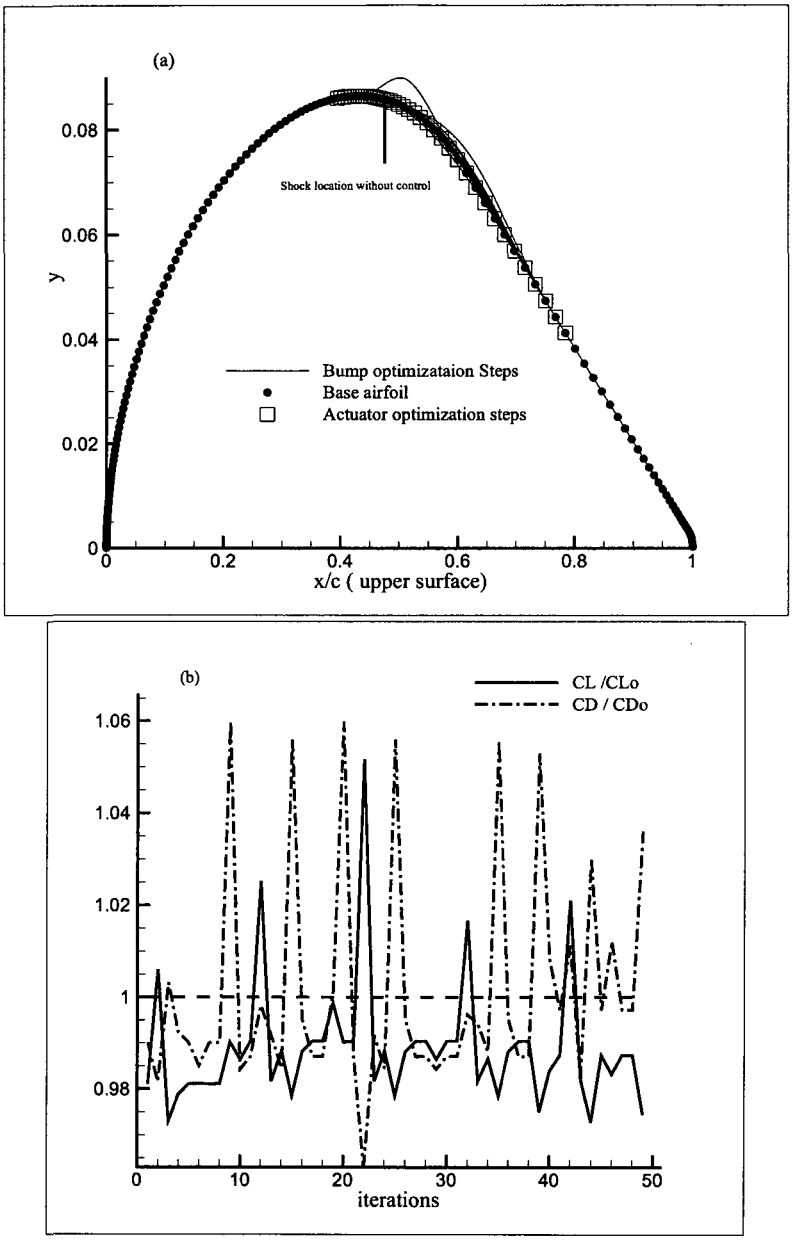

FIG. 38: Variation of (a) Design Variables and (b)Normalized C_L,C_D during hybrid control optimization process

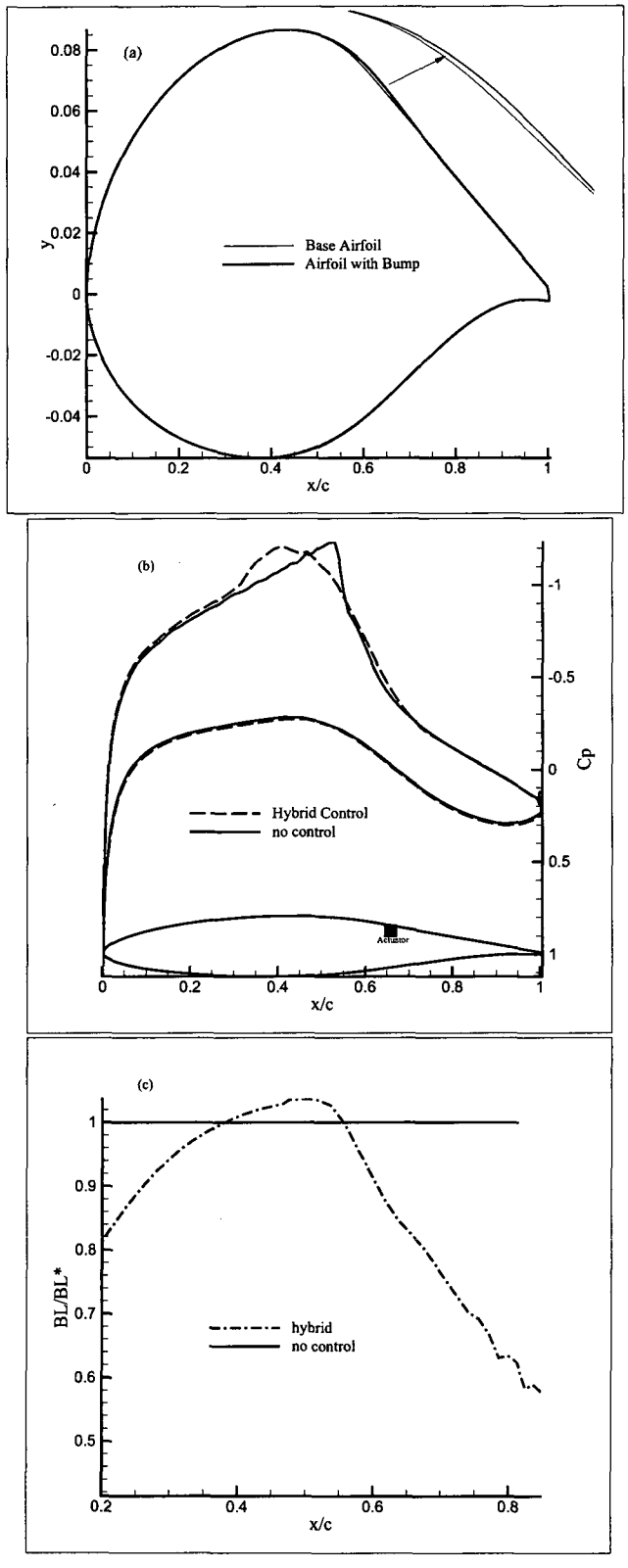

FIG. 39: Comparison of (a) Airfoil (b) Cp distributions and (c)BL thickness

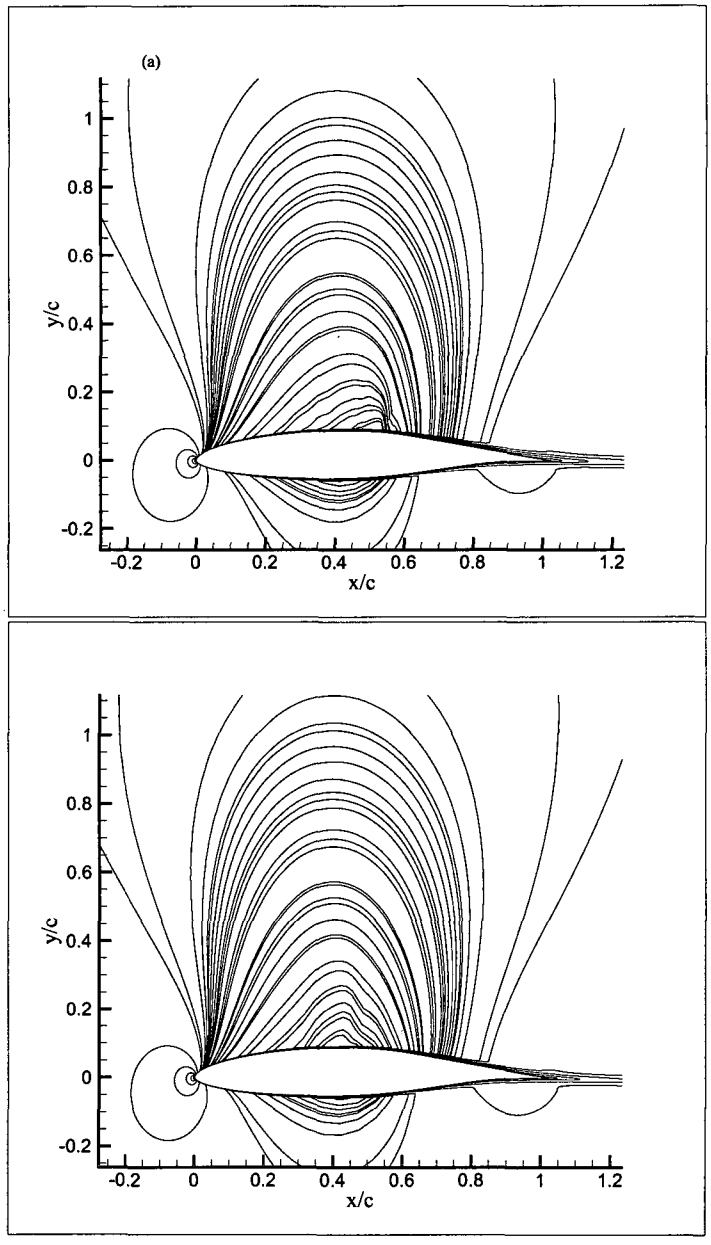

FIG. 40: Mach Contours (a)baseline and (b)with hybrid control

TABLE 12: Initial and optimal values

	Initial Parameters			
Actuator	C_q	β	x_c	
	-0.07	6.34^0	0.65	
Bump	x_b	l_B	c_B/l_B	h_B
	0.576	0.280	0.45	0.0099
	Optimal Parameters			
*Actuator**	C_q^*	β^*	${x_c}^*$	
	-0.0700	6.34^0	0.6651	
*Bump**	${x_b}^*$	${l_B}^*$	$c_B/{l_B}^*$	${h_B}^*$
	0.5862	0.2625	0.4617	0.009942
	Optimal Results			
		C_L^*	C_D^*	
		0.5566	0.009662	
		+%5.17	−%3.73	

of these two control techniques, called case hybrid control, importantly reduces total drag without any penalty in lift.

The computational studies for the transonic airfoils were first done with control by a $2D$ contour bump in the shock region. Bump optimization study achieved an augmentation in lift-to-drag ration around 1.55%. As mentioned earlier the objectives of flow control may cause conflict as the achievement of one desired goal may adversely affect another goal. By using bump, all desired goals were obtained without any penalty. The result indicates that the enhancement in lift and decrement in total drag and the mitigation in shock strength can be obtained by using 2d contour bump.

In the second part, the surface suction with appropriate selection of C_q, β, x_c decreases the drag with an increment in lift value. At the end of the optimization process the resulted optimal values provide 3.17% increase in lift and 3.13% reduction in total drag.

The author is cognizant of the fact that there are significant deficiencies with a combination of control mechanisms in transonic regime. The main difference; hence, the contribution of present study is performed at transonic speed via steady suction jet and $2D$ bump together. $2D$ contour bump and discrete suction actuator on the upper surface of airfoil were combined named hybrid control. The drag reduction is increased to 3.94% and the lift increment is raised to 5.04% by using the hybrid

control. Based on this study, detailed suggestions are provided to aid in the preparation of a possible future study on flow control techniques with optimization. "smart bump" could be one of them.

V.3 COMBINED OPTIMIZATION OF SHAPE AND FLOW CONTROL PARAMETERS ON AN AIRFOIL AT TRANSONIC SPEEDS

V.3.1 Introduction

Engineering design of an airplane wing roughly consists of three stages: conceptual design such as determining the span length, maximum thickness, taper ratio, sweep angle, and aspect ratio; preliminary design including airfoil shape and its optimization, and detailed design including the detailed plan for manufacturing of the wing. In a preliminary design phase, designers start with a good baseline design and then concentrate on improving its performance by using optimization techniques. For transonic commercial aircraft wing design, the primary goal is to improve the wing performance at the cruise conditions without severe penalty at off-design conditions. The main issue at this stage is a shock wave reduction problem. A wave drag is caused by the formation of shock waves around the wing. Shock waves radiate away a considerable amount of energy that is experienced by the aircraft as drag. The magnitude of the rise in drag is impressive, typically peaking at about four times the normal subsonic drag. As this consumes energy, it is highly beneficial to eliminate the effects of shock wave at the design phase.

Optimization is a key tool to reduce the effects of shock wave and it is heavily based on the reforming of an airfoil shape in a passive way. Since the 1970s, the use of numerical optimization techniques in airfoil and wing geometry design has received considerable attention. Both gradient based[58, 59] and non-gradient based algorithms[60, 61] have been employed as a numerical optimization tool for airfoil shape design. In addition to PFC based on aerodynamic shape optimization techniques, AFC can also provide a high aerodynamic performance enhancement by optimizing its parameters. However, AFC alone may not be sufficient to get the best designs. Therefore, it is recommended to study simultaneous AFC and PFC techniques.

The desired goal of the present study is to improve the aerodynamic performance on an airfoil at transonic speed by optimizing the airfoil shape and/or surface suction/blowing parameters. For this reason, four different optimization cases were studied. They are as follows:

- Case I: the optimization of AFC parameters on *NACA-64A010* airfoil,

- Case II: the optimization of shape control parameters starting with *NACA-64A010* baseline airfoil,
- Case III: the simultaneous optimization of active flow and shape control parameters starting with *NACA-64A010* baseline airfoil,
- Case IV: the sequential optimization of active flow and shape control parameters starting with NACA 64A010 baseline airfoil.

For these applications, real coded genetic algorithm is used to search for the optimal design. For the flow simulations, a time-dependent, turbulent flow solver is used on structured grids. Present computations were performed for Re_c 6.07 million, $M_\infty = 0.85$ flow past airfoil at $\alpha = 1^0$.

V.3.2 Numerical Model for Optimization Process

A non-gradient based optimization method, vibrational genetic algorithm enhanced with neural networks which is a real coded genetic algorithm[44] was used in this study. Within the algorithm an initial population is generated by using a random number operator based on baseline shape or parameters. The details of the algorithm is written in optimization techniques chapter.

The algorithm repeats all of the above steps as is necessary until the convergence criterion are satisfied. The settings for the optimizations are given in Table 13. The block diagram for the optimization process is shown in Fig. 41.

TABLE 13: The features of GA

S/N/I	$f_i - w_i - \beta_i$
10/40/3	$f_1 - w_1 - \beta_1 4/0.5/1$
	$f_2 - w_2 - \beta_2 1/0.5/1$

V.3.3 Design parameters and objective function description

In optimization processes there are two types of design parameters; shape parameters for airfoil forming, and flow control parameters for AFC. An airfoil can be represented using Bezier curves with a set of control points[62]. Two-dimensional Bezier curves are given by the following equations:

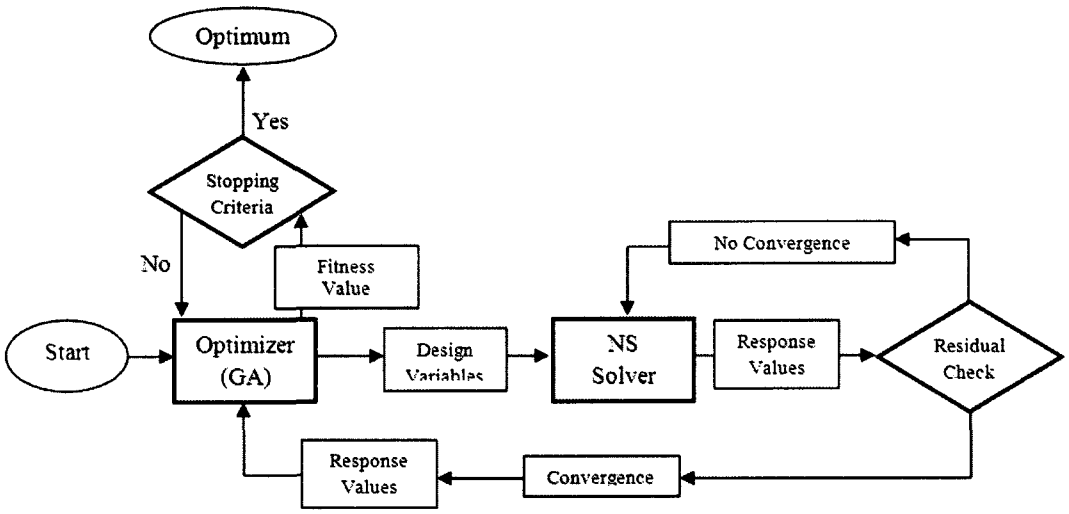

FIG. 41: Optimization process

$$z_1(s) = \sum_{i=0}^{m} C_m^i s^i (1-s)^{m-i} z_{1,i}, \quad {}^{i=1,2,\ldots,D-1} \tag{35}$$

$$z_2(s) = \sum_{i=0}^{m} C_m^i s^i (1-s)^{m-i} z_{2,i}, \quad {}^{i=1,2,\ldots,D-1} \tag{36}$$

$$C_m^i = \frac{m!}{i!(m-i)!}, \quad {}^{i=1,2,\ldots,D-1}, m = D-1 \tag{37}$$

where s is a member of a set whose values vary uniformly between [0,1]. $z_{1,i}$ and $z_{2,i}$ are the coordinates of the control points which define the profile coordinates, $z_1(s)$ and $z_2(s)$. The two control points (0,0) and (1,0) at the leading and trailing edges are fixed. It is commonly assumed that the $z_{1,i}$ control points are fixed therefore the design parameters for forming are only the $z_{2,i}$ control points. The initial population needed for the present method is generated by using a random number operator. The number of control points is taken as 10 for upper and lower airfoil surfaces.

The following design parameters are used to parameterize the flow control: mass flow coefficient, C_q, center location of actuator, x_c, and suction/blowing angle relative to the local tangent, β. In studied cases only one actuator is used on the upper surface

and the width of the actuator, w_d, is fixed to $0.035c$. The design parameter bounds are described as follows:

$$\begin{gathered} \mathbf{Y}^{afc} = [C_q \ \beta \ x_c]^T \\ -0.2 \leq C_q \leq 0.025 \\ 3^0 \leq \beta \leq 176^0 \\ 0.10c \leq x_c \leq 0.96c \end{gathered} \tag{38}$$

Both parameter groups are depicted in Figs. 42, and 43.

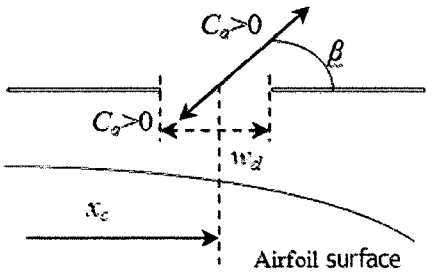

FIG. 42: Active flow control parameters

In shape optimization related problems, the objective function, f is to be maximized, where

$$f = [\frac{C_D}{C_L} + 10(C_L^* - C_{L2})^2 + 100(t^* - t)^2]^{-1} \tag{39}$$

$$C_{L2} = \left\{ \begin{array}{ll} C_L^*, & \text{if} \quad C_L \geq C_L^* \\ C_L, & \text{if} \quad C_L < C_L^* \end{array} \right\}$$

C_L^* is the design lift coefficient and t^* is design maximum thickness ratio, which are taken for the demonstration case to be 0.13 and 0.1, respectively. In the AFC problem, there is no need for the thickness constraint. Therefore, the objective function, f is to be maximized, where

$$f = [\frac{C_D}{C_L} + 10(C_L^* - C_{L2})^2 \tag{40}$$

$$C_{L2} = \left\{ \begin{array}{ll} C_L^*, & \text{if} \quad C_L \geq C_L^* \\ C_L, & \text{if} \quad C_L < C_L^* \end{array} \right\}$$

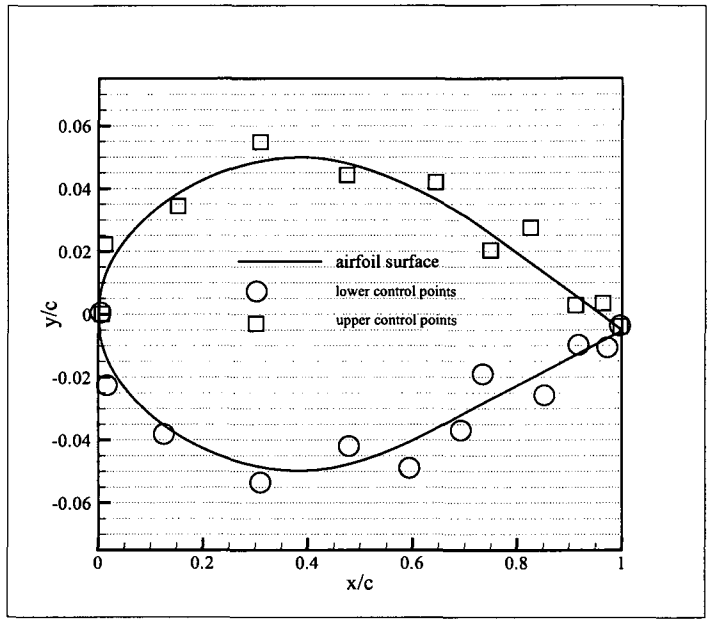

FIG. 43: Shape parameters

V.3.4 Grid generation, validation, and sensitivity

Two dimensional, 10% thick symmetric $NACA-64A010$ was used as the test airfoil. The travel area of the actuator locations between $0.01c$ and $0.99c$ is made dense. The resolution of the utilized C-type computational grid is 449x121. Normal spacing for the first grid line of the surface of the airfoil was $0.00001c$. In the normal direction, 121 grid points were utilized with the farfield boundary located at a distance equal to 13 airfoil chord lengths. Shown in Fig.44 are the grids used in the simulations. To demonstrate the effectiveness of the present method, a solution for the airfoil without actuator was carried out. The validation case used in this study had a Reynolds number of 6.07 million based on airfoil chord $M_\infty = 0.85, \alpha = 1.0^0$ corresponding to one of the numerical study [46]. For the above free stream conditions, the predicted sectional lift and drag are equal to 0.13 and 0.0329 respectively. The predicted components of airfoil drag are: 0.27338 representing the pressure component (C_{WD}) corresponding to 83% of the total drag and 0.00554 representing the skin friction component (CFD) corresponding to 17% of the total drag. Solution sensitivity to

the grid used in this study is illustrated in Table 14. For the computational cases, three sets of grids and another computational result given by Hassan at al.[63] have been used. The solutions obtained on the course and fine grids are reasonably good. The results obtained on these three different grid sizes are reasonably grid-converged results and prove little solution sensitivity.

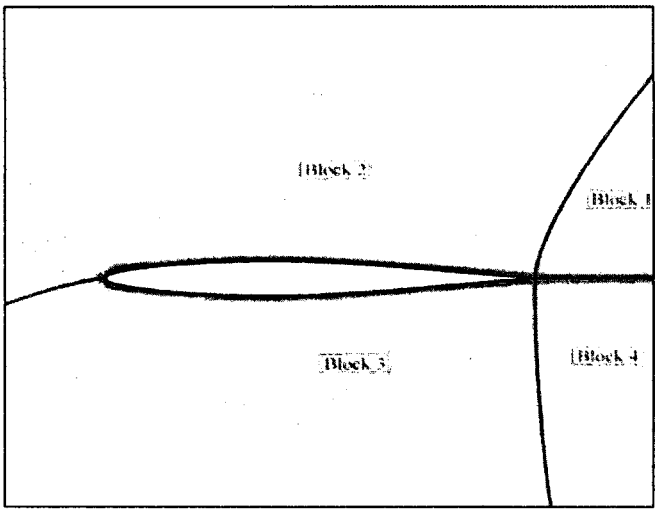

FIG. 44: Computational grid used in simulations

TABLE 14: Grid sensitivity for *NACA-64A010* aerofoil test cases

Grid Size	C_L	C_D	C_{FD}	C_{WD}
Without control				
$449 * 121$	0.1300	0.03290	0.005540	0.027338
$389 * 121$	0.1357	0.03233	0.005440	0.026889
$281 * 99$	0.1298	0.03261	0.005452	0.027158
Computation[?]	0.1400	0.03280	0.00544	0.027400

V.3.5 Optimization Results

Optimization of flow control parameters

At first, only AFC parameters are optimized to get a maximum aerodynamic performance. The genetic optimization process takes only eleven generations. At the end of the optimization process, C_q has taken the suction velocity as -0.1884, β became

the minimum angle as 3^0 which is tangent to airfoil surface, and the location arrived at $0.8295c$ which is very close to the shock wave location located at $0.830c$. The convergence histories of the aerodynamic coefficients, C_L, C_D, and the aerodynamic performance, C_L/C_D, are depicted in Fig. 45. After suction operation at optimal values and optimal location, C_L is increased to 0.3545 which means a 272.6% increment compared with the original lift coefficient; on the other hand, C_D is also increased to 0.04251 which means a 29.17% increment compared with the original drag coefficient. However, the total drag increment comes from the wave drag rather than the form drag. For example, velocity profiles inside the boundary layers are depicted in Fig. 46. In the suction case the thickness of the boundary layer became thinner due to suction operations. As a result, the aerodynamic performance is increased to 8.339 which means 211.1% increment when compared with the original value which is equal to 3.95.

On the other hand, the C_p distributions and Mach counters around the airfoils are depicted in Figures 47,48, and 49. According to these figures, suction operation has a significant effect on the positions of both upper and lower shocks. The locations of shock waves are significantly changed. The upper shock wave moved from $0.695c$ to a new location at $0.830c$. This relocation causes an extension of the supersonic region and also an additional strength to the upper shock wave. The position of the lower shock wave is a bit different. Instead of moving forward, it is moved backward toward $0.600c$. Additionally, the strength of lower shock wave is also decreased. The movement of upper shock toward the downstream extends the supersonic region resulting in better aerodynamic performance.

Optimization of shape control parameters

In the second case, only the shape control parameters are optimized to get a maximum aerodynamic performance. The genetic optimization process takes forty generations. The convergence histories of the aerodynamic coefficients, C_L, C_D, and the aerodynamic performance, C_L/C_D, are depicted in Fig. 50. After forming at optimal values, C_L is increased to 0.2496 which means a 192% increment when compared with the original lift coefficient; C_D is decreased to 0.01213 which means a 63.13% decrement when compared with the original drag coefficient. The total drag decrement comes from the wave drag rather than the form drag. At the end, CFD takes the value of 0.0060 and C_{WD} takes the value of 0.0059 which is less than form drag. As a result,

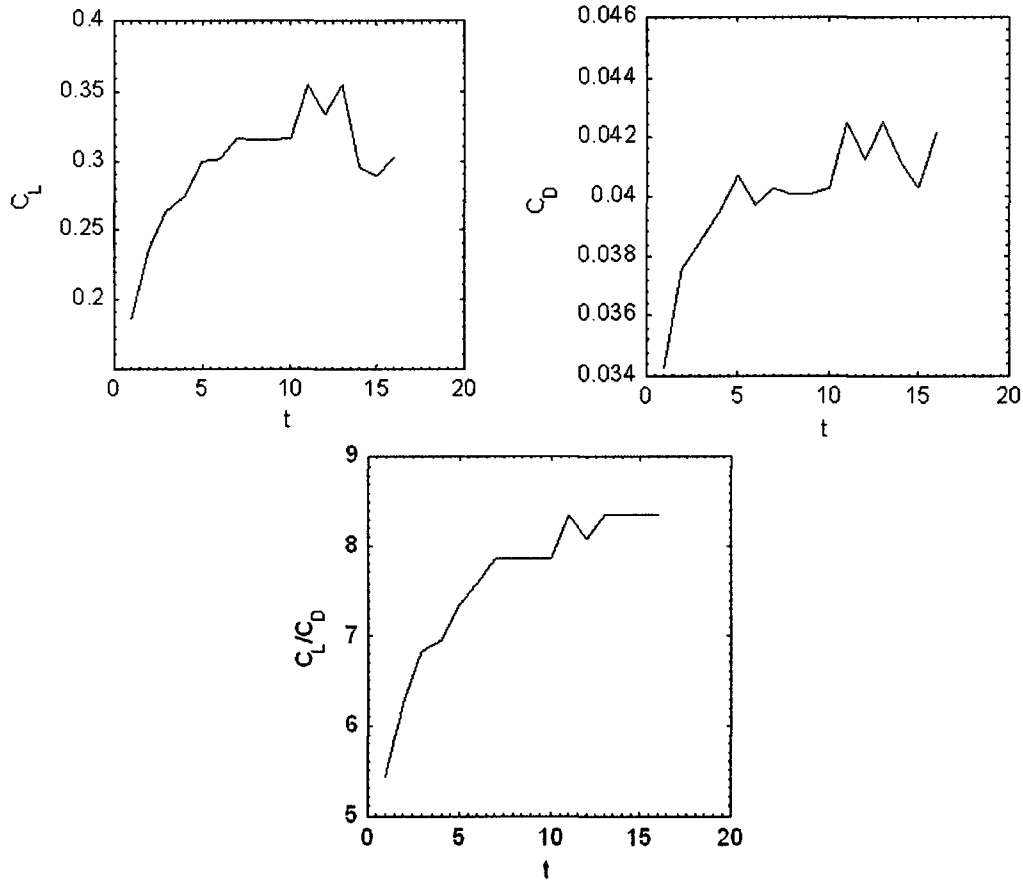

FIG. 45: The change of aerodynamic coefficients and performance during the generations

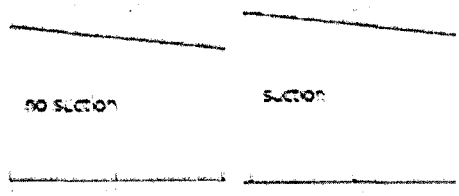

FIG. 46: Velocity profiles inside the boundary layers

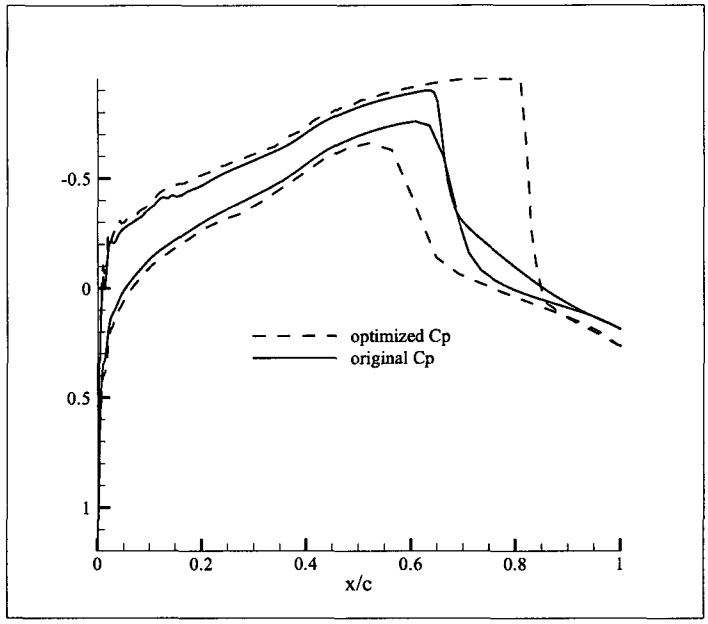

FIG. 47: C_p distributions around *NACA-64A010*

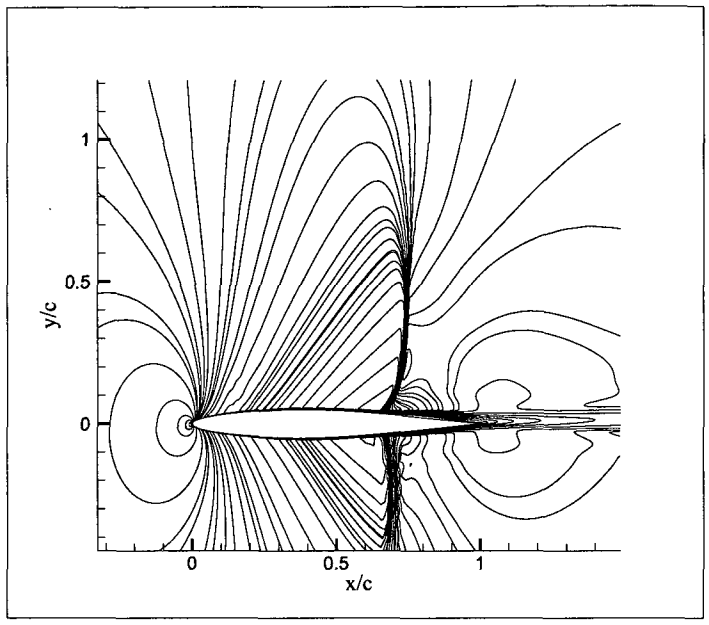

FIG. 48: Mach counters around *NACA-64A010* without AFC

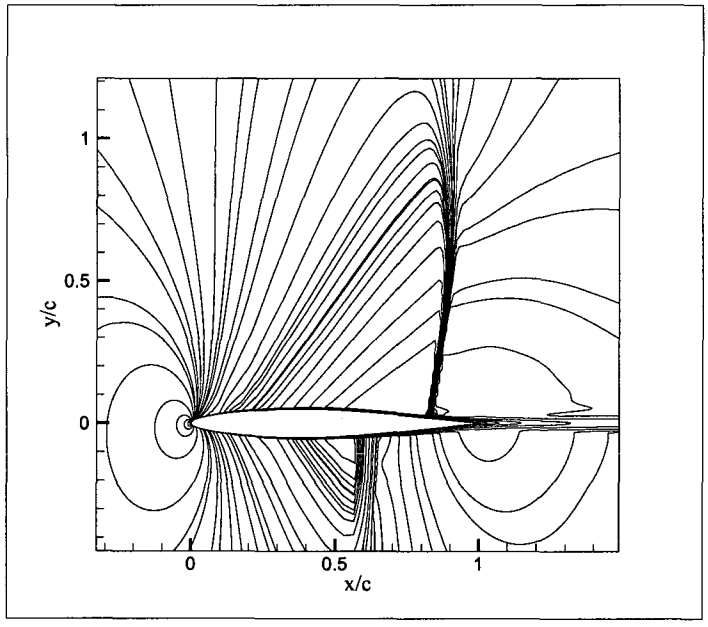

FIG. 49: Mach counters around *NACA-64A010* with AFC

the objective function is increased to 20.58 which means 520.75% increment when compared with the original aerodynamic performance.

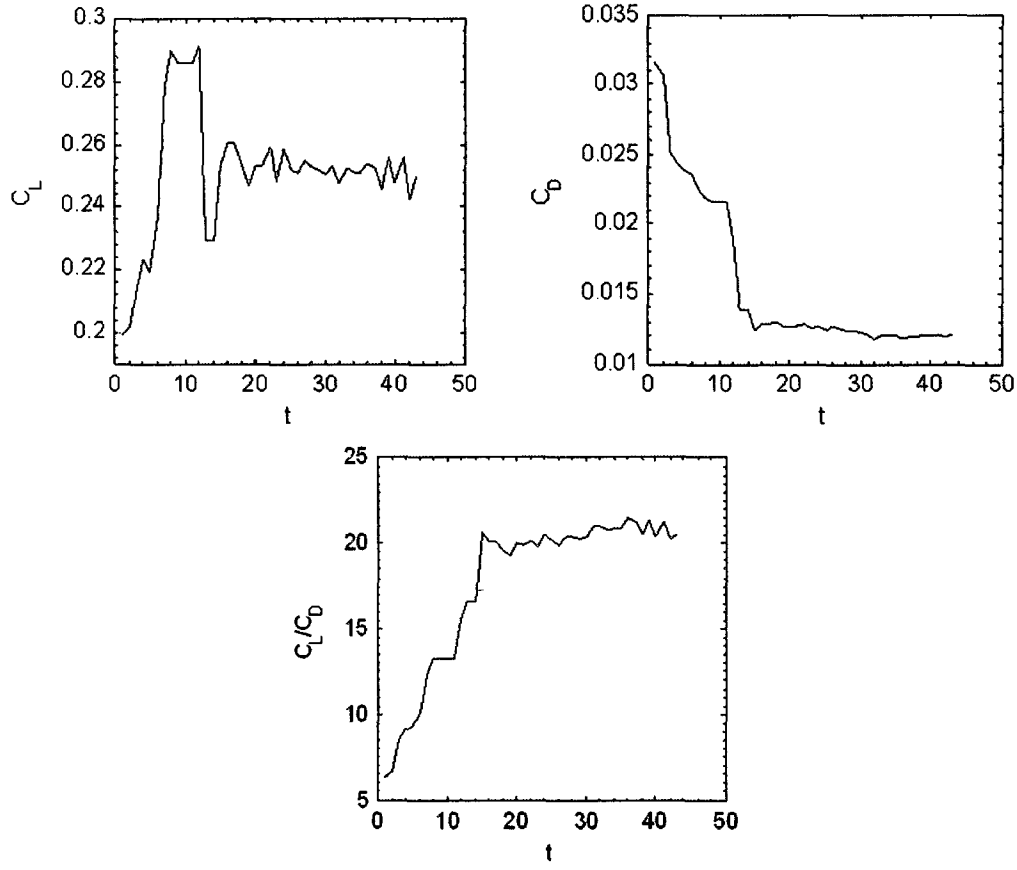

FIG. 50: The change of aerodynamic coefficients and performance during the generations

The resulting C_p distribution and Mach counter around the optimized airfoil are shown in Figs. 51, and 52. The maximum thickness ratio for the optimal airfoil form is about 0.0963 which is good enough for the process. During the optimization, the crescent point for the upper surface moved toward the trailing edge as is expected. This movement results in the relocation of the shock waves. The upper shock wave moved from the original place at $0.695c$ to $0.782c$. The lower shock wave is also moved toward the leading edge. Both the strengths of the shock waves are significantly decreased. However, there are still shock waves although they are weak. The main

reason for the shock waves is the high free stream Mach number which is equal to M_∞ 0.85. Practically, it is difficult to entirely eliminate the shock wave on the upper surface by using shape formation in high transonic flows.

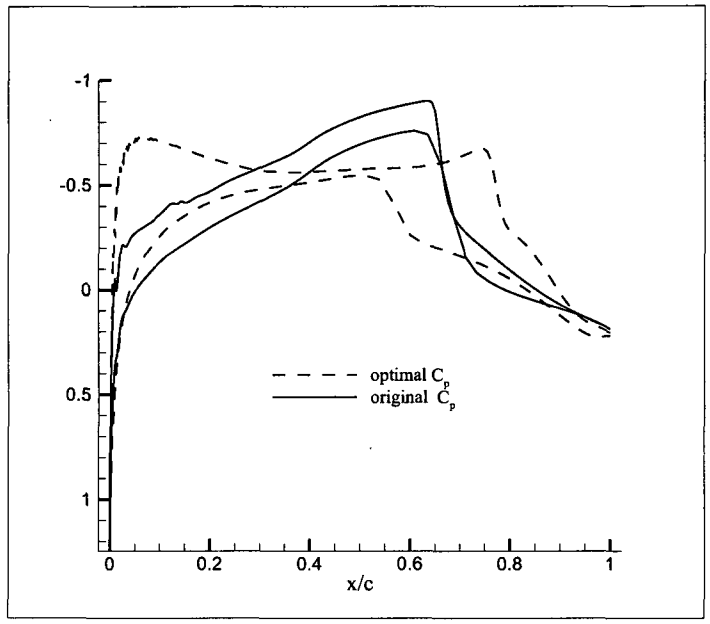

FIG. 51: C_p distributions around *NACA-64A010* and optimized airfoil

Combined optimization of shape and flow control parameters

In the third case, the shape and the flow control parameters are simultaneously optimized to get a maximum aerodynamic performance. The genetic optimization process takes about thirty-eight generations. The convergence histories of the aerodynamic coefficients, C_L, C_D, and the aerodynamic performance, C_L/C_D, are depicted in Fig. 53. After the optimization process, C_L is increased to 0.3193 which means a 245.61% increment when compared with the original lift coefficient; on the other hand, C_D is decreased to 0.0162 which means a 50.75% decrement when compared with the original drag coefficient. As a result, the objective function is increased to 19.71 which means a 498.8% increment when compared with the original aerodynamic performance.

The resulting C_p distribution and Mach counters are shown in Figs. 54and 55. The maximum thickness ratio for the optimal airfoil form is about 0.0881, and this

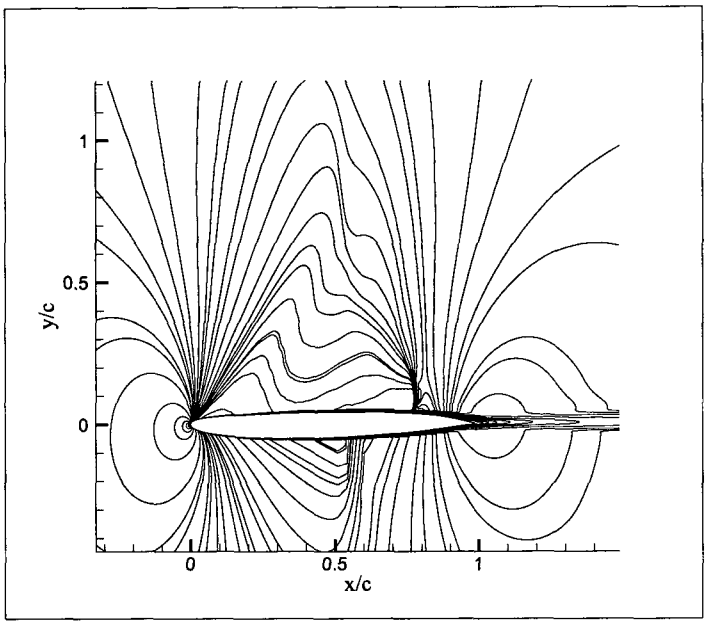

FIG. 52: Mach counters around optimized airfoil shape

result is not good enough for the process. The optimization process could not preserve the desired thickness ratio. In the objective function description given in Eq. 39 the weighting number for thickness constraint is 100, and it is good enough for this kind of problem. Because of the improper resulting shape, the second optimization process was run. In this second application the weighting number for the maximum thickness ratio is increased from 100 to 200. However, the resulted airfoil shape has 0.091 maximum thickness ratio, and again it doesn't satisfy the required thickness ratio. From both results we understand that the main reason for the deficient thickness ratio is the AFC operations. In this optimization process, the increase in C_L originated from AFC dominates the thickness ratio constraint. It seems that AFC gives an extra thickness ratio to the airfoil shape in objective function computations. On the other hand, bigger weight number may result in insufficient design optimization space and it does not allow robust designs. Similar to the shape optimization process, the crescent point for the upper surface moved toward the trailing edge. The upper shock wave moved from original place $0.695c$ to $0.825c$. The lower shock wave is also moved the toward leading edge. Both the strengths of shock waves are decreased,

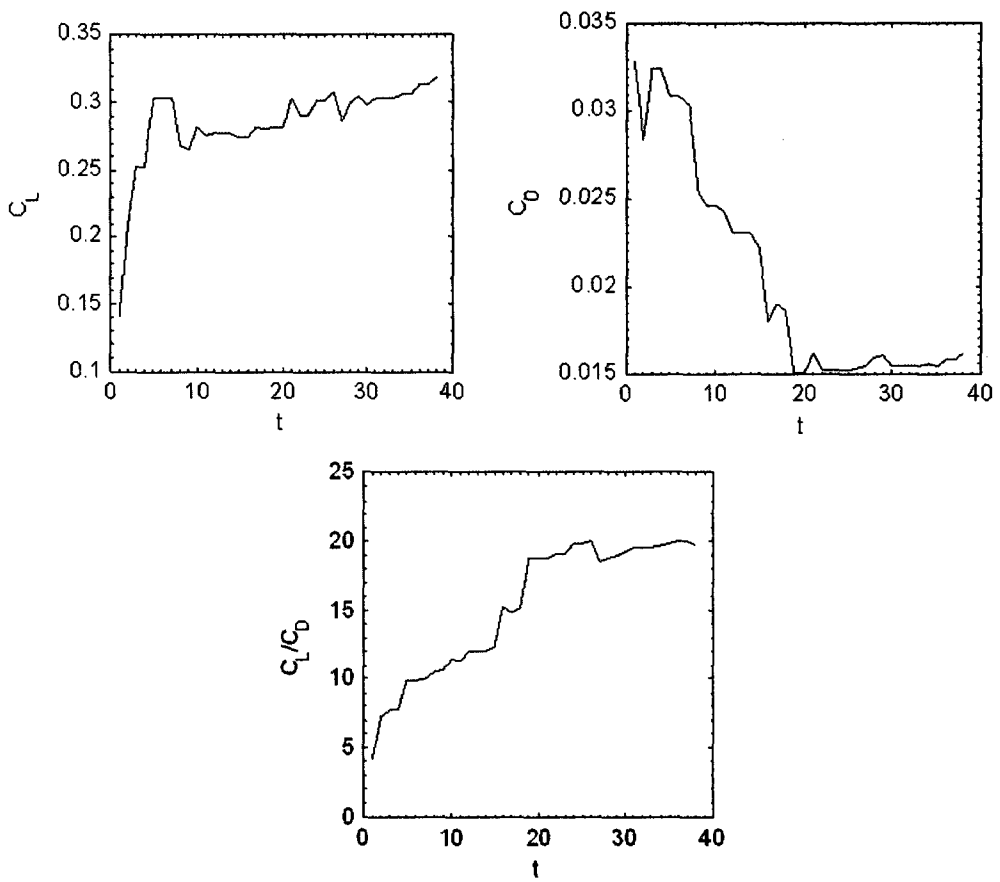

FIG. 53: The change of aerodynamic coefficients and performance during the generations

but there are still shock waves which cannot be ignored.

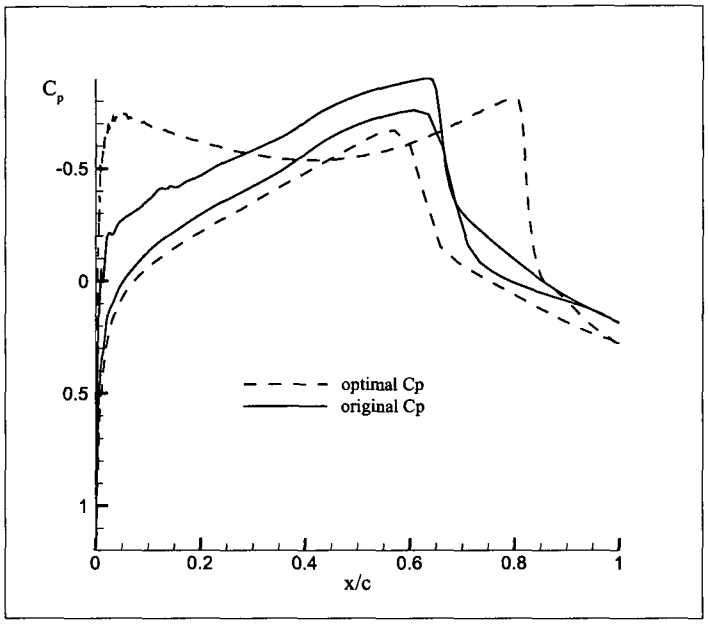

FIG. 54: C_p distributions around *NACA-64A010* and optimized airfoil

Consequently, at the end of the optimization process, C_q, has taken the suction velocity as -0.08871, β became approximately the minimum angle at 3^0 which is tangent to airfoil surface. The location of the actuator seems to be moved together with the upper shock wave location. The upper shock is located at $0.825c$ on the optimal upper surface. The location of the actuator is also located at $0.829c$ which is fairly close to the upper shock wave on the downstream.

The Sequential Optimization of Shape and Flow Control Parameters

In the last case, the shape and flow control parameters are sequentially optimized. For this purpose the resulting shape optimized in the second case is used as a baseline airfoil form. Then, the flow control parameters are optimized on this optimal airfoil form. The genetic optimization process takes only ten generations. At the end of the optimization process, C_q, has taken the suction velocity as -0.1952, β became approximately the minimum angle as 3^0 which is tangent to airfoil surface, and the location arrived at $0.1089c$ which is close to the leading edge. On the other hand,

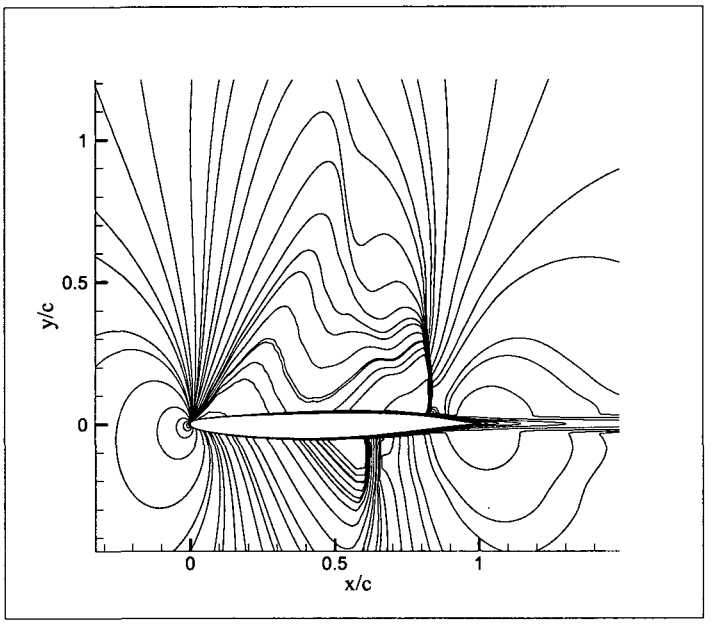

FIG. 55: Mach counters around optimized airfoil shape

the upper shock wave was located at $0.7797c$. Before the flow control operation the upper shock wave was located at $0.782c$. It seems that the suction operations that get a shock wave move backward. The convergence histories of the aerodynamic coefficients, C_L, C_D, and the aerodynamic performance, C_L/C_D, are depicted in Fig. 56. After suction operation at optimal values and optimal location, C_L is increased to 0.2389 which means a 183.76% increment when compared with the original lift coefficient; on the other hand, C_D is decreased to 0.0105 which means a 68% decrement when compared with the original drag coefficient. Interestingly, both the drag portions, the wave and the form drags, are decreased. At the end, C_{WD} takes the value of 0.0058 and CFD takes the value of 0.0046 which is less than the original wave drag. As a result, the objective function is increased to 22.75 which means a 575.80% increment when compared with the original aerodynamic performance. On the other hand, the suction is not located within the periphery of upper shock wave; instead, it is located within the leading edge area. This is probably because of the eliminated shock wave. The weak shock wave causes a low level wave drag. However, the form drag is still strong. Therefore, it seems that the suction is located to decrease the

form drag rather than the wave drag.

In Figs. 57 and 58 resulting C_p distributions and Mach counters are shown. The effect of flow control operations on the pressure coefficient distributions is zoomed in Fig. 57. It seems it has a small scale effect. However, it causes wavy counters on Mach number distributions shown in Fig. 58. Clearly, the optimal values provided by the sequential optimization process are so good. The sequential optimization strategy gives the best aerodynamic performance. The comparative results related to C_L, C_D, and C_L/C_D ratio are depicted in Fig. 59.

V.3.6 Conclusions

In this study, different aerodynamic optimization processes are taken into consideration. At first, only the FC parameters on the upper surface of $NACA-64A010$ airfoil are optimized. At the end of the optimization process, a significant aerodynamic performance enhancement is provided. However, the main part of this success comes from the increment in C_L value rather than the decrease in C_D value. In the second case, only the shape control parameters are optimized. The current symmetric airfoil became an asymmetric, classical transonic airfoil which has almost preserved its maximum thickness ratio. The result includes a significant increase in C_L and a significant decrease in C_D.

In the third case, a simultaneous optimization process is employed. Within this study, both the flow and the shape control parameters are simultaneously optimized. The optimization resulted in a 498.8% increment in aerodynamic performance when compared with the original value. However, the process cannot preserve the maximum thickness ratio constraint. It is observed that the flow control operation diminishes the effect of the thickness ratio and causes a thinner airfoil. Finally, a sequential optimization process is studied. The process has given the best results including a 575.8% increment in aerodynamic performance, a 183.76% increment in C_L, and a 68% decrease in C_D when compared with the original values.

From the results obtained, it is concluded that the optimization strategy has an important effect on the aerodynamic performance. The best way is to optimize the airfoil shape parameters at first and then optimize the AFC parameters.

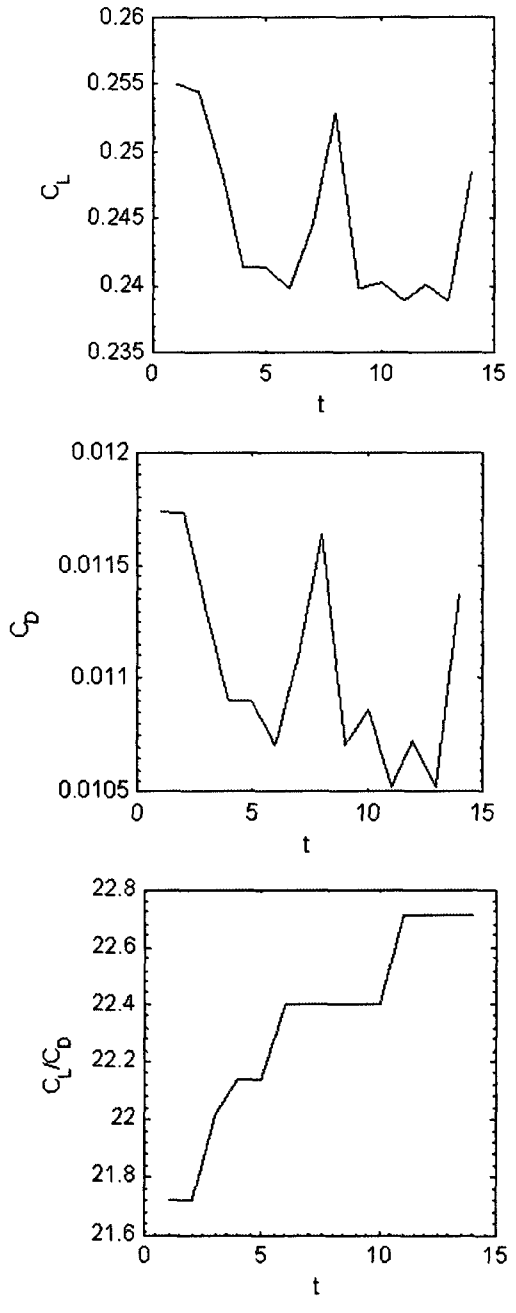

FIG. 56: The change of aerodynamic coefficients and performance during the generations

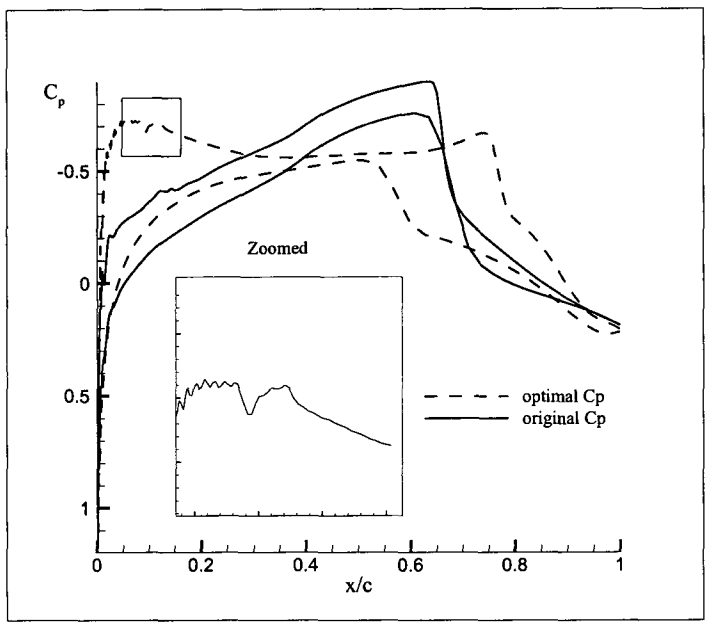

FIG. 57: C_p distributions around *NACA-64A010* and optimized airfoil

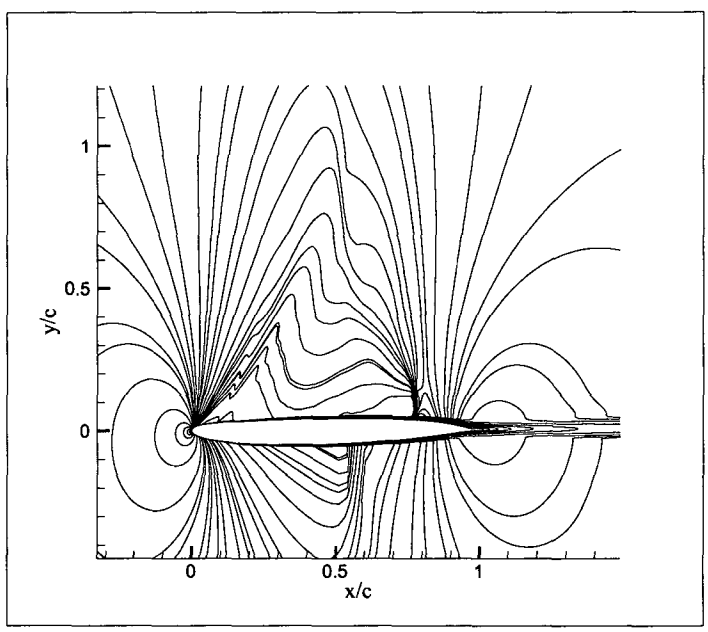

FIG. 58: Mach counters around optimized airfoil shape

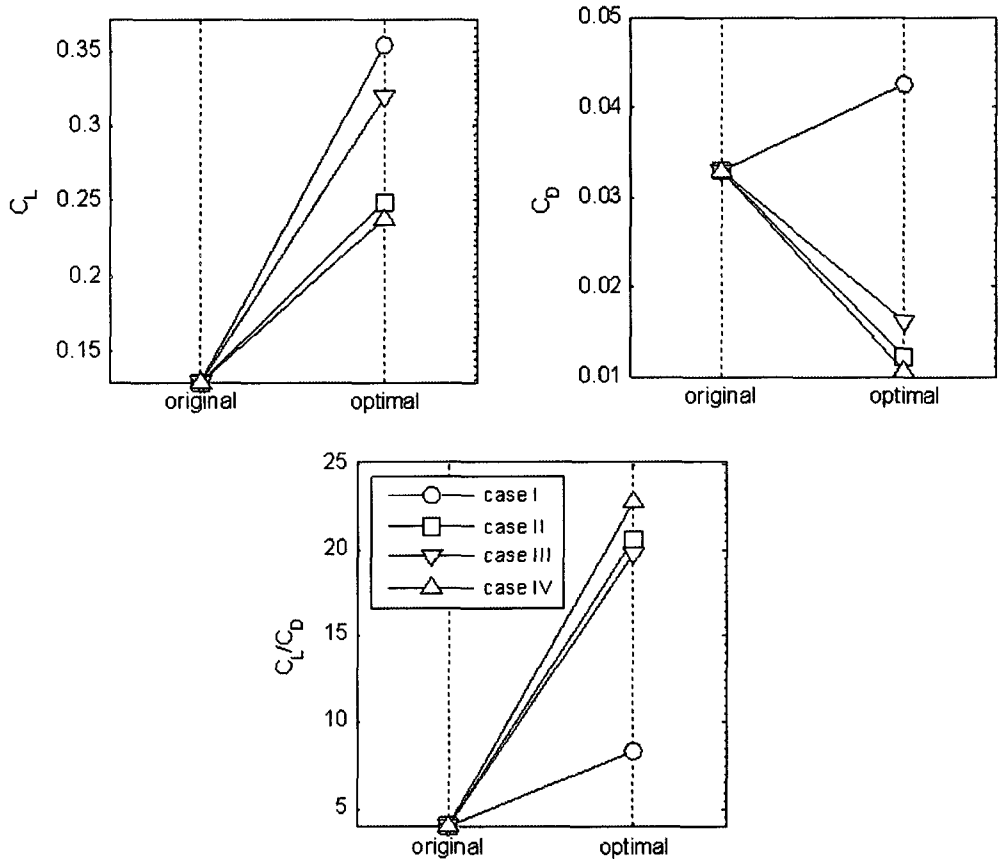

FIG. 59: The comparative results among the constructed optimization cases

CHAPTER VI

CONTROL OF SONIC BOOM

VI.1 INTRODUCTION

The main obstacle for flying supersonically over populated areas is the detrimental effects of Sonic Boom (SB) on the general public and structures. SB is a kind of variation of the ambient air pressure with respect to atmospheric pressure. This acoustic phenomenon is related to bodies flying in the atmosphere at a speed exceeding the local speed of sound[64]. For a supersonic aircraft, the near-field shock structure is a complex array of shocks and pressure waves originating from various parts of the aircraft. The initial rise in pressure, or shock, is due to the coalescence of various shock waves emanating from the forward components of the aircraft. At the same time, the aft pressure rise usually stems from shocks emanating from the back regions of the aircraft. In the far-field, these waves coalesce into the characteristic N-shaped wave[59]. The pressure increase and the rise time are key parameters in SB analysis and they have a major impact on the environment due to its disturbance on the population and damage to surrounding buildings. For this reason, current national regulations do not allow any supersonic flight over land[60]. For a safe supersonic flight, the maximum SB overpressure at ground level is set to be 0.3 pounds per square foot by the "Quiet Supersonic Platform" initiated by the Defense Advanced Research Projects Agency in 2000[61].

For SB mitigation, passive and active suppression methods have been investigated by researcher for many years. Passive suppression studies through the shape optimization include Vazquez et al. (2004)[65], Shields et al. (2008)[66], Farhat et al.(2007)[67], and Rallabhandi et al. (2007)[68]. In 2002 Kandil et al. developed computer code, using three-dimensional non-linear FPE, which marches the SB signal through stratified three-dimensional atmosphere from the near-field to ground level[69]. 14% reduction on the ground level bow shock strength was achieved by using dihedral[70]. A SB mitigation study using 2-level factorial RSM and the steepest descent approach was given by Kandil et al[71], where wing camber, thickness, and nose angle of a delta wing configuration were examined. Dihedral angle was added as a fourth parameter in the multivariable design analysis of a delta wing for SB mitigation by Kandil et al. [72]. Also in 2009, Kandil and Ozcer showed that

a modified F-5E aircraft build by Northrop Grumman, designated as a Shaped SB Demonstrator, is fitted with the optimized axisymmetric nose, and the wings. The final results predict 42% reduction in bow shock strength, 17% reduction in peak ∇p, 22% reduction in pressure impulse, 10% reduction in foot print size, 24% reduction in inviscid drag, and no loss in lift for the optimized aircraft[73]. The study at NASA Dryden[74] clearly shows that passive suppression through the shape optimization alone can have only a limited impact on SB overpressure.

Although shape optimization is an important part of any SB mitigation effort, other methods including active suppression should be employed in order to get a silent supersonic platform. The characteristic of the N-shaped wave can potentially be modified by employing an active system on high speed vehicles which could significantly weaken and disperse the strong shock system. Generally, three types of systems can be distinguished, such as physical spike, mass or energy deposition. Among these systems, the energy addition method encompasses flow manipulation by transferring energy to some points upstream of the aircraft by means of laser, microwaves, electrical discharge, or external combustion, in order to heat or even ionize the flow.

The numerical modeling of pulsed off-body energy addition for SB mitigation has been studied for almost half a century. In the 1970s, the use of off-body heating for SB alleviation was proposed by Cheng Sin[74] to weaken the shock wave. The effect of localized microwave discharge created by a focused off-board microwave beam upstream of a model in a Mach 1.4 flow was investigated by Beaulieu et al.[75]. Another important step in shock wave mitigation was taken by Tretjakov et al. by utilizing a pulsed optical discharge in a supersonic flow to affect the shock structure. Similarly, a single laser pulse was used by Yan et al.[76] to investigate its effects on the shock-wave and flow field structure associated with symmetric intersecting oblique shock waves. Miles et al.[77] indicated that a steady state off-body energy addition can reduce the near-field signature and predicted that it may suppress the far-field coalescence. Experiment and computational modeling performed by Sohail H. Zaidi et al. indicated that energy addition can reduce the near-field signature primarily by suppressing the coalescence of the various shock waves originating from the different parts of the vehicle[78]. However, in that study, it was stated that far-field measurements and numerical investigations are required to optimize the position of the energy source and to see the real impact on the SB signature on the ground.

The probability of elimination or partial reduction of SB on the ground generated from a body moving in the atmosphere at a supersonic speed by adding the energy upstream of the body is discussed in this chapter. The primary aim of this study was to assess the efficiency of upstream energy addition to a supersonic vehicle to weaken the shock strength and to suppress the SB on the ground. The numerical modeling of pulsed off-body energy addition for SB mitigation has been studied for almost half a century. The use of off-body energy addition has been used as an alternative technique for SB mitigation. The optimum location of a pulsed shock based on less power consumption and a suppression of far-field shock waves are investigated.

VI.2 MOTIVATION

SB is a major inhibitor in flying supersonically over the ground. Enabling flying supersonically will have important effect in both the commercial and military sectors. Despite this fact, there is not enough progress achieved over the years and decades in the way of solutions. The efforts to date show that classic approaches to shape optimization separately are not likely to build a credible low boom aircraft which has pressure levels as low as 0.3 psf. The dominant contribution to the SB from an aircraft is from the lift rather than from the volume displacement[77].

There are two crucial parameters for the feeling of SB by the human ear is the overpressure, ∇p, and the rise time, t. The air pressure surrounded by the shock wave is generally only a few psf greater than normal atmospheric pressure, and this additional pressure is called overpressure. Rise time, t, is the releasing time of this overpressure. The overpressure roughly can be divided into two parts: ∇pL, lift overpressure and ∇pV, volume overpressure. ∇p_v decays as 1/2 power of the atmospheric pressure at flight altitude h. ∇p_L is independent of this pressure, because the lift must remain constant with altitude, assuming constant aircraft weight, so the effects of thinner air on ∇pL are offset by an increased angle-of-attack. With the atmospheric pressure decaying exponentially with increasing altitude, ∇pV decays much more rapidly than ∇pL as h increases.

$$\nabla P_L = K_L p_0^{\frac{1}{2}} \frac{(M^2-1)^{\frac{3}{8}}}{M} \frac{W^{\frac{1}{2}}}{l_L^{\frac{1}{4}}} \frac{1}{h^{\frac{3}{4}}} \tag{41}$$

Eq.41 was verified by the measurements at NASA Dryden[74], clearly shows that

shape optimization alone can have only a limited impact on SB overpressure. Although shape optimization should be an important part of any SB mitigation effort, other methods must be employed in order to achieve the goal. Upstream energy addition to supersonic vehicle may attenuate the shock strength and may suppress the SB on the ground.

VI.3 OUTLINE OF PRESENT RESEARCH

The primary aim of the second part of this dissertation is to assess the efficiency of upstream energy addition to a supersonic vehicle to weaken the shock strength and to suppress the SB on the ground.

- Investigate the optimum location of pulsed shock to prevent the merging of generated shocks.
- Impact of attenuation or destruction of near-field the shock waves in SB suppression
- Optimize the location and power of the pulse shock to obtain the minimum overpressure value.

VI.4 PROBLEM CONSTRUCTION

The SB problem modeling can be seen in Fig. 60. In classical SB methodology, the region between the flying object and the ground is usually divided into three sub regions. These are near-field region, mid-field region, and far-field region. Inside the near-field and mid-field regions, the Euler approach is used to predict the flow characteristics. The predicted values are propagated to the ground by using less accurate computational methods, such as the Thomas Code and the ground signature is evaluated to assess the SB effects.

Although the real complex problem is simplified to a smaller scale, similar coalescence of shock waves were generated in order to evaluate the basic effects of energy addition. The simplified model is designed to produce two shock waves that intersect at a specific location below the flying object by using basic oblique shock relation equations. The constructed model is depicted in Fig. 61. According to this model, the angle of the first surface is set to be 35^0, the second angle for the following surface is set as 37.5^0. The free stream Mach number (M_∞) is determined as 2.6. Due to

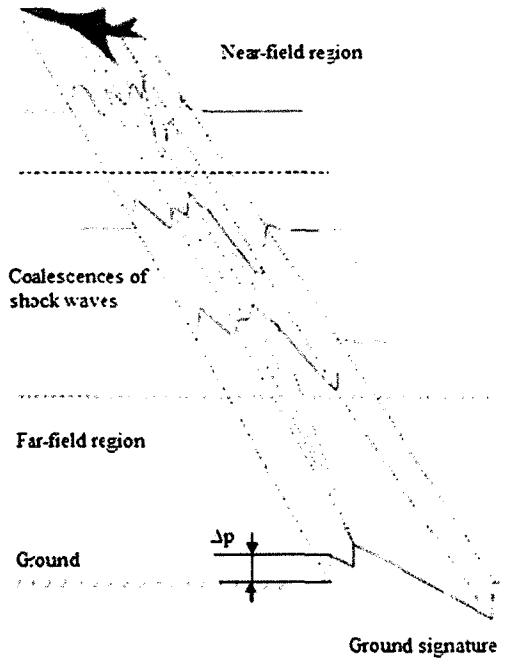

FIG. 60: The model of wave propagation

oblique shocks the speed of flow is decreased to M_1 as 1.9867 and then M_2 as 1.9081. The angles of the first and the second oblique shocks are 14^0 and 29.75^0, respectively. The altitude is set to 32, 140 ft.

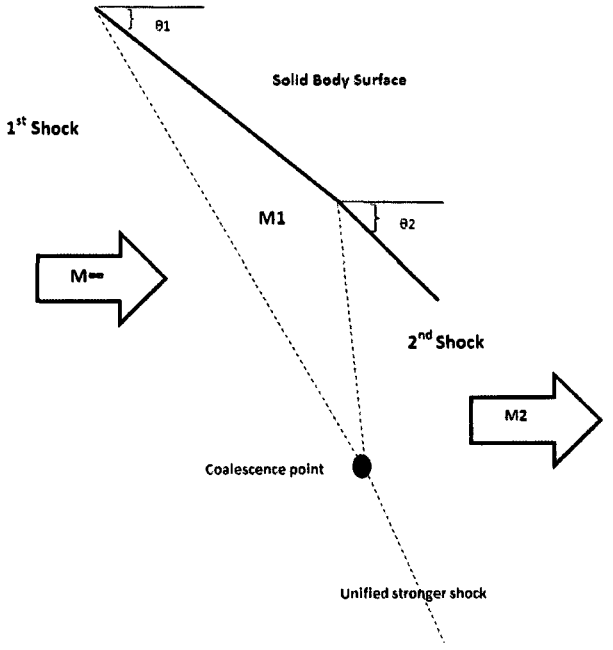

FIG. 61: Problem definition based on oblique shocks

VI.5 COMPUTATIONAL MODELING

VI.5.1 Numerical model for flow analysis

The near-field signature is predicted using $CFL3Dv6.4$, Reynolds Averaged Navier-Stokes code for solving $2D/3D$ flows on structured grids[35], at $M_\infty 2.6$ with 0 angle of attack . In addition to resolving the near-field aerodynamics that produce the SB signature, a computational mesh should provide sufficient resolution beneath the shocks to continue to have a pressure profile away from the supersonic aircraft. The details of the ground signature rely on the accurate calculation of the pressure distribution in the near-field of the aircraft [79]. Because of this, a very fine structure mesh, $801x801$ is used to accurately predict the propagation of shocks. First of all,

steady state solution is obtained without any energy deposition. After that, the pressure value, 5 times the ambient pressure, was imposed at a specific location along a line across the two dimensional domain with a duration of around 100μ s. The energy deposition produces a shock wave called pulsed shock that expands as it propagates in the domain. Then, the pulsed shock waves' propagation and interaction with model shock was observed to comprehend the dynamic effects of energy addition.

VI.5.2 Design parameters and objective function

The design parameters of the optimization problem are determined as the location of the pulsed shock wave. The origin of the domain is set to be the leading edge of the solid body surface. The power of the pulsed shock wave is set to a constant value which is 5 times ambient pressure. The boundaries of the computational domain are qualified as the additional constraints within the optimization process. The design parameters are depicted in Fig. 62.

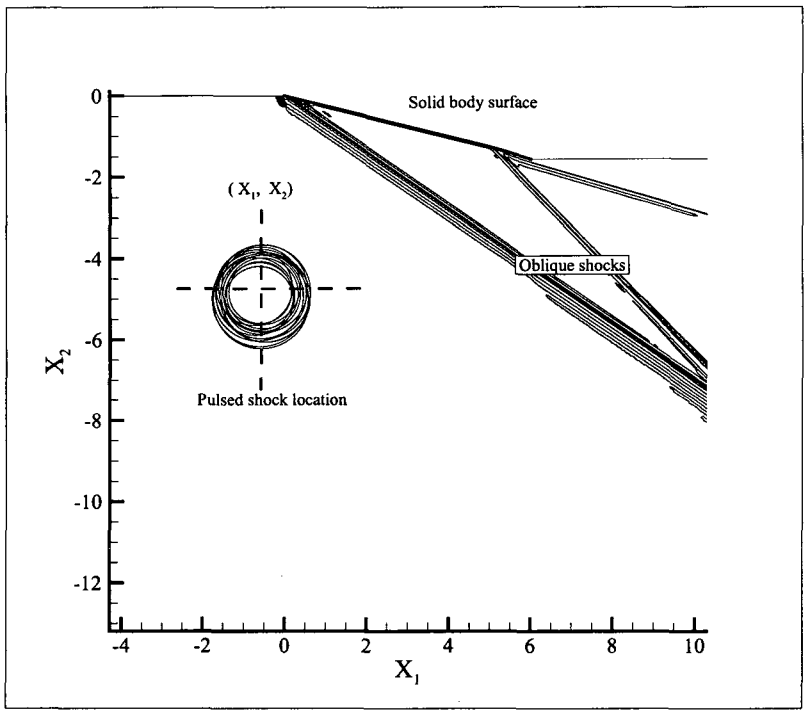

FIG. 62: Design parameters

When describing an objective function, the following issues should be kept in mind. First, a SB is a far-field phenomenon. Therefore, any attenuation, or even a complete destruction of shocks in the near-field area may not result in SB mitigation. Second, any energy-addition operation will be associated with both a weight penalty and a power cost. In general, it is difficult to describe a numerical objective function concerning the first issue for a low boom ground signature. There are some numerical approaches that can be used to describe the fitness of a ground signature, such as the initial and maximum overpressure, or the minimum distance between two consecutive shocks [80]. Furthermore, in the case of energy addition problems the process is dynamic and these changes make the problem much more complex. On the other hand, no approaches are given in the literature to obtain a comprehensive estimate for the energy efficiency consumed by the energy-addition method [81]. However, one of the important parts of an optimization process is to reduce the consumed energy. For that reason, more attention is put on the power cost issue when describing the objective function for the optimization process.

The objective function description, f, for the optimization problem is given below

$$\begin{aligned} Min \quad & f = f_r E^u \\ Subject\ to \quad & \Delta P < \Delta P_1 + \Delta P_2 \\ & -5 \leq x_1 \leq 10 \\ & -20 \leq x_2 \leq -1.7 \end{aligned} \tag{42}$$

where f_r is the laser pulse application frequency, E^u is the constant unit energy per a laser impulse, ΔP_1 is the pressure increase due to the first shock wave, ΔP_2 is the pressure increase due to the second shock wave, and ΔP is the total pressure increment due to the unified shock waves. Normally, the total pressure increment is equal to the sum of ΔP_1 and ΔP_2. However, we predicted that the laser impulse has a serious affect on the unification of the shock waves; therefore, the equality is disturbed by decreasing the total pressure increase. The purpose of determining such an objective function is to minimize the total energy consumed by laser equipment. The application frequency is equal to $1/T$ where T is the period, so, the objective function can be redescribed based on the period, such as

$$Min \qquad f = \frac{E^u}{T}$$

TABLE 15: Optimization Steps

Initialization	
P^I	Determination of initial design points using LHD
$f(x,g)$	Objective function computation
$f^e(x,g)$	Elitism application
RSM_L	Response surface fitting by using local approximation
P^C	New individuals generated by crossover operator
P^P	New individuals predicted by RSM_L
New Population	$P = P^C + P^P$
1^{st} Population	
Design cycle	
$f(x,g)$	Objective function computation
$\|f(x,g) - f(x,g-1)| < \varepsilon$	Convergence check
RSM_L	Response surface fitting by using local approximation
P^C	New individuals generated by crossover operator
P^P	New individuals predicted by RSM_L
P^M	New individuals mutated by mutation operators
New Population	$P = P^C + P^P + P^M$
g^{th} Population	

$$Subject\ to \quad \Delta P < \Delta P_1 + \Delta P_2 \tag{43}$$

$$-5 \leq x_1 \leq 10$$

$$-20 \leq x_2 \leq -1.7$$

In this type of description, the main purpose is to maximize the period that provides less energy consumption while suppressing the coalescence of the oblique shock waves.

VI.5.3 Numerical model for optimization

In this section, we present the main steps of the optimization algorithm used in the SB mitigation problem. The employed optimization algorithm is a real-coded genetic algorithm, and its basic steps are outlined here.

First, we generate the initial population of designs including the individuals, PI. The population size, s, is selected as 9, and the whole individuals are generated in accordance with the optimal orthogonal-array Latin Hypercube Design (LHD) Method. Such designs are seen to have good 'space-filling' properties, covering the

design space well without replication[82]. The generated initial design points are depicted in Fig. 63.

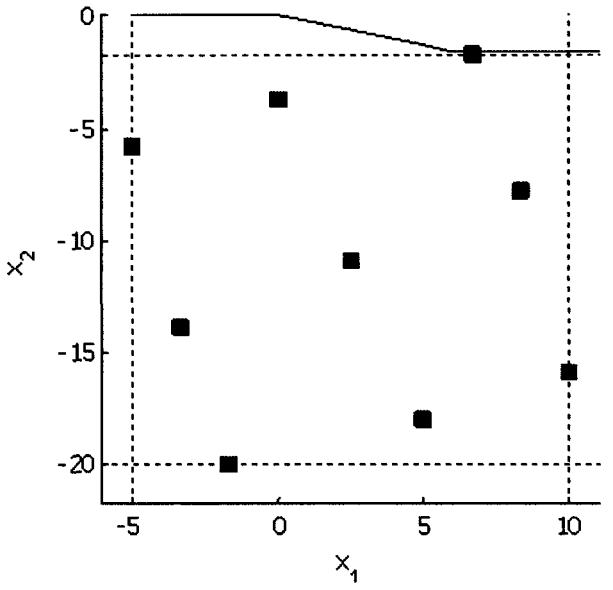

FIG. 63: Initial design points determined by LHD

After initiation all individuals in the population are evaluated by using an exact objective function solver. All of the design points and associated exact values of the objective function are archived in the database. The convergence check is done if the determined criteria whether the tolerance, ε, is satisfied or not. The elitism concept is applied next to ensure that the best objective function value within a population is not reduced from one generation to the next. The procedure for the elite fitness value, $f^e(x,g)$, and elite individual, $x^e(g)$, is as follows:

$$f^e(\mathbf{x},g) = argmin f(\mathbf{x}_i(g)^{i=1,2,\ldots,S},) \;\&\; \mathbf{x}(g) = \mathbf{x}_i(g) \tag{44}$$

$$\mathbf{x}^e(g) = \left\{ \begin{array}{rl} \mathbf{x}^e(g-1), & \text{if } f^e(g) > f^e(g-1) \\ \mathbf{x}^e(g), & \text{if } f^e(g) \leq f^e(g-1) \end{array} \right\} \tag{45}$$

where g is the generation number. In the next step, the factor-response couples are used to construct local response surface models ($RSML$). Radial basis neural

nets (NN) locally approximate the response values as a weighted sum of radial basis functions. In the applications, the $Matlab$ routine, *newrb* is used to construct radial basis NNs [47]. Then, cost weighting fitness scaling and roulette selection procedure for mating are determined [47]. The $Blx-\theta$ with θ=0.5 crossover technique is applied for the new individuals[?]. The design prediction strategy is applied immediately following this crossover phase. In the neural network application, all the genes of an elite individual are mutated as follows:

$$\widehat{f}_L(\mathbf{x}) = \sum_{i=1}^{N_{RBF}} \alpha_i \varphi(\eta) \tag{46}$$

$$\varphi(\eta) = e^{-\eta^2} \tag{47}$$

where α_i is the weight associated with the radial basis function, $\varphi(\eta)$ given in Eq.47. Dummy variable η would be the Euclidean distance between the two vectors such as input, $\mathbf{x}$, and weight, $\mathbf{w}$, vectors. In the applications the Matlab routine *newrb* is used to construct radial basis NNs. Then, cost weighting fitness scaling and roulette selection procedure for mating are determined. The $Blx-\alpha$ with $\alpha = 0.5$ crossover technique is applied for the new individuals [Eshelman]. The new design prediction strategy is applied right after this crossover phase. In the neural network application, all the genes of an elite individual are mutated as follows:

$$P-i,j^{NN}(g) = \left\{ \begin{array}{rl} x_j^e(g)[1 + w_1\gamma_1(1-u)] & \text{if } g = nfr_1^{n=1,2,\cdots}, \\ \phi & \text{if } g \neq nfr_1^{n=1,2,\cdots}, \end{array} \right\} \tag{48}$$

where d is the problem dimension and it is equal to 2, u is a random real number between (0-1), w_1 is a user defined weight number, γ_1 is a user-defined scale factor, f_{rm} is the mutation application frequency. A newly generated temporal population P_NN includes N individuals. The objective function values of this population, f_{NN}, are predicted via a trained neural network, and the best q of them is randomly placed within the population as follows:

$$\mathbf{f}^{NN} = \widehat{f}_L(P^{NN})$$

$$[\mathbf{f}^{NN} \ order] = sort(\mathbf{f}^{NN}) \tag{49}$$

$$(X_k(g))_i = P^{NN}_{order(i),i=1,2,...,q} \quad {}^{k=randint[1,s]}$$

This application provides a local but controlled diversity within the population. At the next design cycle all individuals in the population are evaluated by using an exact objective function solver. This cycle is repeated until the convergence criterion is satisfied.

VI.6 OPTIMIZATION STUDY

The optimization results are depicted in Fig.64. The process takes about 5 generations which means 45 objective function computations. At the end of the optimization process, the coordinates of the energy addition location converge to $(-5, -4.83)$ coordinates. At this location, the period reaches the value of 120 time frame.

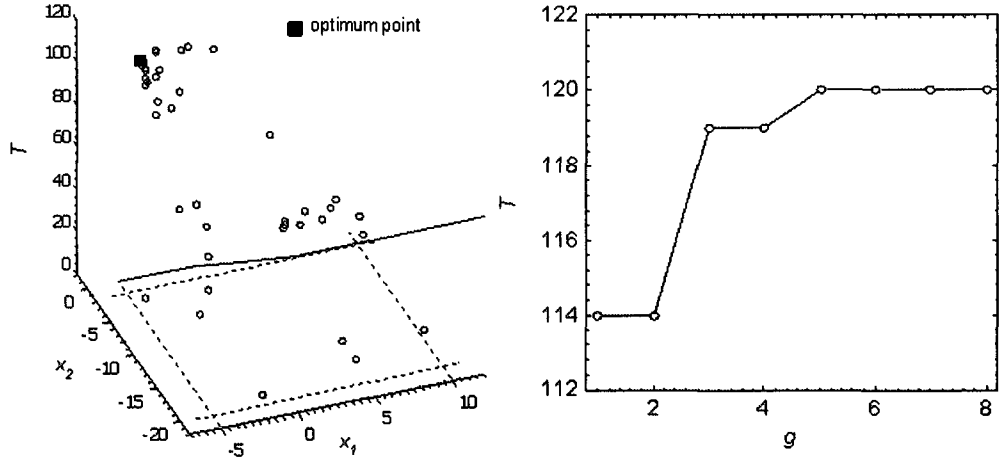

FIG. 64: Optimization process points and the global optimum location for the optimization process (left), convergence history for the period (right)

On the other hand, an example of the interaction of a series of energy addition pulses is shown in Fig. 65. These are eight frames from a movie that show the dynamics of the interaction. The pulse is located on the optimal coordinates at the time, which is equal to zero. While the time advances, the pulse is carried by the

supersonic flow. The pulse waves run into the first shock wave at time frame 15. It also encounters the second shock wave at time frame 20. The pulse arrives at the coalescence point at time frame 30. In the following time frames, the pulse waves and oblique shock waves interact with each other. These interactions disturb the coalescence of the shock waves until time frame 150. Therefore, the time frames between 30 and 150 are the duration for suppressing the coalescence of the shock waves. In Fig. 66, multiple pulses and their interactions with oblique shocks are depicted.

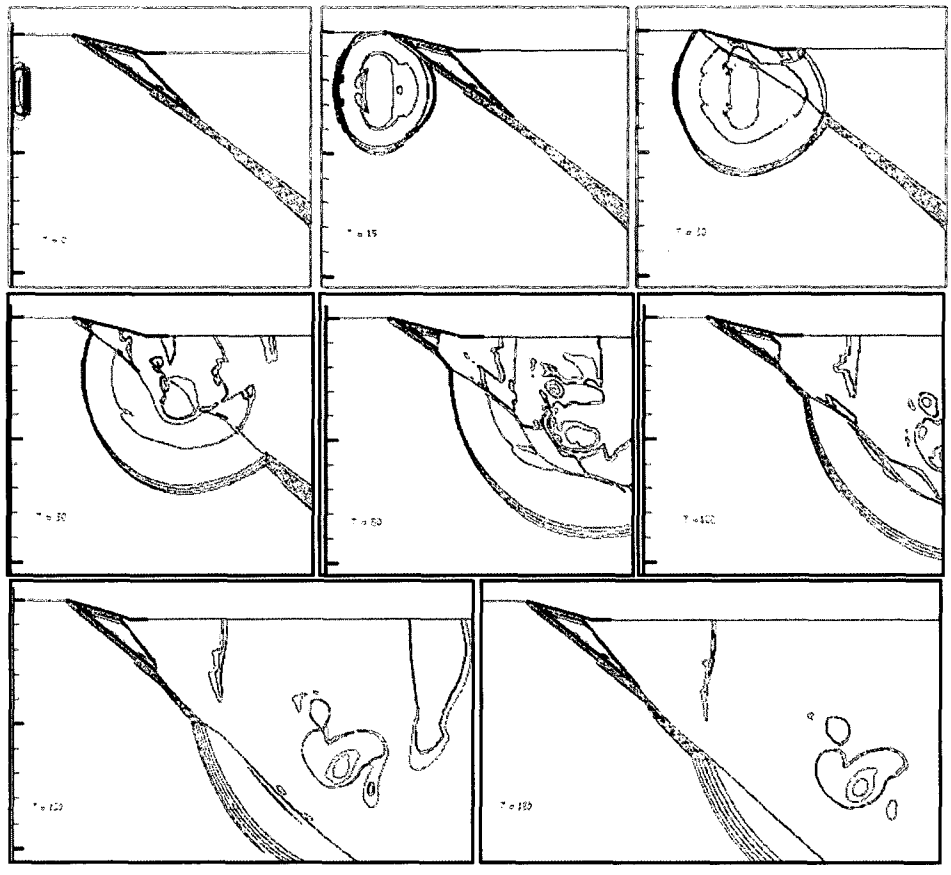

FIG. 65: Sample time frames for the pulse extension in supersonic flow area

FIG. 66: A sample time frame for the multiple energy-addition based pulses in supersonic flow area

VI.7 FAR FIELD RESULT

As seen in Fig. 65, the effect of impulse shock to postpone the interaction is enviable. However, far-field signature has to be investigated in detail to describe the effectiveness of this application because the main goal is the mitigation of the SB signal on the ground. The expectation from the optimization process is that release of off-body energy would decrease the total power requirements to modify the far-field signature, and this pulsed shock suppresses the far-field coalescence and attenuates the SB. As part of this study, one of the far field propagation methods developed by Thomas[83] was linked with $CFL3D$ so that it is utilized as a tool to investigate the impact of off-body energy addition to the far-field signature from a supersonic model. This code uses the near-field pressure distribution as an input to calculate the far-field signature. The near-field pressure data is extrapolated to a specified distance, x_2cut which is equal to 11, far enough away from the supersonic model. This pressure distribution is then propagated to the ground using the Thomas Code. The nonlinear process effects are not considered in this algorithm. Fig. 67 shows the change of max dP for every time step at ground. The max dP (called baseline value) is equal to 0.0518414 without energy addition. After the propagation of pulsed shock, a max dP value is fluctuated between 0.0344798 and 0.0775426. Figs. 68, 69 and 70 clearly illustrates the near-field and far-field results. As pulsed shock generated by energy addition passes through the oblique shock, an important deformation and attenuation of the shock can be observed. Fig. 68 corresponds to a time which is equal to 4.5 sec after the pulse of energy. The pulsed shock primarily affects the oblique shocks generated from the supersonic model; it bends the first oblique shock and kills the second one. Also, the effect of this interaction on the ground signal can be seen in this figure. The difference in the far-field signature and the baseline is crucial to understanding the effect of an added energy. The dP value is increased slightly and then it decreased to a minus value around -0.02. The maximum pressure gradient is consistently lower in value than it is in the absence of the energy addition. Label 2 indicates the time which is equal to 5.2 sec. The second oblique shock still cannot be seen, and the core of the pulsed shock travels on the first one. The form of the supersonic model's ground signature is pulled back relative to the normal wave. The overpressure value is still less than the baseline dP value. Fig. 69 illustrates the following two time steps. Although max dP value for the first time which is equal to 6.7 sec is greater than the baseline value, the overpressure vale is less than the

baseline value. After a short time, dP decreases to 0.046094. In Fig. 70, the initial rise in pressure is pulled back, and its value is less than the baseline. At 9.9 sec, the max dP value is dropped to 0.04649.

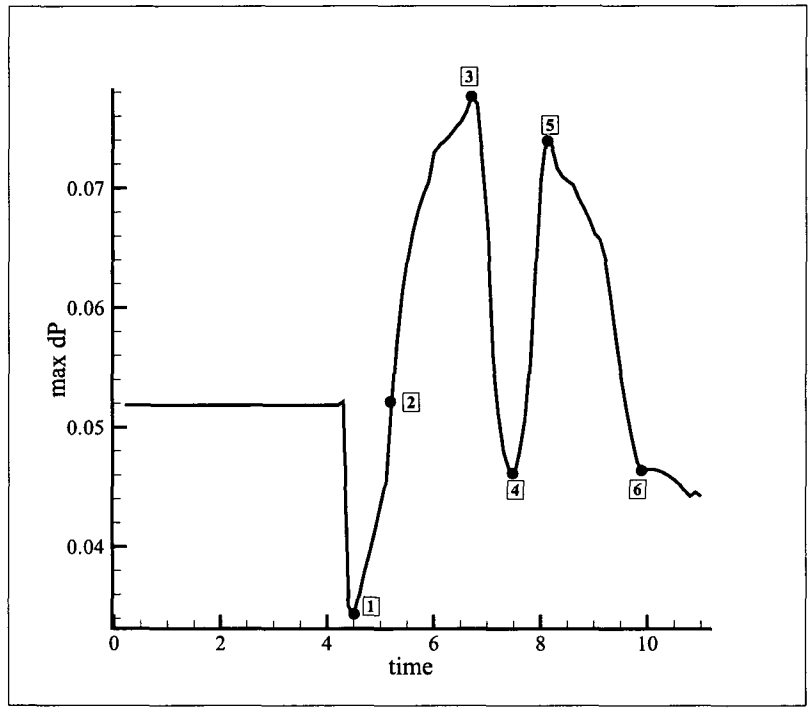

FIG. 67: Maximum dP via time at far-field signature

VI.8 CONCLUSIONS

This study investigates the theory of energy deposition to supersonic airflow off-the model in order to attenuate the SB on the ground. The effect of energy release is demonstrated numerically. A number of numerical calculations have been done on supersonic flow past the region of energy release. The results show the effect of SB mitigation due to energy release with the proper optimization, whereby an appreciable amount of energy could be saved. The calculations are performed as delaying the coalescence of the shock waves and investigating the overpressure of the SB ground signal. These results suggest an essential chance to enable SB reduction using active control based on pulse shock created by energy addition upstream of supersonic

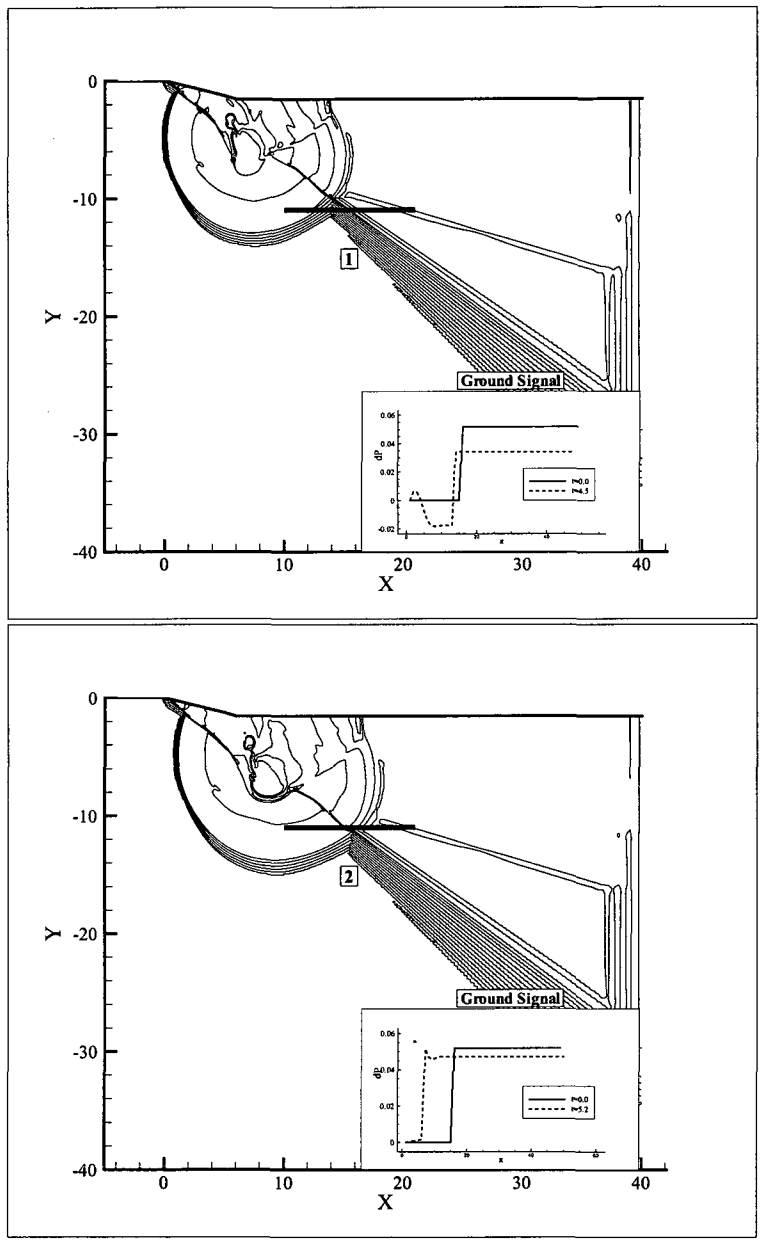

FIG. 68: Near and far field results at points (1) and (2)

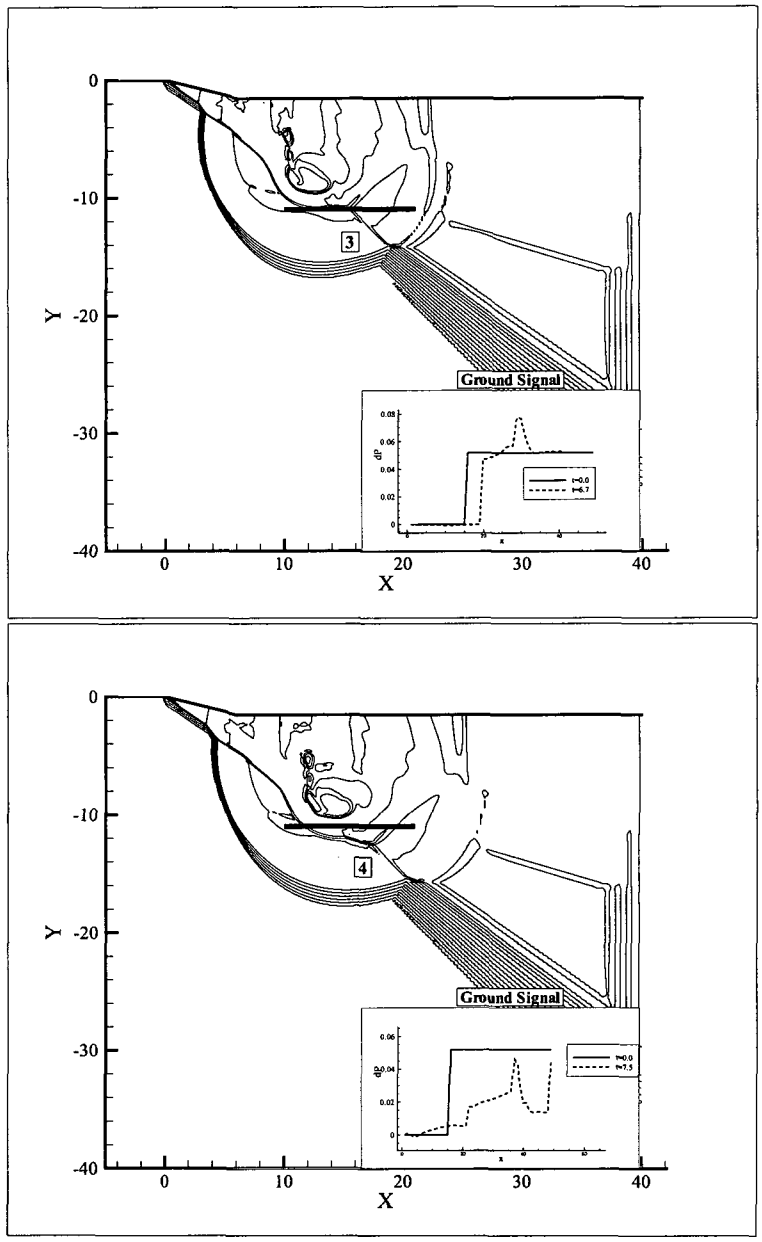

FIG. 69: Near and far field results at points (3) and (4)

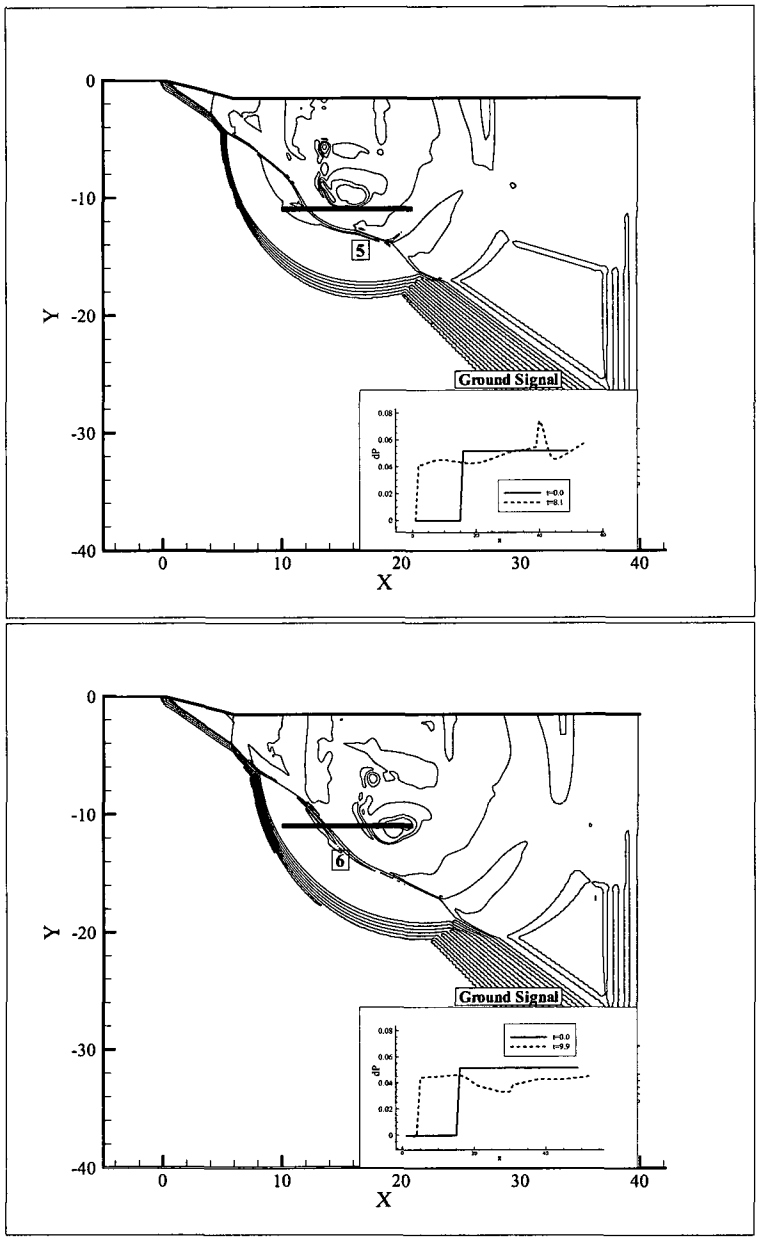

FIG. 70: Near and far field results at points (5) and (6)

aircraft. Given the promising nature of the advanced results presented herein, it is reasonable to expect the development of an efficient SB mitigation methodology that will ultimately become useful in the area of SB suppression.

CHAPTER VII

CONCLUSIONS AND RECOMMENDATIONS

VII.1 CONCLUSIONS

The present study consists of two parts: AFC of shocks and SB ground signature. Three applications were performed by employing active and passive control devices to enhance the overall aerodynamic performance of an airfoil in transonic regime. First, some validation cases have been done against the experimental data regarding pressure distribution and lift and drag coefficients. A grid sensitivity study was performed to ensure the numerical solution accuracy of the governing equations. Then, a parametric study was carried out to understand the physics of control concepts and it demonstrated that the expected improvement in aerodynamic performance were mostly dependent on the mass coefficient, the location and width of the actuator and the jet angle relative to the local tangent. Based on the retrieved results, the following outstanding conclusions are drawn: The surface suction downstream of the transonic shock wave increases the lift with very little penalty in drag and shock strength. This provides an extended low-pressure region after the shock on the upper surface of the aerofoil. A significant lift augmentation was observed for the present suction control applied at the appropriate angle and location of downstream of the shock wave. Blowing ahead of shock generally was found to reduce the lift-to-drag ratio.

Then, a numerical study has been carried out to investigate the benefits of AFC to improve the aerodynamic performance of $2D$ aerofoil, *NACA-64A010*, at transonic speed by using the gradient based optimization technique. The optimization was successfully applied to *NACA-64A010* airfoil with a 1^0 hinged flap and equipped with AFC actuator with the aim of improve the aerodynamic performance. An automated optimization cycle was performed and hereby the computational time was decreased. Unfortunately, the gradient -based optimization method depends on the initial points, so that several optimization runs with different initial values needed to escape the local minimum/maximum points. Additionally, a global search optimization method, GA is employed to make sure that the resulted optimal values are global optimal design variables for one-jet control system optimization. For all cases, to obtain the fully converged solutions, the convergence study on residuals and

forces was done before passing the response values to the optimization program.

A method based on gradient-based approach is exercised to optimize the actuation parameters of the AFC over an airfoil. Optimization work has three parts: maximize the lift-to-drag ratio of the aerofoil with constraints C_D and C_L, applying one-jet control system optimization with single variable; using one-jet control system optimization with multi variables and lastly multi jets control system with multi variables. The single variable optimizations were performed in order to enhance the L/D ratio. First of all, the performance was optimized for jet angle relative to the local normal while keeping the other parameters constant. As compared to the non-control case, the optimization produces 7.76% increment into L/D ratio. The optimal angle is almost tangential to the airfoil surface, 3_0. For second step, by using this optimum jet angle as an initial point, mass flow coefficient is employed for the optimization. C_q optimizations result in 8.91% increase in the objective function. The same process was done for both location and width of jet. Finally, compared to the non-control case, the single variable optimization produces 13.62% increase in the aerofoil transonic aerodynamic performance optimizing jet angle, mass flow coefficient, location and width of the actuator, respectively.

As mentioned earlier, the parameters effectiveness correlates with each other. In order to obtain the best solution, multi variable optimization was introduced. For the initial point, the optimal results obtained from the single variable optimizations are used. The result indicates that, a significant augmentation was observed by using the one-jet four-parameter control system on the downstream of the shock position. The increment was reached to 18.195% with multi variable optimization. Additionally, genetic algorithm is used to validate the results obtained by using gradient based technique. As a result, gradient based optimization and genetic algorithm are converged to same result with different design parameters.

Finally, an optimization study is performed by multi actuators with multi design variables. The upper limit for the width of the actuators is reduced to $0.06c$ to give the actuators more flexible moving location. All the actuators are located at downstream of shock location. The two-jet four-parameter control system optimization results 18.78% increase in L/D ratio. Then, the number of the actuators is increased to three. The final lift-to-drag ratio is reached to 24.2764 which mean 20.06% increments in the aerodynamic performance.

The second application consists of the shock control in the form of $2D$ contour

bump, discrete suction, and combination of these two control techniques, called case hybrid control, importantly reduces total drag without any penalty in lift. The computational studies for the transonic airfoils were, first done with control by a $2D$ contour bump in the shock region. Bump optimization study achieved an augmentation in lift-to-drag ration around 1.55%. As mentioned earlier the objectives of flow control may cause conflict as the achievement of one desired goal may adversely affect another goal. By using bump, all desired goal obtained without any penalty. The result indicates that, the enhancement in lift and decrement in total drag and the mitigation in shock strength can be obtained by using 2d contour bump. In the second part, the surface suction with appropriate selection of C_q, β, x_c decreases the drag with an increment in lift value. At the end of optimization process the resulted optimal values provide 3.17% increase in lift and 3.13% reduction in total drag. The author is cognizant of the fact that there are significant deficiencies about a combination of control mechanisms in transonic regime. The main difference; hence, the contribution of present study is performed at transonic speed via steady suction jet and $2D$ bump together. $2D$ contour bump and discrete suction actuator on the upper surface of airfoil were combined named hybrid control. The drag reduction is increased to 3.94% and the lift increment is raised to 5.04% by using the hybrid control.

The third application includes the optimization of AFC and shape parameters. At first, only the AFC parameters on the upper surface of $NACA-64A010$ airfoil are optimized. At the end of the optimization process, a significant aerodynamic performance enhancement is provided. However, the main part of this success comes from the increment in C_L value rather than the decrease in C_D value. In the second case, only the shape control parameters are optimized. The current symmetric airfoil became an asymmetric, classical transonic airfoil which has almost preserved its maximum thickness ratio. The result includes a significant increase in C_L and a significant decrease in C_D. In the third case, a simultaneous optimization process is employed. Within this study, both the flow and the shape control parameters are simultaneously optimized. The optimization resulted in 498.8% increment in aerodynamic performance when compared with the original value. However, the process cannot preserve the maximum thickness ratio constraint. It is observed that the flow control operation diminishes the effect of thickness ratio and causes a thinner airfoil. Finally, a sequential optimization process is studied. The process has given

the best results including 575.8% increment in aerodynamic performance, 183.76% increment in C_L, and 68% decrease in C_D when compared with the original values. From the results obtained, it is concluded that the optimization strategy has an important effect on the aerodynamic performance. The best way is to optimize the airfoil shape parameters at first, and then to optimize the AFC parameters.

Finally, the last application was performed to investigate the theory of energy deposition to supersonic airflow off-the model in order to attenuate the SB on the ground. The effect of energy release is demonstrated numerically. A number of numerical calculations have been done on supersonic flow past the region of energy release. The obtained results show the effect of SB mitigation due to energy release with the proper optimization, whereby an appreciable amount of energy could be saved. The calculations are performed as delaying the coalescence of the shock waves and investigating the overpressure of the SB ground signal. These results suggest an essential chance to enable SB reduction using active control based on pulse shock created by energy addition upstream of supersonic aircraft. Given the promising nature of the advance results presented herein, it is reasonable to expect the development of an efficient SB mitigation methodology that will ultimately become useful in the area of SB suppression.

VII.2 RECOMMENDATIONS FOR FUTURE RESEARCH

Based on this study, the following recommendations are drawn for future research.

A detailed parametric study and an optimization methodology were introduced and impressive results were obtained in this dissertation. However, a couple of subjects should be interesting to investigate in the future. First, this study should be extended to an application both numerically and experimentally. Second, synthetic jets can be utilized instead of pulsed synthetic jets. It also should be interesting to study further the oscillating response or performance when frequency is varied. Third, a plasma actuator can be used instead of the traditional method. It produces a body force on the external fluids tangential to the airfoil surface without requiring for an air chamber and pneumatic system [84].

Fourth, local and global optimization of a 2D airfoil were performed to improve the aerodynamic performance. This study should be extended to an application for a 3D wing. Fixed wing geometry weakens the overall performance of the aircraft because of the variation of flight and freestream conditions. Wings that are optimized

for a single flight condition can have lower aerodynamic performance throughout the other flight conditions. A wing shape has to have a satisfactory off-design performance. Optimizing an airfoil shape to operate efficiently during the entire flight envelope has been the subject of the major research areas since the 1980s [85, 86, 87]. The adaptive wing technology may enhance take-off, approach-and-landing and cruise performance for contemporary aircrafts by enabling the modification of the wing geometry variation depending upon each task required by the aircraft's mission.

Furthermore, this study examined the energy deposition method in order to mitigate the SB on the ground. To understand the effect of pulsed shock on the SB ground signal, the location and power of pulsed energy were optimized. For future study, series of energy addition pulses can be investigated to obtain a continuous effect on the SB ground signal.

BIBLIOGRAPHY

[1] Gadel-Hak, M., "MODERN DEVELOPMENTS IN FLOW CONTROL," *Appl. Mech. Rev*, Vol. 49, No. 7, 1996, pp. 365–379.

[2] Gadel-Hak, M., "Flow Control: The Future," *Journal of Aircraft*, Vol. 38, No. 3, 2001, pp. 402–418.

[3] GadEl-Hak, M., *Flow Control*, Cambridge University Press, 2000.

[4] Riley, J. J., Gadel-Hak, M., and Metcalfe, R. W., "Compliant Coatings," *Ann Rev Fluid Mech*, Vol. 20, 1988, pp. 393–420.

[5] Bewley, T. R., Choi, H., Temam, R., and Moin, P., "Optimal feedback control of turbulent channel flow," Annual research briefs, 1993, Center for Turbulence Research, Stanford U./NASA Ames.

[6] Vadillo, J. L., *Numerical Studies of tthe Applications of AFC to Subsonic and Transonic Airfol Flows Using a Synthetic Jet Actuator*, Ph.D. thesis, Mechnanical and Aerspace Engineering Dept., Washington Univ.

[7] Kral, L. D., "Active Flow Control Technology," Asme fluids engineering division technical brief, 2000.

[8] Smith, B. L. and Glezer, A., "Jet vectoring using synthetic jets," *Journal Fluid Mech.*, Vol. 458, 2002, pp. 1–34.

[9] Seifert, A. and Pack, L., "Oscillatory Excitation of Unsteady Compressible Flows over Airfoils at Flight Reynolds Numbers," 37th AIAA Aerospace Sciences Meeting and Exhibit, Reno, Nevada, Jan. 11-14, 1999, AIAA 99-0925.

[10] Moin, P. and Bewley, T., "Feedback control of turbulence," *Appl. Mech. Rev.*, Vol. 47, No. 6, 1994, pp. part 2.

[11] Lee, M. and Reynolds, W. C., "Bifurcating and blooming jets," *Rept TF-22, Thermo Sciences Division*, 1985, Dept of Mech Eng, Stanford University.

[12] Nosenchuck, D. M. and Brown, G. L., "Control of turbulent wall shear stress using arrays of TFM tiles," *Bull Am Phys Soc*, Vol. 38, No. 12, 1993, pp. 2197.

[13] Couldrick, S. J., *Study Of Swep And Unswept Normal Shock Wave/Turbulent Boundary Layer Interactionand Control By Piezoelectric Flap Actuation*, Ph.D. thesis, Aerospace, Civil and Mechanica Engineering Dept., University of new South Wales, July, 2006.

[14] Bushnell, D. M. and Hefner, J. N., "Viscous Drag Reduction in Boundary Layers," *AIAA*, 1990.

[15] Chng, T. L., Zha, G., Rachman, A., and Tsai, H. M., "Flow Control of an Airfoil via Injection and Suction," *Journal of Aircraft*, Vol. 46, No. 1, 2009, pp. 291–300.

[16] Chng, T. L., Zhang, J., and Tsai, H. M., "A Novel Method of Flow injection and Suction for Lift Enhancement," 46rd AIAA Aerospace Sciences Meeting and Exhibit, Reno, Nevada, 7-10 Jan 2008, AIAA Paper 2008-335.

[17] Duvigneau, R. and Visonneau, M., "Simulation and Optimization of Aerodynamic Stall Control using a Synthetic Jet," 2nd AIAA Flow Control Conference,, Portland, Oregon, 28 June - 1 July 2004, AIAA Paper 2004-2315.

[18] Arwarts, G., Fono, I., and Seifert, A., "Suction and Oscillatory Blowing Actuator Modeling and Validation," *AIAA*, Vol. 46, No. 5, 2008, pp. 1107–1117.

[19] Vadillo, J. and Agarwal, R. K., "Numerical Study of Transonic Drag Reduction for Flow Past Airfoils Using Active Flow Control," 45th AIAA Aerospace Sciences Meeting and Exhibit, Reno, Nevada, Jan. 8-11, 2007, AIAA Paper 2007-712.

[20] Vadillo, J., Agarwal, R. K., and Hassan, A. A., "Active Control of Shock/Boundary Layer Interaction in Transonic Flow over Airfoils," 43rd AIAA Aerospace Sciences Meeting and Exhibit, Reno, Nevada, Jan. 10-13 2005, AIAA Paper 2005-486.

[21] Smith, D. W. and Walker, J. H., Tech. rep.

[22] Qin, N., Zhu, Y., and Shaw, S. T., "Numerical study of active shock control for transonic aerodynamics," *International Journal of Numerical Methods for Heat and Fluid Flow*, Vol. 14, No. 4, 2004, pp. 444–466.

[23] Qin, N., Zhu, Y., Ashill, P., and Shaw, S. T., "Active Flow Control of Transonic Aerodynamics Using Suction, Blowing. Bumps and Synthetic Jets," AIAA Applied Aerodynamics Conference, 18th, Denver, CO, Aug. 14-17, 2000, AIAA Paper 2000-4329.

[24] Anders, S. G., Sellers, W. L., and Washburn, A. E., "Active Flow Control Activities at NASA Langley," 2nd AIAA Flow Control Conference, Portland, Oregon, 28 June - 1 July 2004, AIAA Paper 2004-2623.

[25] Meunier, M., "Simulations of Flow Control Strategies for Novel High-Lift Configurations," *AIAA*, Vol. 47, No. 5, 2009, pp. 1145–1157.

[26] Merriam-Webster, o. D., "http://www.merriam-webster.com," 2009.

[27] Belegundu, A. D. and Chandrupatla, T. R., *Optimization Concepts and Applications in Engineering*, Prentice Hall, Upper Saddle River, NJ, 1999.

[28] Choudhary, R. and Michalek, J., "http://www.cmu.edu/me/ddl/publications," 2009.

[29] Pike, W. R., *Optimization for Engineering Systems*, Minerals Processing research Institute, 2001.

[30] Holland, J. H., *Adaptation in natural and artificial system*, Ann Arbor, The University of Michigan Press, 1975.

[31] Entz, R. M. U., Correa, L. G. N., Oliveria, R. F., Catalano, F. M., and Medeiros, M. A. F., "Methods for Preliminary Airfoil Optimization," 27rd AIAA Applied Aerodynamics Conference, San Antonio, TX, 22-25 June 2009, AIAA Paper 2009-3774.

[32] Rumsey, C., Biedron, R., and Thomas, J., "CFL3D: Its History and Some Recent Applications," Nasa/tm-112861, 1997.

[33] Baysal, O., Fouladi, K., and Lessard, V. R., "A Multigrid and Upwind Viscous Flow Solver on Three-Dimensional Overlapped and Embedded Grids," *AIAA*, 1990, 29: 903-910.

[34] Bartels, R. E., Rumsey, C. L., and Biedron, R., "CFL3D Version 6.4: General Usage and Aeroelastic Analysis," Nasa/tm-2006-214301, 2006.

[35] Krist, S. L., Biedron, R. T., and Rumsey, C. L., *CFL3D User's Manual Version 5.0,NASA/TM-1998208444*, June 1998.

[36] Bur, R., Corbel, B., and Delery, J., "Study of passive control in a transonic shock wave/boundary layer interaction," 35th AIAA Aerospace Sciences Meeting and Exhibit, Reno, Nevada, Jan. 6-9 1997, AIAA Paper 97-0217.

[37] Delery, J., "Investigation of Strong Shock Turbulent Boundary Layer Interaction in 2D Transonic Flows with Emphasis on Turbulence Phenomena," AIAA 14th Fluid and Plasma Dynamics Conference, Pali Alto, California, Jun. 23-25 1981, AIAA 81-1245.

[38] Manual, C., "http://cfl3d.larc.nasa.gov," 2009.

[39] Spalart, P. and Allmaras, S., "One-Equation Turbulence Model for Aerodynamic Flows," *AIAA*, 1992, 92-0439.

[40] *VisualDOC User Manual, Vanderplaats Research and Development, Inc.*, Colorado Springs, 2002.

[41] Pehlivanoglu, Y. V., *Hybrid Inteligent Optimization Methods for Engineering Problems*, Ph.D. thesis, Aerospace Engineering Dept., Old Dominion Univ, 2010.

[42] Meet Zorka, O. f. T. C. C., "http://www.odu.edu/news," 2009.

[43] Koklu, M., *Micro Synthetic Jets as Effective Actuators*, Ph.D. thesis, Aerospace Engineering Dept., Old Dominion Univ, 2007.

[44] Pehlivanoglu, Y. V. and Baysal, O., "Vibrational Genetic Algorithm Enhanced with Fuzzy Logic and Neural Network," *Aerospace Science and Technology*, Vol. 14, No. 7, 2009, pp. 56–64.

[45] Haupt, R. L. and Haupt, S. E., *Practical Genetic Algorithms, 2nd Edition*, A John Wiley Sons Inc. Publication, 2004.

[46] Eshelman, L. J. and Schaffer, J. D., *Real Coded Genetic Algorithms and Interval Schemata, Foundations of Genetic Algorithms 2*, Morgan Kaufmann Publishers, 1993.

[47] Neural Network Toolbox, M., *The language of technical computing*, Version R2007b, The MathWorks, Inc., 2007.

[48] Yeshala, N., Min, B., and Sankar, L. N., "Drag Reduction Studies Using Active Flow Control," 4th AIAA Flow Control Conference, Wahington, DC, 23-26 June 2008, AIAA Paper 2008-3870.

[49] Han, Z. H., Zhang, S., Song, W. P., and Qiao, D., "Optimization of Active Flow Control over an Airfoil Using Surrogate Management Framework," 47th AIAA Aerospace Sciences Meeting, Orlando, Florida, 5-8 Jan. 2009, AIAA Paper 2009-1280.

[50] Qin, N., Zhu, N., and Poll, D. I. A., "Surface suction on aerofoil aerodynamic characteristics at the transonic speeds," *Proceedings of IMechE Part G J. Aeronautical Engineering*.

[51] Stanewsky, E., "Adaptive wing and flow control technology," *Progress in Aerospace Sciences*, Vol. 37, No. 7, 2001, pp. 583–667.

[52] Shmilovich, A. and Yadlin, Y., "Flow Control for the Systematic Buildup of High-Lift Systems," *Journal of Aircraft*, Vol. 45, No. 5, 2008, pp. 1680–1688.

[53] Stanewsky, E., Delery, J., Fulker, J. L., and de Matteis, P., *Drag reduction by shock and boundary layer control, in: Results of The Project EUROSHOCK II, in: Notes On Numerical Fluid Mechanics And Multidisciplinary Design*, Springer, 2001.

[54] Birkemeyer, J., Rosemann, H., and Stanewsky, E., "Shock control on a swept wing," *Aerospace Science and Technology*, , No. 4, 2000, pp. 147–156.

[55] Wong, W. S., Qin, N., Sellars, N., Holden, H., and Babinsky, H., "A combined experimental and numerical study of flow structures over three-dimensional shock control bumps," *Aerospace Science and Technology*, Vol. 10, No. 11, 2007, pp. 436–447.

[56] Fulker, J. L. and Simmons, M. J., "An experimental study of shock control methods," Ra/as/hwa/tr94007/1, 1994.

[57] Yagiz, B. and Kandil, O. A., "Optimization of Active Flow Control in Transonic Aerodynamics," 27rd AIAA Applied Aerodynamics Conference, San Antonio, TX, 22-25 June 2009, AIAA Paper 2009-3763.

[58] Leoviriyakit, K., Kim, S., and Jameson, A., "Viscous Aerodynamic Shape Optimization of Wings including Planform Variables," 21st Applied Aerodynamics Conference Orlando, Orlando, Florida, June 23-26, 2003, AIAA 2003-3498.

[59] Khasdeo, N., Kandil, O. A., and Ozcer, I. A., "Optimization of delta wing geometry parameters for sonic boom mitigation," 37th AIAA Fluid Dynamics Conference and Exhibit, Miami, FL, 25 - 28 June 2007, AIAA 2007-4109.

[60] Longo, J. M. A., Dittrich, R., Banuti, D., Sippel, M., Klevanski, J., Atanassov, U., Carrier, G., Duveau, P., Salah, E. D. I., Thepot, R., Loubeau, A., Coulouvrat, F., Jarlas, R., Rabia, H., Perigo, D., and Steelant, J., "Concept study for a Mach 6 transport aircraft," 47th AIAA Aerospace Sciences Meeting Including The New Horizons Forum and Aerospace Exposition, Orlando, Florida, 5-8 January 2009, AIAA 2009-435.

[61] Pawlowski, J. W. and Graham, D. H., "Optimization of delta wing geometry parameters for sonic boom mitigation," 37th AIAA Fluid Dynamics Conference and Exhibit, Miami, FL, 25 - 28 June 2007, AIAA 2007-4109.

[62] Farin, G., *Curves and Surfaces for Computer Aided Geometric Design*, A Practical Guide, Academic Press, 1993.

[63] Hassan, A. A., Osborne, B., Schwimley, S., and Billman, G., "Control of Shock-Boundary Layer Interactions (SBLIs) Using An Oscillatory Jet," 45th AIAA Aerospace Sciences Meeting, Reno, Nevada, Jan. 8-11 2007, AIAA Paper 2007-0476.

[64] Alauzet, F. and Loseille, A., "High-order sonic boom modeling based on adaptive methods," *Journal of Computational Physics*, Vol. 229, No. 3, 2010, pp. 561–593.

[65] Vazquez, M., Dervieux, A., and Koobus, B., "Multilevel optimization of a supersonic aircraft," *Finite Elements in Analysis and Design*, Vol. 40, No. 15, 2004, pp. 2101–2124.

[66] Shields, W. L. E. and Le, D., "Interactive inverse design optimization of fuselage shape for low-boom supersonic concepts," *Journal of Aircraft*, Vol. 45, No. 4, 2008, pp. 1381–1397.

[67] Farhat, C., Maute, K., Argrow, B., and Nikbay, M., "Shape optimization methodology for reducing the sonic boom initial pressure rise," *AIAA Journal*, Vol. 45, No. 5, 2007, pp. 1007–1018.

[68] Rallabhandi, S. K. and Mavris, D. N., "Aircraft geometry design and optimization for sonic boom reduction," *Journal of Aircraft*, Vol. 44, No. 1, 2007, pp. 35–47.

[69] Kandil, O. A., Yang, Z., and Bobbitt, B. J., "Prediction of Sonic Boom Signature Using Euler-Full Potential CFD With Grid Adaptation and Shock Fitting," 8th AIAA/CEAS Aeroacoustics Conference, Breckenridge, CO, 2002, AIAA 2002-2542.

[70] Bobbitt, P., Kandil, O. A., and Yang, Z., "The Beneficial Effects of Wing Dihedral on Sonic Boom," Aeroacoustics Conf, Hilton Head, SC, 2003.

[71] o A Kandil, Khasdeo, N., and Ozcer, I. A., "Sonic Boom Mitigation through Thickness, Camber, and Nose Angle Optimizations for a Delta Wing," AIAA Atmospheric Flight Mechanics Conference and Exhibit, Colorado, Keystone, 2006, AIAA 2006-6636.

[72] Kandil, O. A., Khasdeo, N., and i A Ozcer, "Optimization of Delta Wing Geometry Parameters for Sonic Boom Mitigation," 37th AIAA Fluid Dynamics Conference and Exhibit, Miami, FL, 2007, AIAA 2007-4109.

[73] Ozcer, I. A., *Multidisciplinary Design Optimization for Sonic Boom Mitigation*, Ph.D. thesis, Aerospace Engineering Dept., Old Dominion Univ, 2009.

[74] Cheng, S. I. and Goldburg, A., "Aircraft Engine Noise and Sonic Boom," Nato agardconference proc, May 1969.

[75] Beaulieu, W., Brovkin, V., Goldberg, I., Klimova, A., Kolesnichenko, Y., Krylov, A., Lashkov, V., Leonov, S., Mashek, I., Ryvkin, M., and Serov, Y., "Microwave Plasma Influence on Aerodynamic Characteristics of Body in Airflow," Proceedings of the 2nd Weakly Ionized GasesWorkshop, Reston, VA, 1998, pp. 193–199.

[76] Yan, H., Elliott, R. A. G., and Knight, D., "Laser Energy Deposition in Intersecting Shocks," June 2002, AIAA Paper 2002-2729.

[77] Miles, R. B., Martinelli, L., Macheret, S. O., Shneider, M. N., Girgis, I. H., Zaidi, S. H., and Mansfield, D. K., "Suppression of Soinc Boom by Dynamic Off-Body Energy and Shape Optimization," Jan. 2002, AIAA Paper 2002-0150.

[78] Zaidi, S. H., Shneider, M. N., and Miles, R. B., "Shock wave mitigation through off-body pulsed energy deposition," *AIAA Journal*, Vol. 42, No. 2, 2004, pp. 326–331.

[79] Choi, S., Alonso, J. J., and der Weide, E. V., "Numerical and Mesh Resolution Requirements for Accurate Sonic Boom Prediction of Complete Aircraft," 42nd AIAA Aerospace Sciences Meeting and Exhibit, Reno, Nevada, Jan. 5-8, 2004, AIAA-2004-1060.

[80] Plotkin, K. J., Rallabhandi, S. K., and Li, W., "Generalized formulation and extension of sonic boom minimization theory for front and aft shaping," 47th AIAA Aerospace Sciences Meeting Including The New Horizons Forum and Aerospace Exposition, Orlando, Florida, Jan. 2009, AIAA-2009-1052.

[81] Fomin, V. M., Tretyakova, P. K., and Taranb, J. P., "Flow control using various plasma and aerodynamic approaches (Short review)," *Aerospace Science and Technology*, Vol. 8, 2004, pp. 411–421.

[82] Leary, S., Bhaskar, A., and Keane, A., "Optimal orthogonal-array-based Latin hypercubes," *Journal of Applied Statistics*, Vol. 30, No. 5, 2003, pp. 585–598.

[83] Thomas, C. L., "Extrapolation of Sonic Boom Pressure Signatures by the Waveform Parameter Method," Nasa tn-d-6832, June 1972.

[84] Zhang, P. F., Yan, B., Liu, A. B., and Wang, J. J., "Numerical Simulation on Plasma Circulation Control Airfoil," *AIAA*, Vol. 48, No. 10, 2010, pp. 2213–2226.

[85] Renken, J. H., "Mission - Adaptive Wing Camber Control Systems for Transport Aircraft," 3rd Applied Aerodynamic Conference, Colorado Springs, Colorado, October 14-16, 1985, AIAA 85-5006.

[86] DeCamp, R. W. and Hardy, R., "MISSION ADAPTIVE WING ADVANCED RESEARCH CONCEPTS," *American Institute of Aeronautics and Astronautics*, 2008, AIAA 85-2088.

[87] Bonnema, K. L. and Smith, S. B., "AFTI/ F-111 MISSION ADAPTIVE WING FLIGHT RESEARCH PROGRAEI," 1988, AIAA 88-38719.

[88] Eberhart, R. C. and Kennedy, J., "A New Optimizer Using Particle Swarm Theory," In Proc. 6th Int. Symp. Micromachine Human Science, Nagoya, Japan, 1995, pp. 39–43.

[89] Roe, P., "Approximate Riemann Solvers, Parameter Vectors, and Difference Schemes," *Journal of Computational Physics,*, 1981, Vol. 43.

[90] Blokhintsev, D. I., "Acoustics of a Nonhomogeneous Moving Medium. Gostekhizdat, Moscow," Translated as naca tm 1399, 1956.), 1946.

This page intentionally left blank

APPENDIX A

PSO OF AFC ON AN AIRFOIL AT TRANSONIC REGIME

A.1 INTRODUCTION

In the previous study, the capability of weakening the shock waves to improve the aerodynamic performance in transonic conditions is evaluated using surface suction/blowing on airfoils via a gradient-based optimization process. The desired goal of the present study is to improve the aerodynamic performance on airfoils at transonic speeds by optimizing the surface suction/blowing parameters using a non-gradient based global algorithm, the Particle Swarm Optimization, method to search for an improved design. For selected cases, obtained results are compared to those from a gradient-based algorithm. For the flow simulations, a time-dependent, turbulent flow solver developed at NASA Langley Research Center is used on structured grids. Present computations were performed for Mach 0.78 flow past a $NACA64A010$ airfoil at an angle of attack of 0.5^0 with and without AFC.

A.2 OPTIMIZATION

During the optimization processes the swarm size, S, is taken as 10, the inertia weight, w, is decreased linearly starting from 0.6 and ending at 0.3 related to the maximum iteration number G, which is equal to 100. The mutation frequency, f_m, is equal to 5, scale factor, A, is equal to 0.5, c_1 is equal to 2, c_2 is equal to 2. In the computational phase two-level parallelization is implemented. The first parallelization is applied in the swarm. Each particle objective function value within the swarm is computed on different processors in a parallel way. The flow solver code is also appropriate for parallel computing. Therefore, the second level parallelization is applied in the flow solver.

A.2.1 Particle Swarm Optimization

As in other evolutionary algorithms, the Particle Swarm Optimization (PSO) method is a population-based stochastic algorithm that originates from the "nature" and "evolutionary computations." Often these algorithms may require more cost function evaluations than comparable gradient-based algorithms. They, however, provide

attractive characteristics such as ease of implementation for both continuous and discrete problems, efficient use of large numbers of parallel processors, no requirement for the continuity in response functions, and more robust solution generations for searching global or near global solutions. PSO algorithms search the optimum within a population called "swarm." It benefits from two types of learning: "cognitive learning" based on individual's own history and "social learning" based on swarm's own history accumulated by sharing information among all particles in the swarm. Since its development in 1995 by Kennedy et al.[88], it has attracted significant attention and popularity.

A general optimization problem can be expressed as follows:

$$Minf(x)$$

Subject to:

$$\begin{aligned} g_j(\mathbf{x}) \leq 0 \qquad & j = 1, 2, ..., m \\ h_k(\mathbf{x}) = 0 \qquad & k = 1, 2, ..., l \\ \mathbf{x}^L \leq (\mathbf{x}) \leq \mathbf{x}^U \quad & i = 1, 2, ..., D \end{aligned} \tag{50}$$

where $\mathbf{x}$ is a column vector of real valued design variables, $f(\mathbf{x})$ is the objective function, g_j is inequality constraint, h_k is equality constraint, $\mathbf{x}^L$ and $\mathbf{x}^U$ are the side constraints for the design variables. For the present PSO set up; let S be the swarm size, D be the particle dimension space, and each particle of the swarm has a current position vector $\mathbf{x}_i$, current velocity vector v_i, individual best position vector $\mathbf{P}_i$ found by the particle itself. The swarm also has the global best position vector $\mathbf{P}_g$ found by any particle during all prior iterations in the search space. Assuming that the function f is to be minimized and describing the following notations in t_{th} generation, then the definitions are as follows:

$$\begin{aligned} \mathbf{x}_i(t) &= (x_{i,1}(t), x_{i,2}(t), ..., x_{i,j}(t)), \quad x_{i,j}(t) \in R^{D,^{i=1,2,...,S}} \\ v_i(t) &= (v_{i,1}(t), v_{i,2}(t), ..., v_{i,j}(t)), \quad v_{i,j}(t) \in R^{D,^{i=1,2,...,S}} \end{aligned} \tag{51}$$

where each dimension of a particle in the swarm is updated using the following equations:

$$v_{i,j}(t) = w(t)v_{i,j}(t-1) + c_1 r_1(P_i(t-1) - x_{i,j}(t-1)) + c_2 r_2(P_g(t-1) - x_{i,j}(t-1))$$

$$x_{i,j}(t) = x_{i,j}(t-1) + v_{i,j}(t) \tag{52}$$

In Eq.52, c_1 and c_2 denote constant coefficients, r_1 and r_2 are elements from random sequences in the range of $(0,1)$. The parameter c_1 controls the influence degree of the "cognitive" part of an individual, and c_2 determines the effect of the "social" part of the swarm. The inertia weight, w, is decreased linearly starting at one point and ending at the other point related to maximum iteration number, G. The personal best position vector of each particle is computed using the following expression:

$$P_i(t) = \left\{ \begin{array}{rl} P_i(t-1), & \text{if } f(\mathbf{x}_i(t)) \geq f(P_i(t-1)) \\ \mathbf{x}_i(t), & \text{if } f(\mathbf{x}_i(t)) < f(P_i(t-1)) \end{array} \right\} \tag{53}$$

Then, the global best position vector is found by

$$P_g(t) = \mathbf{argmin} f(P_i(t)) \tag{54}$$

The drawback of PSO is the lack of diversity. Therefore, we applied mutation operations during the generations. Mutation operators introduce new individuals into a population by manipulating a current individual, thus adding diversity into the population and probably preventing stagnation of the search in local optima. The traditional general form of the mutation, which was applied in the classical PSO algorithm can be written as $x_{i,j}(t) = M(x_{i,j}(t))$, where M is the mutation operator providing the offspring vector. Instead of this strict form of a mutation operator it can be described including a mutation strategy as follows:

$$x_{i,j}(t) = \Im(M(x_{i,j}(t)), f_m) \tag{55}$$

where $\Im$ the generalized mutation function, f_m is a user defined frequency. In every f_m^-1 period of the generations applying the mutation operator to all particle dimensions of the whole swarm, individuals in the population spread throughout the design space. The mutation operator is given by,

$$x_{i,j}(t) = x_{i,j}(t)[1 + A.rand.\delta]_{1=1,2,\ldots,S}^{j=1,2,\ldots,D} \quad and \; \delta = \left\{ \begin{array}{ll} 1 & \text{if } t = nf_m, n = 1,2,\ldots \\ 0 & \text{if } t \neq nf_m \end{array} \right\} \tag{56}$$

where A is a user defined scale factor called an amplitude and it may be selected as a fixed number or computed during the iterations, rand is a real random number specified by random number generator.

A.3 DESIGN PARAMETERS AND OBJECTIVE FUNCTION

A nonlinear-constrained optimization problem for an airfoil can be expressed as follows:

$$min f_{X \epsilon R^D} = \frac{C_D}{C_L}$$

Subject to:

$$\begin{aligned} -C_L + C_L^* &\leq 0 \\ \mathbf{x}^L \leq \mathbf{x} &\leq \mathbf{x}^U \end{aligned} \tag{57}$$

where C_L^* is the design lift coefficient. In the PSO algorithm, the cost function description can be converted into a unique equation using a weighting number such as:

$$f_{X \epsilon R^D} = \frac{C_D}{C_L} + 10(C_L^* - C_{L2})^2; C_{L2} = \left\{ \begin{array}{lll} C_L^*, & \text{if} & C_L \geq C_L^* \\ C_L, & \text{if} & C_L < C_L^* \end{array} \right\} \tag{58}$$

In both optimization processes, the following design parameters are used: mass flow coefficient, C_q, center location of actuator, x_c, and suction/blowing angle relative to the local tangent,β. Depending on the number of actuators used in AFC, the design parameter vector x is composed of different combinations based on given parameters. In the first three test cases, the center locations of the actuators are kept fixed, the velocities and angles are selected as design variables. However, for the last three cases, the locations of the actuators are also selected as additional design variables. For all the cases, the width of the actuator is kept fixed at 0.035c used in the experiment. The design variables and fixed locations for the first three cases are depicted in Fig.71. The first location, 0.7075c, is selected as the validation point. This location is used by Smith and Walker[21] in their experimental studies as the hinge line of the trailing edge flap. The third location, 0.5125c, is placed behind of the shock wave. Under selected flow conditions, the center of normal shock wave

occurred around 0.5100c. The second location, 0.61775c, is placed between the first and the third locations.

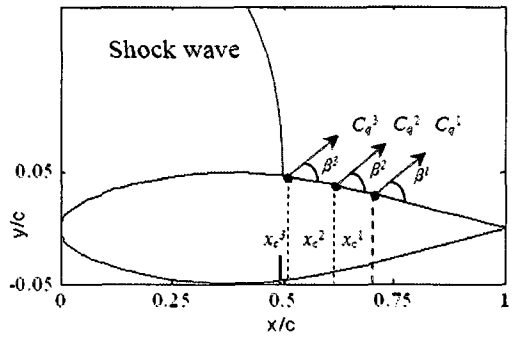

FIG. 71: The design parameters for active flow control

A.4 OPTIMIZATION RESULTS

A.5 FIXED LOCATION OPTIMIZATIONS

The effect of mass flow coefficient and angle for different number of actuators at fixed locations are investigated. For that reason, three cases depending on the number of actuators are studied. First, only one actuator is considered. Then, the number of actuators is increased to two then three to control the flow on the airfoil's upper surface.

1.One-actuator optimization

The center of suction/blowing actuator is placed at 0.7075c. The design parameter vector and bounds are described as,

$$\begin{aligned} \mathbf{x} &= [C_q \ \beta]^T \\ -0.1 \leq C_q &\leq 0.025 \\ 3^0 \leq \beta &\leq 176^0 \end{aligned} \tag{59}$$

Due to the global nature of the PSO algorithm and relatively the small number of design parameters, the optimization process takes only two generations. At the end of optimization, C_q has taken the maximum suction velocity as -0.1 and β became the minimum angle as 3_0 which is almost parallel to the local airfoil surface. The

changes in aerodynamic coefficients C_L and C_D versus computational fluid dynamics (CFD) calls belong to the best particle are depicted in Fig.72. According to these figures, both coefficients are increased due to the suction control. However, the aerodynamic performance based on L/D is also increased. The reason is that the increment in C_L is larger than the increment in C_D. After the suction operation at optimal values, C_L is increased 9.76%; on the other hand, C_D is increased 2.17%. As a result, re-described objective function value (1/f) is increased 7.43%. The change in aerodynamic performance versus CFD calls in PSO is shown on the left side of Fig. 73.

The middle figure in Fig.73 depicts the same objective function change versus CFD calls in SQP optimization process. In this gradient based optimization process, six different initial points (i.p.) are tested to avoid local optimums. After these six SQP optimization processes, the same optimal values found in the PSO process are determined. The PSO case needs 20 CFD calls to reach the optimal values. However, SQP needs 66 CFD calls to get the same optimal values. Additionally, SQP processes are done in accordance with a trial-and-error approach. Therefore, sequential computations are executed. Although sequential computations are implemented, only the best SQP process and the PSO process are compared in terms of computation time on the right side of Fig. 73. One CFD call takes approximately 24 minutes based on Intel 2.4-gigahertz quad-core processor. According to this figure PSO approach is much more time-efficient than the SQP approach.

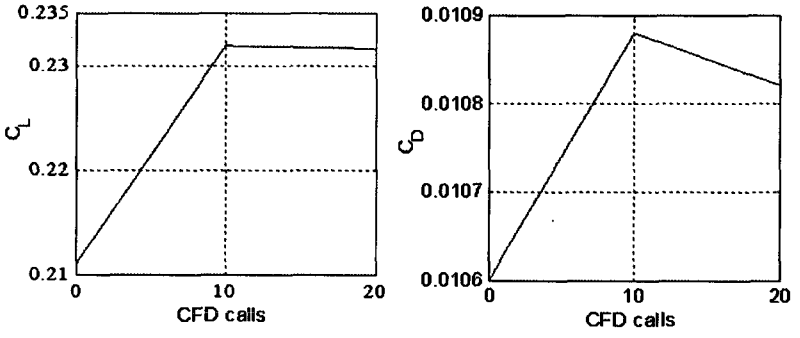

FIG. 72: The change of aerodynamic coefficients during the generations

2. Two-actuator optimization The centers of suction/blowing actuators are placed on 0.7075c and 0.61775c points. The design parameter vector and bounds are described as follows:

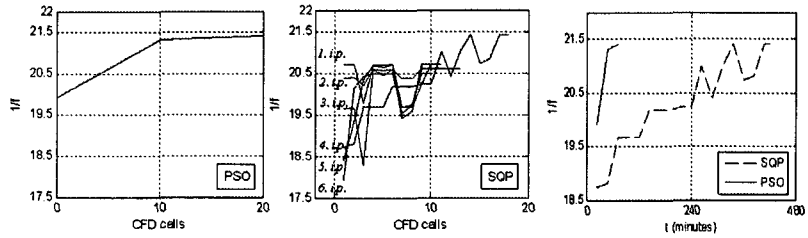

FIG. 73: The change of aerodynamic performance in PSO and SQP

$$\mathbf{x} = [C_q^1 \ \beta^1 \ C_q^2 \ \beta^2]^T$$
$$-0.1 \leq C_q^i \leq 0.025 \tag{60}$$
$$3^0 \leq \beta^i \leq 176^0 \ |^{i=1,2}$$

PSO optimization process takes only four generations. At the end of the optimization, $C_q^{1,2}$ have taken the maximum suction velocity as -0.1 and $\beta^{1,2}$ became the minimum angle as 3^0. The changes of aerodynamic coefficients C_L and C_D versus CFD calls belong to the best particle are depicted in Fig.74. Similar to previous operation, both coefficients are increased due to suction operations. After suction operations at optimal values, C_L increases 16.86%; on the other hand, C_D increases 3.21%. As a result $1/f$ increases 13.25%. The change in aerodynamic performance versus CFD calls in PSO is shown on the left side of Fig.75. The middle figure in Fig.75 depicts the same objective function change versus CFD calls in SQP optimization process. Totally five different initial points are tested to escape from local optimums. After these five SQP optimization processes, the same optimal values found in PSO process are determined. In the PSO process, 40 CFD calls are needed to reach the optimal values. However with SQP, 48 CFD calls are needed to get the same optimal values. Although sequential computations are implemented only the best SQP process and PSO process are compared in terms of computation time on the right side of Fig.75. Similar to the previous optimization case, the PSO approach is much more time-efficient than SQP approach.

3. Three-actuator optimization The centers of suction/blowing actuators are placed on 0.7075c, 0.61775c, and 0.5125c points. The design parameter vector and bounds are described as follows :

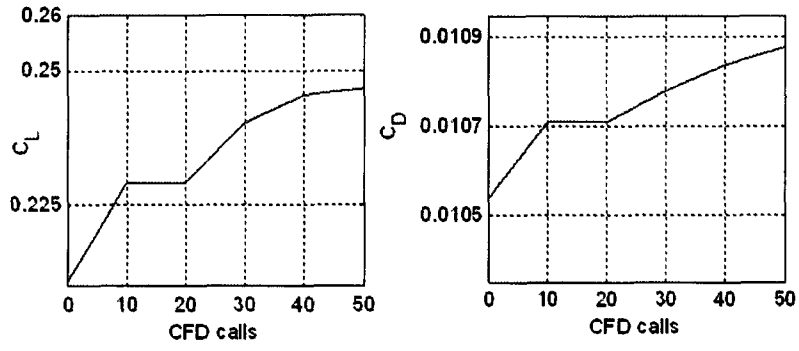

FIG. 74: The change of aerodynamic coefficients during the generations

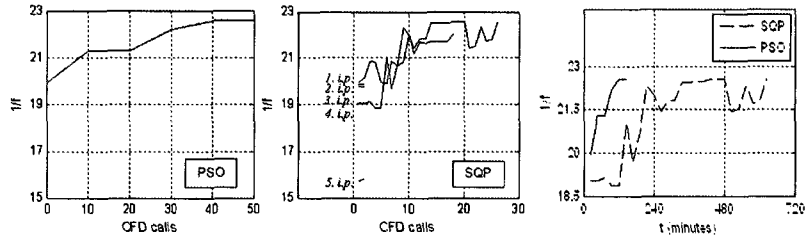

FIG. 75: The change of aerodynamic performance in PSO and SQP

$$\mathbf{x} = [C_q^1\ \beta^1\ C_q^2\ \beta^2\ C_q^3\ \beta^3]^T$$

$$-0.1 \leq C_q^i \leq 0.025 \tag{61}$$

$$3^0 \leq \beta^i \leq 176^0\ |^{i=1,2}$$

The PSO optimization process takes eleven generations. At the end of the optimization, $C_q^{1,2,3}$ has taken the suction velocity as -0.0864, -0.1, and -0.0977, respectively. $\beta^{1,2,3}$ became the minimum angle as 3^0. The changes of aerodynamic coefficients C_L and C_D versus CFD calls belong to the best particle are depicted in Fig.76. After suction operations at optimal values, C_L increases 22.03%; on the other hand, C_D increases 4.82%. As a result 1/f increases 16.46%. The change in aerodynamic performance versus CFD calls in PSO is shown on the left side of Fig.77. The middle figure in Fig.77 depicts the same objective function change versus CFD calls in SQP optimization process. In total, four different initial points are tested to

escape from local optimums based on the previous experience. After these four SQP optimization processes, slightly different optimal values are determined. With SQP, all Cq variables are determined as -0.1 suction velocity; however, all angle values are the same as they are in with the PSO. In SQP, the aerodynamic performance is 16.26%, which is slightly smaller than it is in PSO. In total, 110 CFD calls are needed to reach the optimal values with PSO. However, SQP needs 65 CFD calls to get the same optimal values. The best SQP process and PSO process are compared in terms of computation time on the right side of Fig.77. Although SQP is more efficient than the PSO process in terms of CFD calls, the PSO approach is more time-efficient than SQP approach

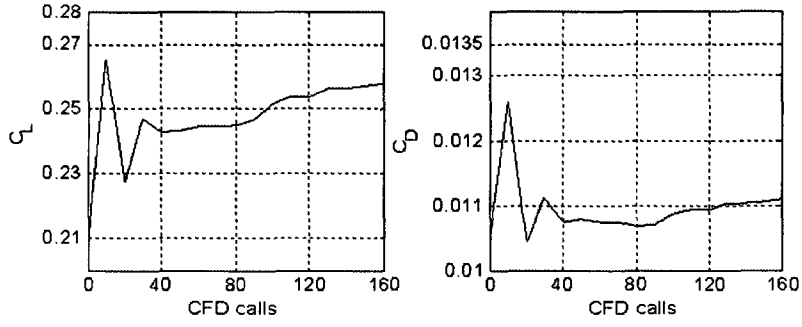

FIG. 76: The change of aerodynamic coefficients during the generations

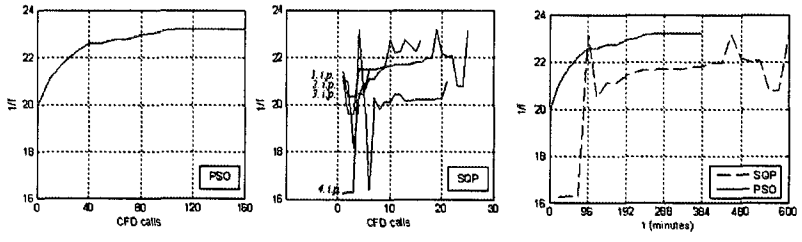

FIG. 77: The change of aerodynamic performance in PSO and SQP

A.6 VARIABLE LOCATION OPTIMIZATIONS

The effects of mass flow coefficient, blowing/suction angle, and the location of center of actuator for different number of actuators are investigated. Similar to previous case studies, three cases depending on the number of actuators are studied. First,

only one actuator is considered. Then, the number of actuators is increased to two then three actuators to control the flow on the airfoil upper surface.

4. One-actuator optimization The design parameter vector and bounds are described as follows:

$$\begin{gathered} \mathbf{x} = [C_q \ \beta \ x_c]^T \\ -0.1 \leq C_q^i \leq 0.025 \\ 3^0 \leq \beta^i \leq 176^0 \\ 0.55c \leq x_c \leq 0.96c \end{gathered} \tag{62}$$

The PSO optimization process takes only four generations. At the end of optimization, C_q has taken the maximum suction velocity as -0.1, β became the minimum angle as 3^0, and the location arrived at 0.5561c which is close to shock wave. These are the same as in the fixed-location case except the location. However, the remaining result is different. The changes of aerodynamic coefficients C_L, C_D and the aerodynamic performance 1/f versus CFD calls belong to the best particle are depicted in Fig.78. After suction operation at optimal values and optimal location, C_L increases 8.02%; on the other hand, C_D decreases 1.33%. As a result 1/f increases 9.46%. This result is reasonably better than the fixed-location optimization case for one-actuator. Another noteworthy point is that the drag is decreased due to change in the location.

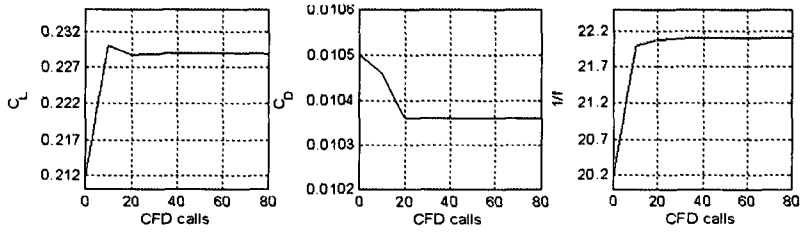

FIG. 78: The change of aerodynamic coefficients and performance during the generations

5. Two-actuator optimization

The design parameter vector and bounds are described as follows:

$$\begin{gathered} \mathbf{x} = [C_q^1 \ \beta^1 \ x_c^1 \ C_q^2 \ \beta^2 \ x_c^2]^T \\ -0.1 \leq C_q^i \leq 0.025 \end{gathered} \tag{63}$$

$$3^0 \leq \beta^i \leq 176^0 \mid^{i=1,2}$$

$$0.70c \leq x_c^1 \leq 0.90c$$

$$0.55c \leq x_c^2 \leq 0.65c$$

To avoid the geometrical interaction, 0.05c distance is kept between the actuators. PSO optimization process takes six generations. At the end of optimization, both C_q variables have taken the maximum suction velocity as -0.1. Similarly, both β angles became the minimum angle at 3^0, the first location x_c^1 is arrived at 0.5724c, which is close to the shock wave, and the second location is x_c^2 arrived at 0.7000c. These are the same values as in the fixed-location case except the locations. The changes of aerodynamic coefficients C_L, C_D and performance $1/f$ versus CFD calls belong to the best particle are depicted in Fig.79. After suction operations at optimal values and optimal locations C_L increases 17.68%; on the other hand, C_D increases 1.71%. As a result $1/f$ increases 15.69%. This result is much better than the fixed-location optimization case for two-actuators.

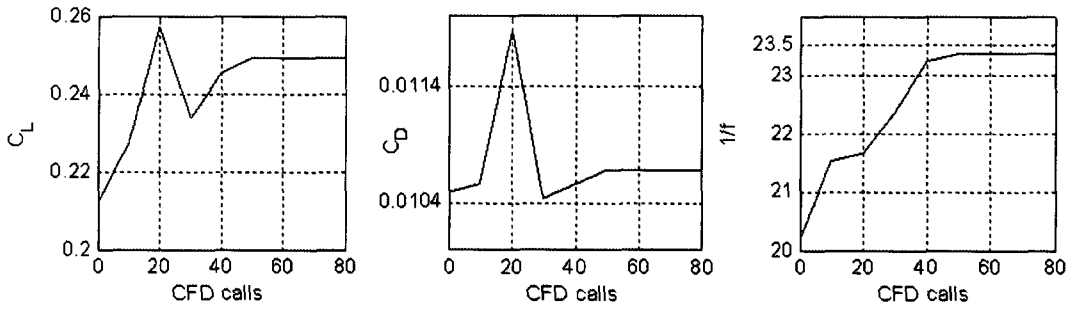

FIG. 79: The change of aerodynamic coefficients and performance during the generations

6. Three-actuator optimization

The design parameter vector and bounds are described as follows:

$$\mathbf{x} = [C_q^1 \ \beta^1 \ x_c^1 \ C_q^2 \ \beta^2 \ x_c^2 \ C_q^3 \ \beta^3 \ x_c^3]^T$$

$$-0.1 \leq C_q^i \leq 0.025 \tag{64}$$

$$3^0 \leq \beta^i \leq 176^0 \mid^{i=1,2,3}$$

$$0.85c \leq x_c^1 \leq 0.96c$$

$$0.70c \leq x_c^2 \leq 0.80c$$

$$0.55c \leq x_c^3 \leq 0.65c$$

Similar to the previous case study, to avoid the geometrical interaction among the actuators 0.05c distance is kept between the actuators. The PSO optimization case needs eleven generations. At the end of optimization, $C_q^{1,2,3}$ have taken the suction velocity as -0.1, -0.077, and -0.1, respectively. $\beta^{1,2,3}$ became the minimum angle at 3^0; the first location x_c^1 is arrived at 0.5889c, which is close to the shock wave, the second location x_c^2 is arrived at 0.7700c, and the third location x_c^3 is arrived at 0.9600c. The changes of aerodynamic coefficients C_L, C_D and the performance $1/f$ versus CFD calls belong to the best particle are depicted in Fig.80. After suction operations at optimal values and optimal locations, C_L increases 37.48%; on the other hand, C_D increases 14.29%. As a result $1/f$ increases 20.7%. This result is much better than the fixed-location optimization case for three-actuators.

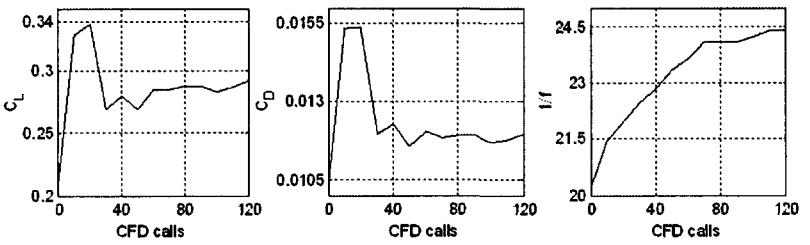

FIG. 80: The change of aerodynamic coefficients and performance during the generations

A.7 COMPARATIVE EVALUATIONS

Both studies showed that the number of actuators and their locations have important effects on the aerodynamic performance. In Fig. 81, the relationship between the number of actuators and performance is depicted. Using more actuators on the airfoil surface provides more increase in the aerodynamic performance. The increasing trend looks like an exponential curve. Selection of actuator location is the other emphasized point. Instead of determining the locations based on rudimentary guessing, using optimized locations provide more efficient results. As seen in Fig. 81, using only two actuators at proper locations can provide almost the same level aerodynamic performance increase as using three actuators.

On the other hand, using an actuator causes the change in the location of the shock wave. In all the cases, the shock location moves downstream. On the left side of

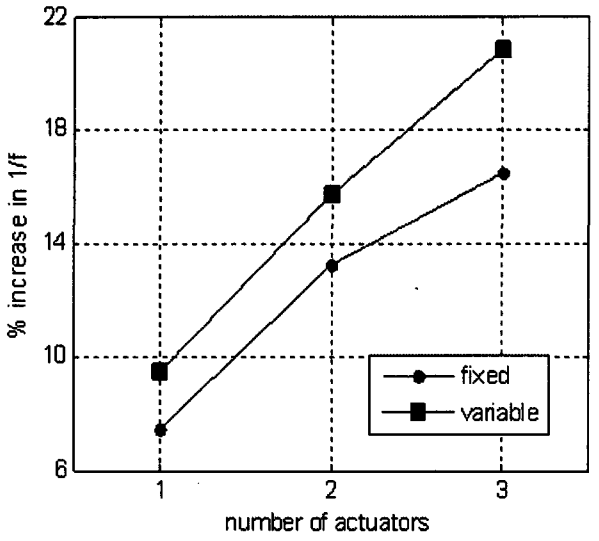

FIG. 81: The effect of location and the number of actuators on an aerodynamic performance

Fig.82, the pressure contours are shown for a fixed-location case using one-actuator. Due to suction at 0.7075c point, a local pocket is generated. This pocket pushes the shock to 0.5625c, which is farther than the original location of 0.5100c. On the right side of Fig.82, the pressure contours are shown for the optimized location case with one actuator. Similar to the fixed location case, the suction at 0.5561c point, a local pocket is generated. This pocket pushes the shock to 0.5350c. The effects of both suction operations on the pressure coefficient can be seen in the middle part of Fig. 82. Selected fixed location causes a sharp increase and then a sharp decrease in the C_p distribution. However, suction at the optimal location causes relatively small and smooth decrease and then a remarkable increase in the C_p distribution. In both cases, it is observed that the shock is pushed downstream as compared to the no-suction cases.

On the left side of Fig.83, the pressure contours are shown for the fixed-location case with two actuators. Due to suction at the 0.7075c and 0.61775c points, two separate pockets are generated. As a consequence, the shock wave is located at 0.5400c. The resulting effect on the pressure coefficient distribution can be seen in the middle part of Fig.83: sharp increases and decreases are visible. On the right side of Fig.83, the pressure contours are shown for the optimized locations of the two

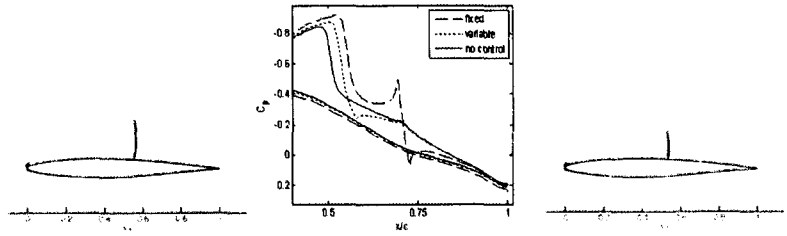

FIG. 82: The effect of control on the pressure field and coefficient for the one-actuator case

actuators. With suction at the 0.5724c and 0.7000c points, only a single local pocket is generated and the shock is pushed further aft to 0.5500c. The resulting effect on the pressure coefficient distribution is a relatively smooth decrease followed by an increase. Again, in both cases, it is observed that the shock is pushed downstream as compared to the no-suction cases

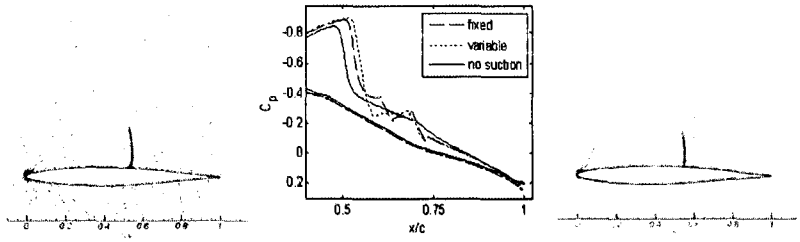

FIG. 83: The effect of location on pressure field and coefficient for the two-actuator case

On the left side of Fig.84, the pressure contours are shown for the fixed location case with three actuators. Because of suction at the 0.7075c, 0.61775c, and 0.5125c points, now three pockets are generated. As a consequence, the shock wave is located at 0.5525c. On the right side of Fig.83, the pressure contours are shown for the optimized locations. Suction at the 0.9600c, 0.7700c, and 0.5889c points generate a merged pocket and an additional single pocket. Consequently, the shock wave is pushed aft to 0.5650c, which is the farthest downstream point of all the cases. The effect of the fixed-location and the optimized-location suctions on the pressure coefficient distributions can be seen in the middle Fig. 16. Similar to previous cases, fixed-location cases cause sharp increases and decreases. However, suction at the optimal locations cause a relatively smooth decrease and increase. Once again, in

both cases, it is observed that the shock is pushed downstream as compared to the no-suction cases.

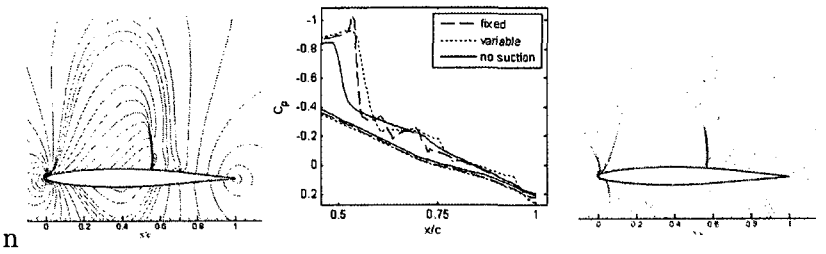

n

FIG. 84: The effect of location on pressure field and coefficient for the three-actuator case

In all the cases, pushing the shock more aft towards the trailing edge extends the supersonic region and shortens the subsonic area. Additionally, the optimization results in squeezing the suction locations to be closer or merged for improved aerodynamic performance.

A.8 CONCLUSIONS

In the first part of the present paper, computational simulations are reported to investigate the benefits of AFC in improving the aerodynamic performance of a 2D airfoil at a transonic speed, and by using a heuristics-based optimization technique PSO and the gradient-based optimization technique SQP. The suction and blowing angles and mass flow coefficients are taken as the design variables in the studied one-actuator, two-actuator, and three-actuator cases. A Navier Stokes solver is coupled with both optimizers to obtain the necessary flow analyses for the initial design parameters and then improve the aerodynamics of the airfoil via the optimization.

As a gradient-based optimization method's success depends heavily on the initial design point, several optimization runs with different initial values are needed to avoid the local minima. Therefore, it is generally observed that the *PSO* approach is more efficient than the SQP in terms of time and *CFD* calls. Using more actuators provides better aerodynamic performance. However, this trend is exponential. Suction operations result in increases in both lift and drag for all the cases, but C_L increase is more than that of CD, resulting in better aerodynamic performance. The best result is provided by the three-actuator case with a 16.46% increase in the aerodynamic performance. Additionally, the shock wave location on the upper surface

is moved toward the trailing edge resulting in the extension of the supersonic region for all the cases.

In the second part of the present paper, computational cases are reported to investigate the benefits of AFC on the aerodynamic performance of the same airfoil under the same flow conditions by using PSO. The suction and blowing angles, mass flow coefficients, and the locations of the actuators are taken as the design variables in the one-actuator, two-actuator, and three-actuator cases. A Navier Stokes solver is coupled with the PSO optimizer to obtain a flow solution for a given initial design and then improve the aerodynamics of the airfoil via the optimization.

Similar to the previous cases, using more actuators provides better aerodynamic performance. Suction operations result in increased C_L and either decreased or increased C_D. The one-actuator case provides a particularly interesting result because C_D is decreased and C_L is increased in this case. The best result is provided by the three-actuator case with 20.7% increase in the aerodynamic performance. All the cases provide better results than their fixed-location counterparts. Again, the shock wave location on the upper surface is further aft towards the trailing edge, resulting in the extension of the supersonic region for all the cases. Another noteworthy point is that the optimization processes move closer or merge with the actuator locations, which effectively provides a more global suction.

Finally, it is concluded that AFC can provide high aerodynamic performance enhancement by optimizing its parameters. However, AFC alone may not be sufficient to get the best designs. Therefore, it is recommended as a follow up to study simultaneous AFC and passive flow control techniques.

APPENDIX B

TIME ADVANCEMENT

For a non-deforming mesh, Equation 2 can be written as:

$$\frac{1}{J}\frac{\partial Q}{\partial t} = R(Q) \tag{65}$$

where

$$R = -\left[\frac{\partial(\hat{F}-\hat{F}_v)}{\partial\xi} + \frac{\partial(\hat{G}-\hat{G}_v)}{\partial\eta} + \frac{\partial(\hat{H}-\hat{H}_v)}{\partial\zeta}\right] \tag{66}$$

The time term can be discretized with backward differencing:

$$\frac{(1+\Phi)(Q^{n+1}-Q^n)-\Phi(Q^n-Q^{n-1})}{J\Delta t} = R(Q^{n+1}) \tag{67}$$

n indicates time level. If the method is first-order temporally accurate, $\Phi = 0$; when $\Phi = \frac{1}{2}$ the method is second-order accurate. The right-hand side is a function of the unknown flow variables at time level $n+1$, so that this equation is implicit.

This code advances the solution in time using an approximate factorization algorithm. The implicit derivatives are written as spatially first-order accurate, which results in block-tridiagonal inversions for each sweep. Though, for the solutions that make use of FDS the block-tridiagonal inversions are generally simplified with a diagonal algorithm (with a spectral radius scaling of the viscous terms).

Because the left-hand side is treated for computational efficiency in steady-state simulations (approximate factorization, first-order accuracy), second-order temporal accuracy is sacrificed for unsteady computations. The use of sub-iterations id one of the method to obtain the desired accuracy. Two different sub-iteration strategies have been utilized in CFL3D. The first method is termed "pseudo time sub-iteration ($\tau - TS$)" also known as the dual time stepping method. The other method is termed "physical time sub-iteration (t -TS)".

For the $\tau - TS$ method, a pseudo time term is added to the time-accurate Navier-Stokes equations.

$$\frac{1}{J}\frac{\partial Q}{\partial \tau} + \frac{(1+\phi)(Q^{n+1}-Q^n)-\phi(Q^n-Q^{n-1})}{J\Delta t} = R(Q^{n+1}) \tag{68}$$

This equation is then discretized and iterated in Eq. 3, where is the sub-iteration counter.

$$\frac{(1+\phi')(Q^{m+1}-Q^m)-\phi'(Q^m-Q^{m-1})}{J\Delta\tau} + \frac{(1+\phi)(Q^{m+1}-Q^n)-\phi(Q^n-Q^{n-1})}{J\Delta t} = R(Q^{m+1}) \tag{69}$$

In Eq. 68, ϕ and ϕ' govern the order of accuracy of the physical and pseudo time terms, respectively. In actuality, the pseudo time term is dealt with as a first order (i.e., $\phi' = 0$), but the general form is indicated here for completeness. As $m \to \infty$, the pseudo time term disappears if the sub-iterations converge and $Q^{m+1} \to Q^{n+1}$. It is linearized with

$$R(Q^{m+1}) \cong R(Q^m) + \frac{\partial R}{\partial Q}\Delta Q^m \tag{70}$$

and the quantity $\frac{-(1+\phi)Q^m}{J\Delta t}$ is added to both sides of Eq.68, then Eq.68 becomes

$$\left[\left(\frac{1+\phi'}{J\Delta\tau}+\frac{1+\phi}{J\Delta t}\right)I+\delta_\xi A+\delta_\eta B+\delta_\varsigma C\right]\Delta Q^m = \frac{\phi'\Delta Q^{m-1}}{J\Delta\tau}+\frac{\phi\Delta Q^{n-1}}{J\Delta t}-\frac{(1+\phi)(Q^m-Q^n)}{J\Delta t}+R(Q^m) \tag{71}$$

where

$$\begin{aligned} \Delta Q^m &= Q^{m+1}-Q^m \\ A &= \frac{\partial(\hat{F}-\hat{F}_v)}{\partial Q} \\ B &= \frac{\partial(\hat{G}-\hat{G}_v)}{\partial Q} \\ C &= \frac{\partial(\hat{H}-\hat{H}_v)}{\partial Q} \end{aligned} \tag{72}$$

Eq.71 is approximately factored and written in primitive variable form; it is solved as a series of sweeps in each coordinate direction.

In the $t-TS$ method, Eq.67 is only iterated in , where is the sub-iteration counter:

$$\frac{(1+\Phi)(Q^{m+1}-Q^n)-\Phi(Q^n-Q^{n-1})}{J\Delta t} = R(Q^{m+1}) \tag{73}$$

The quantity $\frac{-(1+\phi)Q^m}{J\Delta t}$ is added to both sides, the residual is linearized, and the equation is approximately factored and written in primitive variable form.

APPENDIX C

SPATIAL DISCRETIZATION

C.1 DISCRETIZATION OF INVISCID FLUXES

The spatial derivatives of the convective and pressure terms are written conservatively as a flux balance across a cell as [89]. From Eq.72,

$$(\delta_\xi \hat{F})_i = \hat{F}_{i+\frac{1}{2}} - \hat{F}_{i-\frac{1}{2}} \tag{74}$$

where the i index indicates a cell-center location and $i \pm \frac{1}{2}$ corresponds to a cell-interface location. The state-variable interpolation and a locally one-dimensional flux model is used to determine the interface flux. CFL3D offers Flux limiting, Flux vector Splitting and Flux difference splitting, but only the Flux Difference Splitting method is chosen to split these inviscid fluxes in this study.

C.2 FLUX DIFFERENCE SPLITTING

The interface flux in the ξ direction is written as

$$\hat{F}_{i+\frac{1}{2}} = \frac{1}{2}\left[\hat{F}(q_L) + \hat{F}(q_R) - |\tilde{A}_{inv}|(q_R - q_L)\right]_{i+\frac{1}{2}} \tag{75}$$

where $\tilde{A}_{inv}$ is the evaluation of A_{inv} with Roe-averaged variables defined as below:

$$A = \frac{\partial(\hat{F} - \hat{F}_v)}{\partial Q} \tag{76}$$

$$|\tilde{A}_{inv}| = |A_{inv}(\tilde{q})| \tag{77}$$

A_{inv} is the inviscid part of the matrix A, that is,

$$A_{inv} = \frac{\partial \hat{F}}{\partial Q} = T \bigwedge T^{-1} = T(\overset{+}{\bigwedge} + \overset{-}{\bigwedge})T^{-1} \tag{78}$$

$$|A_{inv}| = T \bigwedge T^{-1} \tag{79}$$

T is the matrix of right eigenvectors as columns and T^{-1} is the matrix of left eigenvectors as rows. $\bigwedge$ is the diagonal matrix of eigenvalues of the matrix A_{inv}. They are all evaluated using Roe-averaged values such that the term given below is satisfied exactly.

$$\hat{F}_(Q_R) - \hat{F}_(Q_L) = |A_{inv}|(Q_R - Q_L) \tag{80}$$

Here, the above term $A_{inv}|(Q_R - Q_L$ can be written as below:

$$|A_{inv}|(Q_R - Q_L) \equiv |\tilde{A}_{inv}|\Delta Q = \begin{bmatrix} \alpha_4 \\ \tilde{u}\alpha_4 + \hat{\xi}_x\alpha_5 + \alpha_6 \\ \tilde{u}\alpha_4 + \hat{\xi}_x\alpha_5 + \alpha_7 \\ \tilde{u}\alpha_4 + \hat{\xi}_x\alpha_5 + \alpha_8 \\ \tilde{H}\alpha_4 + (\tilde{\bar{U}} - \hat{\zeta})\alpha_5 + \tilde{u}\alpha_6 + \tilde{v}\alpha_7 + \tilde{w}\alpha_8 - \frac{\tilde{a}^2\alpha_1}{\gamma-1} \end{bmatrix} \tag{81}$$

where,

$$\alpha_1 = |\frac{\nabla\xi}{J}|\tilde{\bar{U}}|(\Delta\rho - \frac{\Delta p}{\tilde{a}^2})$$

$$\alpha_2 = \frac{1}{2\tilde{a}^2}|\frac{\nabla\xi}{J}|\tilde{\bar{U}} + \tilde{a}|(\Delta p + \tilde{\rho}\tilde{a}\Delta\hat{U})$$

$$\alpha_3 = \frac{1}{2\tilde{a}^2}|\frac{\nabla\xi}{J}|\tilde{\bar{U}} - \tilde{a}|(\Delta p - \tilde{\rho}\tilde{a}\Delta\hat{U})$$

$$\alpha_4 = \alpha_1 + \alpha_2 + \alpha_3 \tag{82}$$

$$\alpha_5 = \tilde{\alpha}(\alpha_2 - \alpha_3)$$

$$\alpha_6 = |\frac{\nabla\xi}{J}|\tilde{\bar{U}}|(\rho\Delta u - \hat{\xi}_x\tilde{\rho}\nabla\bar{U})$$

$$\alpha_7 = |\frac{\nabla\xi}{J}|\tilde{\bar{U}}|(\rho\Delta u - \hat{\xi}_y\tilde{\rho}\nabla\bar{U})$$

$$\alpha_8 = |\frac{\nabla\xi}{J}|\tilde{\bar{U}}|(\rho\Delta u - \hat{\xi}_z\tilde{\rho}\nabla\bar{U})$$

The tilde ($\sim$) symbol indicates the following Roe-averaged variables.

$$\tilde{\rho} = \sqrt{\rho_L \rho_R}$$

$$\tilde{u} = \frac{u_L + u_R\sqrt{\frac{\rho_R}{\rho_L}}}{1 + \sqrt{\frac{\rho_R}{\rho_L}}}$$

$$\tilde{v} = \frac{v_L + v_R\sqrt{\frac{\rho_R}{\rho_L}}}{1 + \sqrt{\frac{\rho_R}{\rho_L}}}$$

$$\tilde{w} = \frac{w_L + w_R\sqrt{\frac{\rho_R}{\rho_L}}}{1 + \sqrt{\frac{\rho_R}{\rho_L}}}$$

$$\tilde{H} = \frac{H_L + H_R\sqrt{\frac{\rho_R}{\rho_L}}}{1 + \sqrt{\frac{\rho_R}{\rho_L}}} \tag{83}$$

$$\tilde{a}^2 = (\gamma - 1)\tilde{H} - \frac{\tilde{u}^2 + \tilde{v}^2 + \tilde{w}^2}{2}$$

$$\tilde{\bar{U}} = \frac{1}{|\nabla\xi|}(\xi_x\tilde{u} + \xi_y\tilde{v} + \xi_z\tilde{w} + \xi_t)$$

C.3 DISCRETIZATION OF VISCOUS FLUXES

Second-order central differences is utilized to discretize the viscous terms. The second derivatives are related to differences across cell interfaces of first-derivative terms. Hence, the viscous terms are discretized as

$$(\delta_\xi\hat{F}_\nu)_i = (\hat{F}_\nu)_{i+\frac{1}{2}} - (\hat{F}_\nu)_{i-\frac{1}{2}} \tag{84}$$

In Eq.7, $\hat{F}_\nu$, using the thin-layer approximation

$$\hat{F}_\nu = \frac{M_\infty \mu}{Re_{\tilde{L}_R} J} \begin{bmatrix} 0 \\ \phi_1 \frac{\partial u}{\partial \xi} - \xi_x \phi_2 \\ \phi_1 \frac{\partial v}{\partial \xi} - \xi_y \phi_2 \\ \phi_1 \frac{\partial w}{\partial \xi} - \xi_z \phi_2 \\ \phi_1 [\delta_\xi (\frac{|V|^2}{2}) + \frac{1}{Pr(\gamma-1)} \delta_\xi (a)^2] + (U - \xi_t)\phi_2 \end{bmatrix} \tag{85}$$

where

$$\phi_1 = \xi_x^2 + \xi_y^2 + \xi_z^2$$

$$\phi_2 = \frac{(\xi_x \frac{\partial u}{\partial \xi} + \xi_y \frac{\partial v}{\partial \xi} + \xi_z \frac{\partial w}{\partial \xi})}{3}$$

APPENDIX D

THOMAS CODE

Thomas code is one of the far-field components of a SB calculation methodology. It uses the waveform parameter method. This method depends on a result from geometric acoustics for the wave amplitude and uses isentropic wave theory to account for nonlinear wave deformation [83]. The waveform is defined as a set of parameters. The time rates of change of these parameters are required to obtain the distortion of the signature. The conservation of the Blokhintsev energy invariant along ray tubes [90] is used to derive the waveform amplitude:

$$p\sqrt{\frac{c_n^2 A}{\rho_0 a_0^3}} = F(\xi) \tag{86}$$

The acoustic pressure p is a function of both phase ξ and altitude z. A, the ray tube are as cut by the wavefront, c_n, a speed that a wave propagates normal to itself, a_0 and ρ_0, the ambient sound speed and density respectively are functions only of altitude. As the wave is assumed isentropic and of small amplitude, the isentropic wave theory can be utilized to derive the propagation speed of any point on the waveform, $u + a$.

$$u + a = a_0(1 + \frac{\gamma + 1}{2\gamma}\frac{p}{p_0}) \tag{87}$$

From Eq.86,

$$u + a = a_0 + \frac{\gamma + 1}{2}\sqrt{\frac{a_0}{\rho_0 A c_n^2}}F(\xi) \tag{88}$$

Let the pressure p versus time T plot is used as an input and zero disturbance point is $T = 0$. The amount of nonlinear waveform distortion during the propagation time increment dt can be calculated by

$$dT = \frac{a_0 - (u + a)}{c_n}dt \tag{89}$$

z, altitude of the wave, and its rate of change with respect to dt;

$$\frac{dz}{dt} = -a_0 sin\theta \tag{90}$$

Then, the total nonlinear distortion between initial altitude z_1 to desired altitude z_2 can be evaluated by

$$\Delta T(\xi) = \frac{\gamma+1}{2} F(\xi) \int_{z_1}^{z_2} \frac{dz}{\sqrt{\rho_0 a_0 c_n^4 A sin^2\theta}} \tag{91}$$

Let is define the relationship between T nad ξ:

$$T = \xi - \tau F(\xi) \tag{92}$$

τ is "age variable" and is evaluated from

$$\tau = -\frac{\gamma+1}{2} \int_{z_1}^{z_2} \frac{dz}{\sqrt{\rho_0 a_0 c_n^4 A sin^2\theta}} \tag{93}$$

c_n is speed that is given by,

$$c_n = a_0 + \vec{V}_0 . \vec{n}$$

where $\vec{V}_0$ is wind velocity, and $\vec{n}$ is wavefront unit normal. Then
$c_n = c_0 cos\theta$, c_0 is constant, and θ is an angle between $\vec{n}$ and the horizontal plane.

For the calculations, two different area definitions can be utilized. A corresponds to a ray tube area as cut by the wavefront, and A_h is a ray tube area as cut by a horizontal plane. The relationship between the two areas is given by;

$$A_h = \frac{c_n}{a_0} \frac{A}{sin\theta} \tag{94}$$

The above equations define the F function relates to pressure information at initial altitude. Up to this point, the F function method and waveform parameter approach have been same. In the waveform method, the signature is divided into linear segments which are described by m_i, is the slope of $\frac{\partial p}{\partial T}$, ΔP_i, pressure rise across the shock, and λ_i is the time duration ΔT.

$$
\begin{aligned}
m_i &= \frac{p_{\xi_i}}{T_{\xi_i}} \\
\Delta p_i &= \sqrt{\frac{\rho_0 a_0^3}{c_n^2 A}} \Delta F_i \\
\lambda_i &= T_{i+1} - T_1
\end{aligned}
\tag{95}
$$

These are the three ordinary, first-order, coupled differential equations for the waveform parameters which completely define the distortion of the waveform[83]. The deformation of any arbitrary wave in a nonuniform atmosphere with winds can be evaluated using the above parameters.

VITA

BEDRI YAGIZ
Department of AEROSPACE ENGINEERING
Old Dominion University
Norfolk, VA 23529

Bedri Yagiz was born on August 24, 1979 in Ceyhan, ADANA, Turkey. He graduated from Gaziantep Science High School in 1997, a prestigious high school in Turkey that selects its students through a nationwide exam and provides a sophisticated education in mathematics and the sciences. He was admitted to Aeronautical Engineering at Istanbul Technical University (ITU) in 1997. He received his Bachelor of Science degree in Aeronautical Engineering at Istanbul Technical University in August 2002. Then, he worked as an aerodynamic design and research engineer in the ROTAM Helicopter Project center located in (ITU) while doing his graduate studies. After the completion of the Master of Science degree in August 2005, he woked for Turkish Airlines Technic as a hydromechanics systems engineer in Ataturk International Airport, Istanbul, TURKEY. However, his interests brought him back to research, and he was admitted into the Aerospace Engineering Department at Old Dominion University in January 2006 to pursue his Ph.D. During his Ph.D. study, he was awarded a research assistantship by the department. He was involved in research work pertaining to CFD, Shock and Sonic Boom Mitigation. He married Emine T. Uslu on 21 May 2006, and now he has two precious kids, Yusuf F. and Zeynep N. Yagiz.

Typeset using LaTeX.